POLITECNICO DI TORINO

Master of Science in Energy and Nuclear Engineering

Master’s Degree Thesis

Preliminary assessment of SFNM04 perovskite for CO_2 dissociation through Renewable Chemical Looping process

Supervisors

Prof. Massimo Santarelli

Dr. Domenico Ferrero

Dr. Cannone Salvatore

Candidate

Noemi Giachi

December 2021

“Anche chi non c’è più ci protegge da lassù
Sarà lungo il cammino vedrai
Avrai gioia e dolore, ma non avere mai timore
Non potranno dividerci mai”

Alla mia unica realtà.

Abstract

The indications from the Energy Roadmap 2050, various reports and developments worldwide clearly indicate that fossil fuels will continue to be present in the future of Europe and the world and will still be used in many industrial processes. However, the current climate crisis, caused by the continuous and increasing release of CO_2 into the atmosphere, has reached a drastic level, in which changes made by humans on the ecosystem are more and more tangible. In this framework, Carbon Capture Utilization and Storage technologies (CCUS) can play an important role for this transition period, accompanying the current world energy production sector, based on fossil fuels, towards a zero emissions condition driven by renewable resources. CCUS is in fact a hybrid solution in which the CO_2 leaving the plants is captured instead of being released into the atmosphere and then stored or reused to produce useful products. This last solution is preferred, as it would allow to transform a product until now discarded into one of commercial value, also allowing a recovering of the capture costs. Once captured, CO_2 can in fact be used to create various useful products: among all stands out the syngas, a mixture of hydrogen and carbon monoxide that is the basic component for the creation of other important chemicals, such as ethanol, methanol and DME. There are several methods for syngas synthesis: among these, the technology of Renewable Chemical Looping is very interesting, because it uses high temperature solar energy (green and clean) from concentrating solar for the splitting of H_2O and CO_2; the syngas so created is also called Solar Fuel. Chemical looping is a thermochemical process in which a redox material (also called oxygen carrier) reacts alternately with oxidizing and reducing gas mixtures and returns to the initial composition at the end of the redox cycle, ensuring the repeatability of the process. Different types of chemical looping materials have been studied and tested: in addition to the most common, such as metal oxides and cerium oxides, perovskites are considered very promising materials.

In this study, which is part of an international collaboration between the Polytechnic of Turin, Massachusetts Institute of Technology (MIT) and University of Udine, a new type of perovskite, synthesized by the University or Udine, is studied, and tested in a microreactor in order to analyze its chemical stability and performance within the redox cycle. This material is $Sr_2FeNi_{0.4}Mo_{0.6}O_{6-\delta}$ (SFNM04) and has the peculiarity to show

an exsolution phenomena of *Fe2+* and *Ni3+* when reduced, causing the creation of *Fe-Ni* alloys on the surface of the sample that act as catalyst for the oxidation step and also a larger number of oxygen vacancies in the material, leading to a bigger yield of CO at the end of the cycle. In particular, the aim of this work is to study the behavior of the material while varying the parameters of the process, such as the concentration of the reducing and oxidizing mixtures (the studied range of H_2 is from 5% to 100%, while the CO_2 varies between 6% and 100%, both mixed with nitrogen), the temperature for the two steps and reaction times (from 15 up to 120 minutes); temperatures considered have a range from 550°C up to a maximum of 850°C: bigger temperature were never investigated since the main peculiarity of perovskites is to have yields comparable to the ones of other materials, but with lower temperature. Once the tests were completed, results have been processed in order to assess the SFNM04 response to the variation of these parameters and to calculate the CO produced, in terms of CO global yield, CO maximum production rate and CO_2 conversion.

The results showed a positive effect in the final yield by increasing the reduction times, as well as the temperature (both in oxidation and reduction) and the H_2 concentrations as reducing gas and CO_2 as oxidizing gas: such behavior has been subject to further consideration in order to better understand how the variation of parameters may have influenced the performance of this type of perovskite, in particular by altering its structure, in order to optimize the set-up of the process and ensure a role for this material in the decarbonization pathway the world is trying to pursue.

Summary

List of Figures

List of Tables

Acronyms

GHG	Greenhouse Gas
GWP	Global Warming Potential
IEA	International Energy Agency
SDS	Sustainable Development Scenario
TFEC	Total Finale Energy consumption
TPES	Total Primary Energy Supply
CCS	Carbon Capture and Storage
CCUS	Carbon Capture Utilization and Storage
DME	Dimethyl Ether
CL	Chemical Looping
CSP	Concentrating Solar Power
TR	Thermal Reduction
IGCC	Integrated Coal Gasification Combine Cycle
MEA	Monoethanolamine

MOF	Metallic Organic Framework
PPN	Porous Polymer Networks
DEA	Diethylamine
MDEA	Monodiethylamine
CMS	Carbon Molecular Sieves
PSA	Pressure Swing Adsorption
WGS	Water Gas Shift
SEWGS	Sorption Enhanced Water Gas Shift
ASU	Air Separation Unit
CASU	Cryogenic Air Separation Unit
CLAS	Chemical Looping Air Separation
EOR	Enhanced Oil Recovery
EGR	Enhanced Gas Recovery
ECBM	Enhanced Coal Bed Methane
SOFC	Solid Oxide Fuel Cell
SOEC	Solid Oxide Electrolyzer Cell

PEC	PhotoElectroChemical
FCC	Fluid Catalytic Crackers
CLC	Chemical Looping Combustion
SCL	Syngas Chemical Looping
CDCL	Coal Direct Chemical Looping
VAM	Ventilation Air Methane
OC	Oxygen Carrier
WS	Water Splitting
CDS	Carbon Dioxide Splitting
CLR	Chemical Looping Reforming
TGA	Thermogravimetric Analysis
SFNM	Strontium-Iron-Nickel-Molybdenum perovskite
LSFM	Lanthanum-Strontium-Iron-Molybdenum perovskite
YSZ	Yttria Stabilized Zirconia

MFCs	Mass Flow Controllers
UniUD	University of Udine
MIT	Massachusetts Institute of Technology
SCADA	Supervisory Control and Data Acquisition
TCD	Thermal Conductivity Detector
TPR	Temperature Programmed Reduction
RP	Ruddlesden-Popper
SEM	Scanning Electron Microscopy
PSU	Power Supply Unit

Chapter 1

1. Introduction

The context in which we live is increasingly conditioned by climate change issues. In recent years the world population has developed a progressive awareness about the fact that the way of life so far maintained can no longer be sustainable. The scientific world, world organizations and governments have realized that the consumption and emissions of greenhouse gases, which have marked our society since the second industrial revolution, are not compatible in the long term with the ecosystem in which we are living. It is well known that greenhouse gases (GHGs) are one of the main causes of global warming. Although they are naturally present in the atmosphere, their excessive concentration is directly due to human activities, since their production is certainly at a higher rate in comparison to what nature emits and is capable of absorbing. Among GHGs, CO_2 is the most dominant gas injected in the atmosphere and it accounts for three-quarters of total emissions (74.4%) [1].

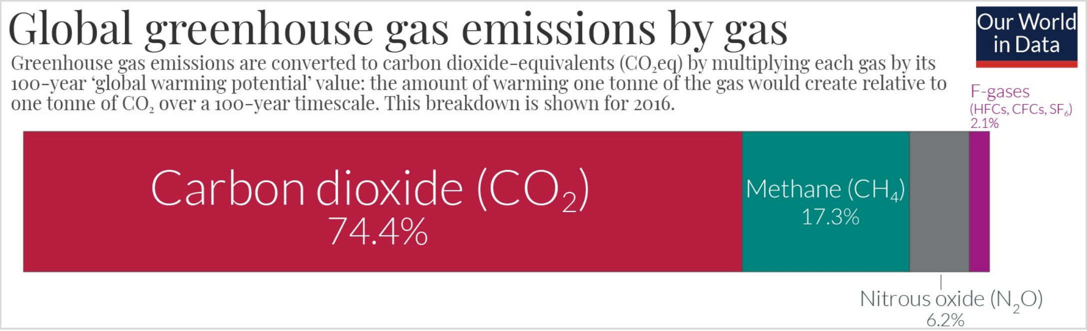

***Figure 1.1**: Total global GHG emissions* [1].

Even if CO_2 is the gas with the lowest GWP[1], because of the amount and the velocity at which it's emitted, together with its long life in atmosphere (it's able to lasts hundreds of thousands of years in the atmosphere), CO_2 is recognized as the first cause of the rise in global mean temperature. The constant increase in the mean concentration of carbon dioxide in the atmosphere is indeed an established fact. Over the years it rose from 280 ppm in the pre-industrial era to 389 ppm at the end of 2010 [2]. Currently the presence of CO_2 in the atmosphere accounts to 414 ppm (data updated in August 2021) [3]. The main source of concern is the fact that this trend seems likely to consolidate in the absence of appropriate containment policies. The CO_2 concentrations would reach at this rate levels that would compromise the entire Earth's ecosystem.

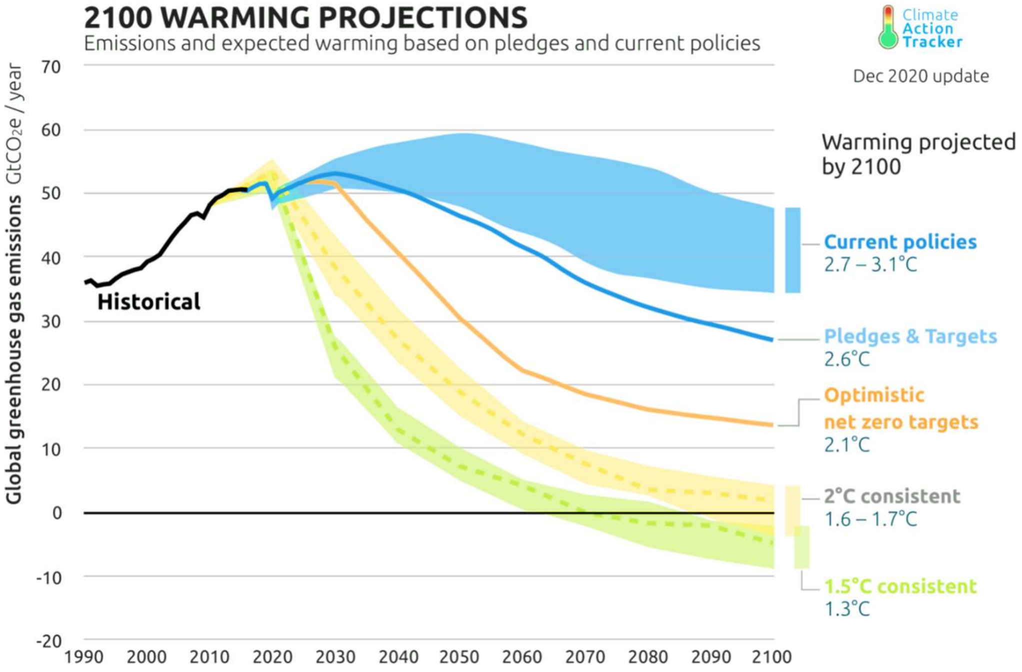

Figure 1.2: *Global greenhouse gas emission pathways [4].*

In the Fifth Assessment Report of the Intergovernmental Panel on Climate Change (IPCC) of 2014, temperatures were expected to rise to 5.8° C by 2100 compared to the pre-industrial era, without implementing any containment policy [2]. To date, the updated data

---

[1] Global Warming Potential (GWP) is defined as the cumulative radiative forcing, both direct and indirect effects, over a specified time horizon resulting from the emission of a unit mass of gas related to some reference gas [CO2: (IPCC 1996)].

provide that it is possible to reach an increase in temperature of more than 3 °C by the same date with the current policies [4]. The Paris Conference of the Parties in 2015 (COP21) sets an ambitious target to keep the temperature below 1.5 hours C to limit global warming, resulting in a reduction in the concentration of CO_2 in the atmosphere. This objective, as can be seen from the current projections, cannot be achieved by continuing with the current policies, but requires further rapid and targeted actions, especially to limit greenhouse gas emissions. Among all human activities, the largest contributor is certainly the energy sector: the generation of electricity and heat heavily affects the total emissions of each continent and it's currently responsible for 73.2% of global emissions [1]. Therefore, it's clear that the energy sector is a key area on which actions can be taken for an effective decarbonization.

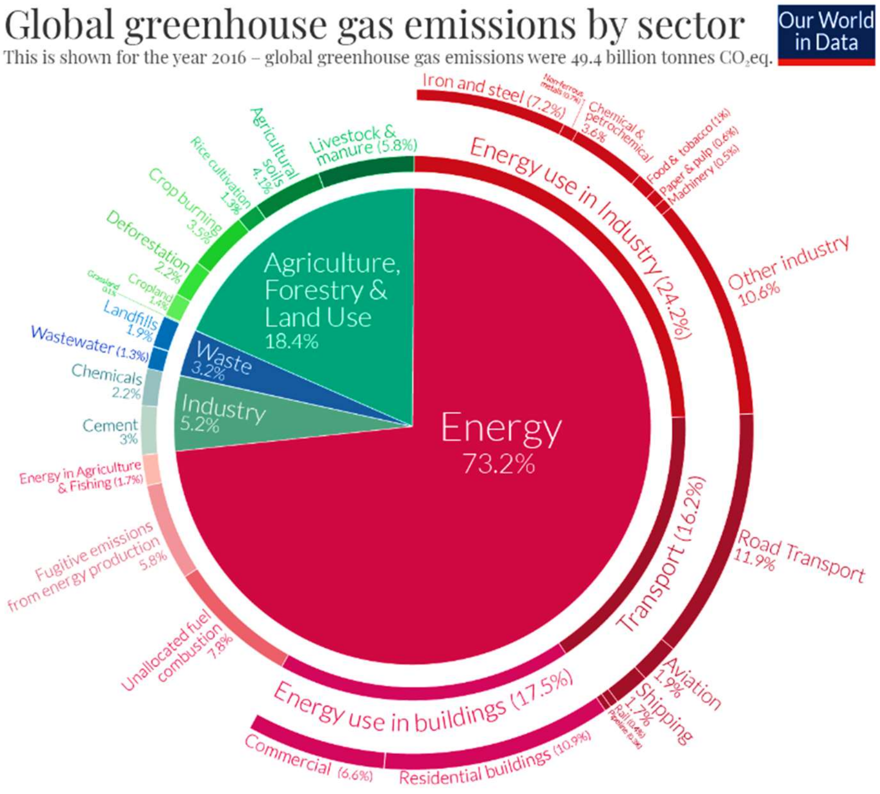

***Figure 1.3**: Global greenhouse gas emissions by sector [1].*

As expressed in the Energy Roadmap 2050 [5], fossil fuels are destined to remain a substantial part of the European Union's energy mix. The available data show that the energy system will be dependent on fossil fuels for many years to come, remaining the main option for electricity generation in the medium and long term and maintaining a share 40-50% in 2030 in energy production. Fossil fuel power plants are considered to be the backbone of the European electricity generation system, with about 50% of total electricity demand supplied, followed by nuclear energy (31%) and renewable energy (13%) [6]. Although to date the use of fossils for energy production has seen a collapse at European level (in particular the use of coal decreased by 19.3% in 2020 [7]), globally still remain the largest source of energy: only Coal accounts for 27% of all energy used worldwide [7], remaining a major component of global fuel supplies, especially in developing countries such as China and India. In addition, the world's energy needs are constantly increasing; according to the IEA Key Statistics 2020 from 1971 to 2019 the primary energy needs (Total Primary Energy Supply) increased from about 230 EJ to about 606 EJ, with a large part of the energy demand satisfied thanks to the use of fossil fuels (about 81%), including coal 26.8%, oil 30.9% and natural gas 23.2% [8].

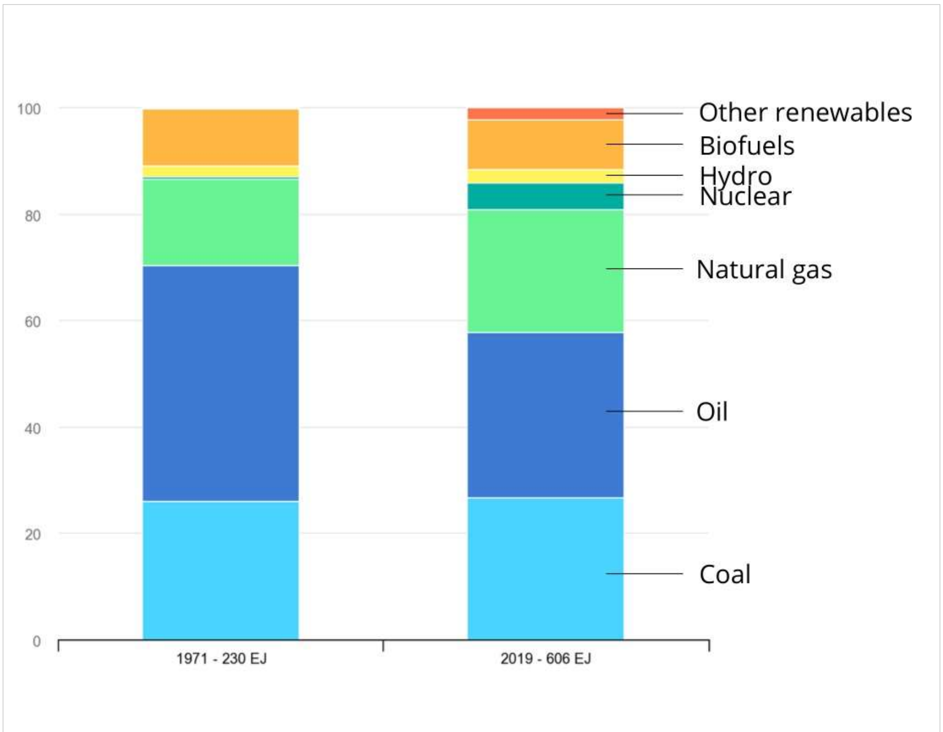

***Figure 1.4**: Global TPES 1971-2019* [8].

In particular, it's interesting to analyze the component related to electricity generation. A massive electrification process has been considered as the most important tool for updating the decarbonization of the energy sector. This leads to an increasing demand for electricity.

To date, coal has always been the world’s leading producer of 36.7% of electricity, followed by natural gas with 23.5% and hydroelectric with 16% [8].

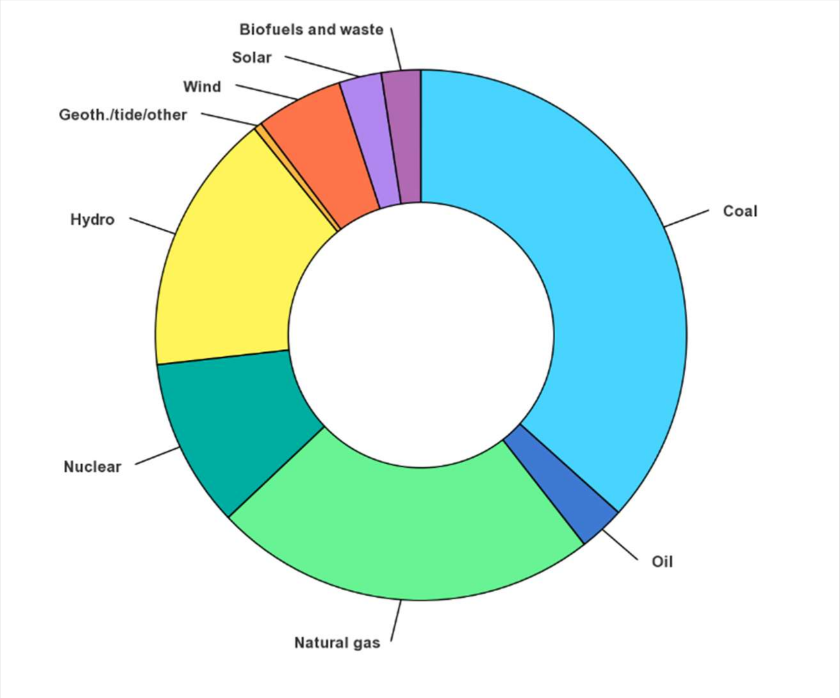

***Figure 1.5**: Global share of electricity production 2019 [8].*

The International Energy Agency (IEA) estimates that electricity generation will increase by two-thirds in 2040, to meet the increase in demand. Similarly, the world’s primary energy demand is expected to grow from the current 13699 Mtoe to 17866 Mtoe in 2040 with an increase of 30.6% predicting a constant significant contribution of fossil fuels [8]. According to these projections, coal, in particular, is expected to cover 23.2% of primary demand in 2040, mainly driven by Asian countries where it is expected to remain the largest source of energy [9]. Therefore coal, as well as other non-renewable sources, will remain a core material in global electricity generation processes; the causes of this situation don’t involve only the economic and technical slowdown given by the necessary remodeling of the entire energy production sector, but a fundamental role is also played by the characteristics of conventional renewable resources, such as solar and wind. These are intermittent resources, which would not guarantee continuity and stability in energy production if not alongside expensive storage devices; moreover, these resources have a very low electric inertia in comparison to conventional heavy generation plants and they can make international grids unstable and prone to failure risks [10]. This explains why fossil fuels are the main source of sustenance of world electricity production. Considering at least the maintenance of current output levels, it's therefore unthinkable to consider an electricity generation from renewable sources alone in a very short period of time. Therefore, in the short-term future, drastic changes in the world energy production sector that would lead to a significant reduction in CO_2 emissions are not foreseen, or at least are not feasible. However, if the target set by the 2015 Paris Conference has to be achieved, other solutions must be considered. In this context, CO_2 capture technologies have been identified as possible solutions to the problem. The combination of Carbon Capture and Storage (CCS) and Carbon Capture and Utilization (CCU) technologies enable carbon dioxide to be captured from the emission sources and subsequently transported by pipeline or ship, and finally, stored in a permanent underground storage rather than its reuse as a useful product, preventing its re-release into the atmosphere and so limiting the climate change of human origin. An added value of the latter type of technology lies in the fact of being able to transform the captured carbon dioxide in products, not only of high commercial value (thus making it convenient the expensive capture technologies), but also useful for the decarbonization of the fuel world: CO_2, together with H_2O is in fact a starting component for the generation of the so-called Green Synthetic Fuels. Green Synthetic Fuels are a type of alternative fuel that play a key role in the transition to a decarbonized energy system, especially in those sectors whose electrification is more difficult; indeed, their importance lies in the fact that they can be used in any field: heat generation and transport sector as well for electricity production, as well to cover peak network loads and thus covering intermittent production of other renewable resources [11]. Among these kinds of fuel, the most important from the commercial point of view is the syngas, which is a mixture of hydrogen and carbon monoxide (H_2 and CO): since it doesn't emit dangerous emissions when producing energy, causing no damage to the environment, syngas has the greatest potential to replace fossil fuels and is the starting point for synthesizing a large number of commercial products, such as methanol, dimethyl ether (DME), ethanol. In particular, DME is very important as it is recognized as a direct and cleaner fuel alternative to conventional diesel [12]. There are several methods for producing syngas. The conventional ones consist in the gasification of biomass and coal or through a steam reforming process of natural gas [13]; however, these solutions are not clean, as they require the use of fossil resources. Syngas can be produced also by exploiting a green, clean resource: the sun. Among the various technologies to carry out this process, Chemical Looping (CL) technologies stand out as economic and sustainable solutions for the splitting of exhaust combustion gases coming from conventional fossil plants, such as CO_2 and H_2O, using high temperature heat from concentrating solar panels (CSP). The syngas thus produced, also called Solar Fuel, will be an alternative fuel produced with clean energy, at high commercial value and with the double advantage of both coming from the recycling of CO_2 emissions and converting solar energy (intermittent and not stable) in a fuel easily storable and transportable.

Chapter 2

2. Literary review

2.1 Carbon Capture, Storage, and Utilization

In the target of arriving to zero CO_2 emissions in the energy sector by 2070 described in the IEA Sustainable Development Scenario (SDS) [14], CCUS technologies account for almost 15%. After years of a declining investment (Figure 2.1), since 2017 a new trend can be observed: in fact, plans for more than 30 new integrated CCUS facilities have been announced for 2020 [15]. The vast majority are in the United States and Europe, but projects are also planned in Australia, China, Korea, the Middle East, and New Zealand. If all these projects will be finished, the amount of global CO_2 capture capacity would more than triple, to around 130 Mt/year (actually CO_2 captured is 40 Mt/year [16]).

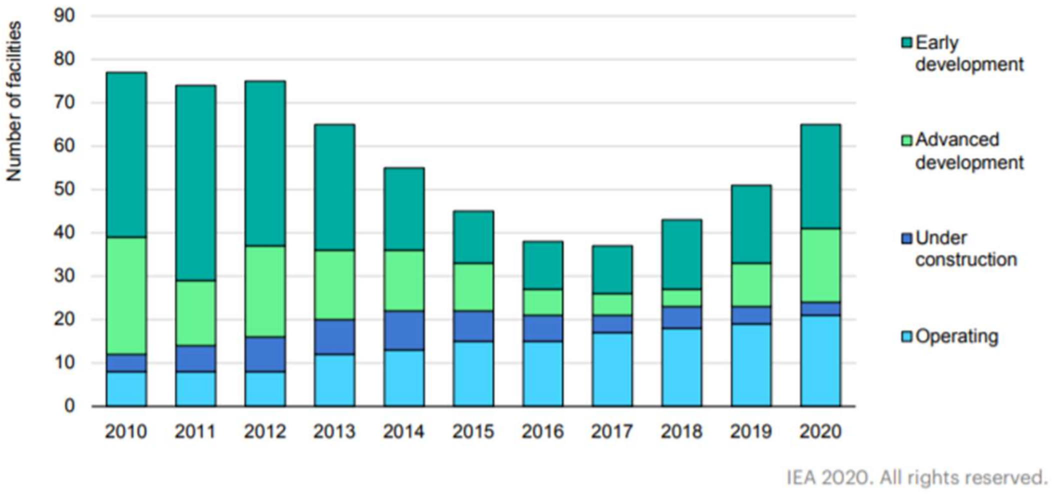

Figure 2.1: *Global large-scale CCUS facilities operating and in development [15].*

Carbon Capture Utilization and Storage (CCUS) is the general term to indicate a set of technologies and techniques that allow the reduction of CO_2 emissions into the atmosphere from large stationary sources, such as power plants fueled by fossil fuels, by means of its capture and subsequent storage or reutilization. This technique allows to continue exploiting fossil fuels but with significantly lower CO_2 emission: for this reason, CCUS can be seen as an important mitigation option in the global transition to a low carbon economy, both in the energy production sector and in industry. The CCUS "chain" consists of three stages: capture, transport, and storage (or utilization).

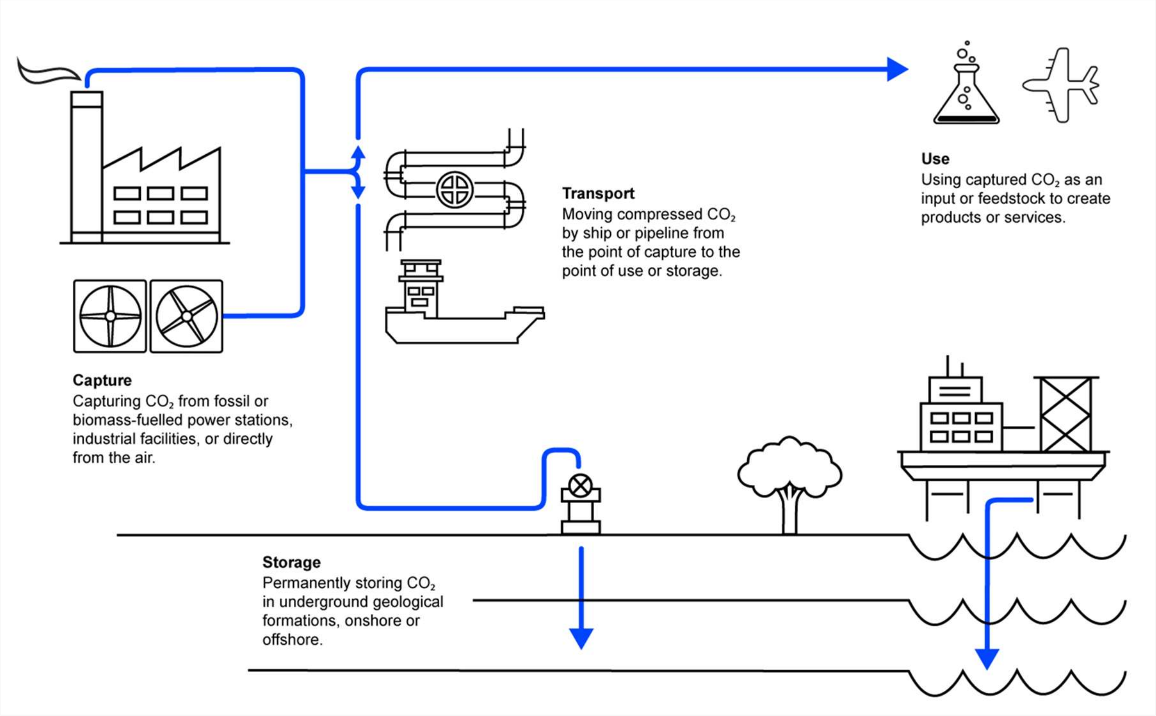

Figure 2.2: *Schematic representation of* CO_2 *pathway in CCUS technologies [17].*

2.1.1 Carbon Capture

There are different methods for capturing CO_2 . The choice of one compared to another is made by analyzing different factors [18]. The most relevant parameters are:

- The nature of the application.
- The concentration of CO_2 in the gas mixture.
- The chemical environment in which carbon dioxide is found: the presence of water vapor or acid species (SO_2,NO_X).
- Physical conditions of CO_2 : temperature and pressure of the environment.

In particular, the concentration of carbon dioxide in the gas flow is a highly relevant factor: high concentrations of CO_2 are much easier to capture and purify than low concentrations. The distinction between the available concentrations of CO_2 in different industrial sectors is important in order to understand how to capture it. Examples of concentrations in different types of plants are shown in Figure 2.3.

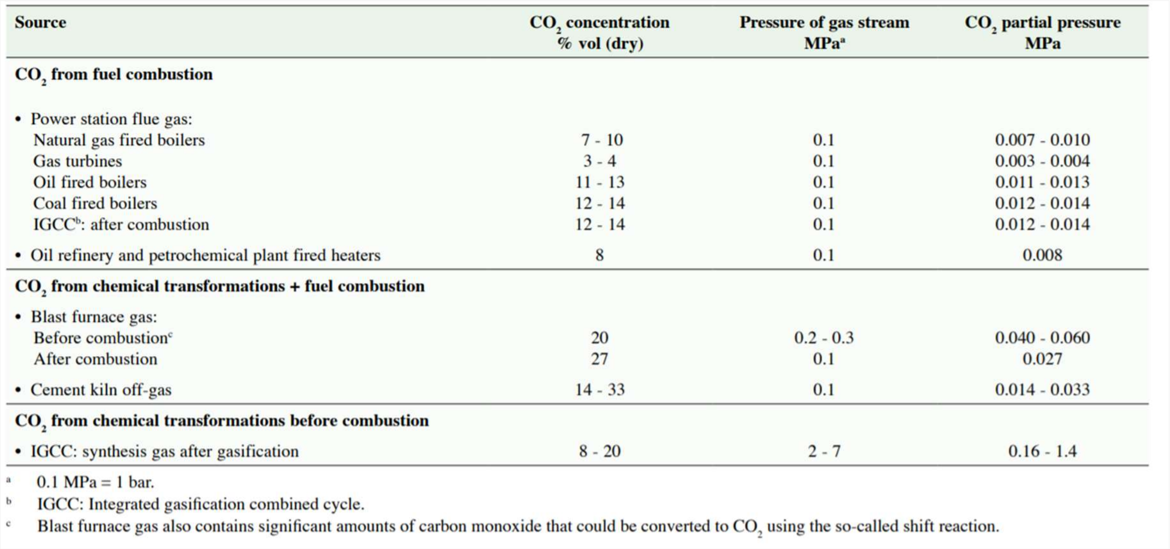

Source	CO_2 concentration % vol (dry)	Pressure of gas stream MPa[a]	CO_2 partial pressure MPa
CO_2 from fuel combustion			
• Power station flue gas:			
Natural gas fired boilers	7 - 10	0.1	0.007 - 0.010
Gas turbines	3 - 4	0.1	0.003 - 0.004
Oil fired boilers	11 - 13	0.1	0.011 - 0.013
Coal fired boilers	12 - 14	0.1	0.012 - 0.014
IGCC[b]: after combustion	12 - 14	0.1	0.012 - 0.014
• Oil refinery and petrochemical plant fired heaters	8	0.1	0.008
CO_2 from chemical transformations + fuel combustion			
• Blast furnace gas:			
Before combustion[c]	20	0.2 - 0.3	0.040 - 0.060
After combustion	27	0.1	0.027
• Cement kiln off-gas	14 - 33	0.1	0.014 - 0.033
CO_2 from chemical transformations before combustion			
• IGCC: synthesis gas after gasification	8 - 20	2 - 7	0.16 - 1.4

[a] 0.1 MPa = 1 bar.
[b] IGCC: Integrated gasification combined cycle.
[c] Blast furnace gas also contains significant amounts of carbon monoxide that could be converted to CO_2 using the so-called shift reaction.

***Figure 2.3**: Properties of gas streams that can be used for capture processes* [19].

Energy-consuming industries, such as cement, steel and iron, and oil refineries, can release as much CO_2 from a single site as a power plant. In some cases, the concentration during the emissions may be higher than that of a power plant, thus making it easier to capture. In this way, some high-consumption industries could offer opportunities for easier capture of CO_2 . Indeed, processes for the production of hydrogen and ammonia already release CO_2 into high concentration streams, making these processes potentially interesting as alternative opportunities for carbon dioxide capture [20]. The other industrial sources of CO_2 are smaller, which makes them less attractive. In addition, the combustion of fossil fuels releases into the air a mixture containing, together with CO_2, also N_2, water vapor, small amounts of O_2 and other elements. Excluding CO_2, the other elements are not greenhouse gases, and therefore do not need to be kept out of the atmosphere. However, element N_2 represents the bulk of the gas flow volume, making the fully storing of the gas flow a non-economic solution, even if it would bring simplification of the CCS plant:

therefore, to catch the CO_2, it is necessary to separate it from the original flow. There are basically three different types of CO capture systems [21].

2.1.1.1- Post-combustion Capture

In this case, CO_2 can be captured by exhaust combustion gases and absorbed into a suitable chemical solvent. CO_2 is then separated from the solvent and compressed to be transported and stored. Indeed, since the exiting gases have a low pressure and a relatively low molar fraction of CO, the best system available for separation is the chemical one, which uses absorption systems based on the use of aqueous solutions and chemical solvents. The post-combustion systems are much easier to apply because they provide for limited interventions on the existing plant: it is necessary to add a section downstream of the pollutant abatement line, where the fumes are treated to separate the carbon dioxide. In addition to presenting the indisputable advantage of being applicable to existing plants, this technique allows also to achieve capture efficiencies exceeding 90% [18]. Different separation techniques are available: chemical absorption by aqueous ammonia, amine-based solvents such as monoethanolamine (MEA), diethanolamine (DEA), and N-methyldiethanolamine (MDEA) and alkaline solvents such as $Ca(OH)_2$ and $NaOH$ are the most common methods for post combustion capture in various industries, including cement, iron and steel, power plants, and oil refineries [22]. An innovative form of this type of capture consists in the use of more advanced sorbents; adsorption systems with solid sorbent are indeed innovative process whose main difference, compared to the conventional one, is the type of dilution medium: the amines are anchored on a porous solid support (solid sorbent) instead of in aqueous solution. The process takes place in two stages. At first the fumes pass through a fixed bed formed by the solid sorbent in granular form: the carbon dioxide is absorbed by the amine dispersed on the surface of the grains and the fumes, free from the CO_2, go to the chimney. Then the solid sorbent is regenerated, releasing the CO_2, which is sent to the confinement, ready for a new absorption cycle. It is in this phase, which is less energy-intensive, the main advantage of this technology compared to the conventional one. Moreover, this process does not have typical drawbacks of the conventional process: the onset of corrosion, the formation of foam and the degradation of the solvent that pollutes the environment [23]. Usually, the adsorbents are classified basing on the temperature in high-temperature or low-temperature materials. The first materials include hydrotalcites, alkali or alkaline-earth oxides such as calcium oxides, alkali silicates and zirconates, as well as double salts; on the other hand, low-temperature adsorbents use porous materials such as zeolites, carbon-based, MOFs, porous polymer networks (PPNs), and covalent organic frameworks (COFs) [22].

2.1.1.2 Pre-combustion Capture

The fuel is converted before combustion into a mixture of hydrogen and carbon dioxide using a gasification (if the fuel is solid) or steam reforming (for natural gas). This kind of capture is usually implemented in combined plants, such as IGCC (Integrated Gasification Combined Cycle) [24]; captured carbon dioxide can be transported and stored, while hydrogen can be used as a fuel for the production of electricity or to power hydrogen cars. The capture in this case can be performed both using physical absorption process (the solvent used is an aqueous solution with 40% MDEA (mono-diethyl-amine) and membrane separation: in fact, since the gas is captured before the combustion, membranes are more suitable for high-pressure precombustion processes such as IGCC. These membranes allow a selective separation of gases: the membrane is permeable only to the species that we want to separate from the fed current. The driving force of the process is the different partial pressure of the permeable species between fed gases and permeated. Generally, the use of membranes for gas-separation applications can offer an approach that is more energy efficient and environmentally friendly than other separation methods [25].

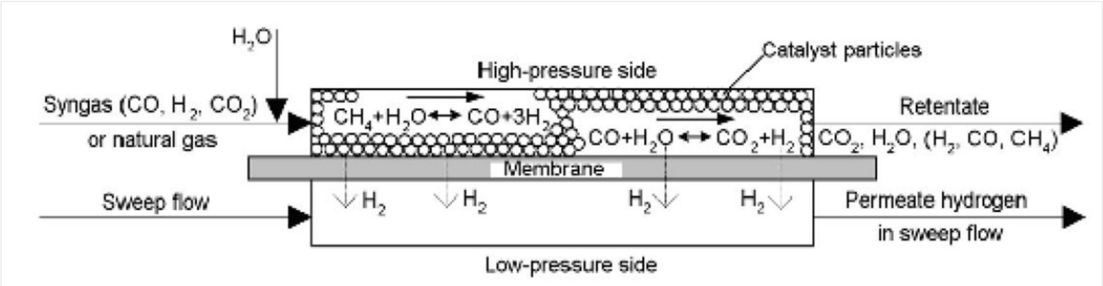

Figure 2.4: *Working principle of a hydrogen separation membrane* [25].

The application of membrane technology for post combustion CO_2 capture is very challenging mainly because of the low pressure of flue gas streams. Membranes can be inorganic or organic, depending on the material used; typically, porous inorganic membranes are composed of zeolites, metal–organic frameworks (MOFs), carbon molecular sieves (CMS), ceramics, and a few oxides (such as titania, zirconia); their advantage is the ability to withstand high temperatures and often have higher mechanical stability, but their cost is so high to limit the commercialization. Conversely, organic membranes (polymeric membranes) can be easily synthetized in porous fiber modules and show a bigger potential for large-scale industrial applications. However, polymeric composite membranes have lower performance of separation in comparison to inorganic membranes [22]. In case of pre combustion too, the capture can be performed using solid sorbent; an innovative approach reported in literature is the SEWGS (Sorption Enhanced Water Gas Shift): the idea is to capture CO_2 in WGS reactors by subtracting it from the reaction phase so as to push the balance of this reaction towards the products. Carbon dioxide is captured by adsorption using a suitable material: Potassium Promoted Hydrotalcite (K_2CO_3). Once saturated, this sorbent is regenerated using Pressure Swing Adsorption (PSA) methods [26].

2.1.1.3 Oxy-combustion Capture

This process involves the use of pure oxygen, or highly enriched air, in the combustion chamber. This type of combustion mainly produces steam and concentrated carbon dioxide, easier to process and send to storage. In fact, the concentration of CO_2 in the gas flow is, as we have seen, a key factor that determine the cost of the capture process: the greater its concentration, the simpler (and therefore cheaper) its removal will be. If a fossil fuel is burned in pure oxygen, the burning temperature is very high, but if some combustion gas is recycled into the combustor, the temperature can be reduced to a level similar to that in a conventional combustor; the combustion products that are obtained are a prevalent mixture of H_2O and CO_2 and in smaller quantities from SO_2 and NO_X, N_2, O_2 in excess.

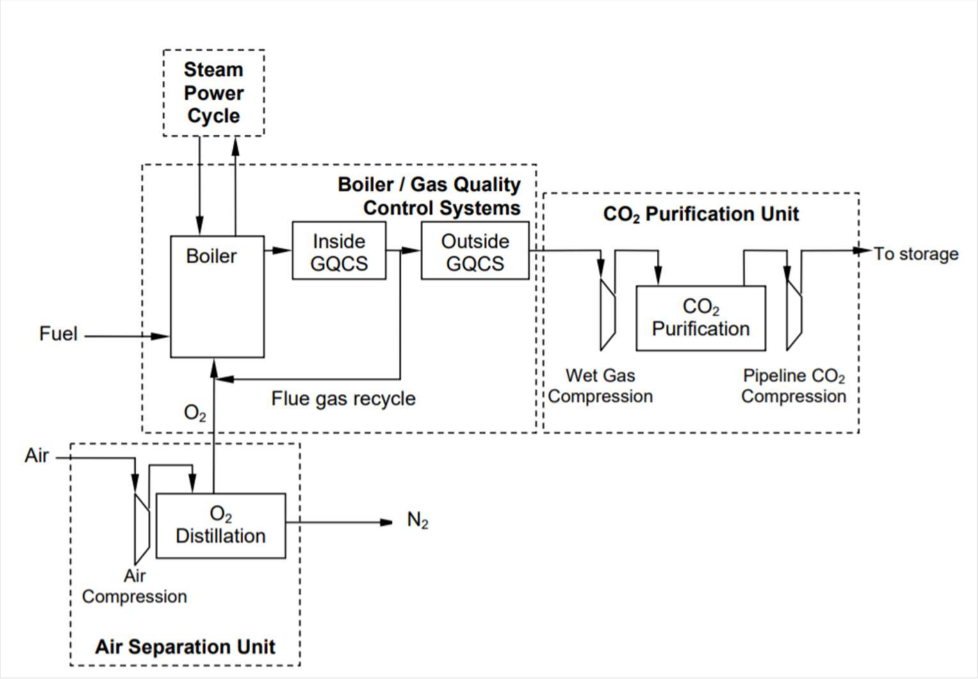

***Figure 2.5**: Oxy-Combustion Power Plant Simplified Block Diagram* [27].

From these combustion flues, the separation of carbon dioxide is very simple: in fact, by cooling down, the water condenses and can be removed. This type of technique, with current technologies, can be used with coal cycles [23]; the application to gas cycles is not convenient, because the turbomachines and the combustor would have to operate with gas flows with a very different molar composition. An oxy-fuel combustion plant has an advantage: it can potentially be without chimney and zero emissions into the atmosphere. It is also a technology that can be applied to existing power plants, without changes to the power cycle but only to the boiler. The energy disadvantages of the plant are due to the ASU (Air Separation Unit), which absorbs a significant fraction of the work produced by the power cycle [28].

2.1.2 Carbon Storage

Once the CO_2 is captured, it is compressed or liquefied in order to make its transfer easier. The main difference between these two options regards the fact that a liquefaction approach makes the following compression easier with a pump and less expensive in terms of energy than a compressor; however, it requires a refrigeration system, which add complexity to the system [29]. After this last step, CO_2 is transferred (with pipelines, rather than with ships) toward the occurring site. One of the main options is to store the CO_2 captured in natural reservoir usually underground. For a capture capable of substantially modifying overall emissions, storage tanks shall have sufficient capacity to retain a significant fraction of global CO_2 emissions (currently around 31.5 Gt/a [30]). The assessment of many of the options available indicates that for this purpose only certain natural reservoirs have sufficient capacity and the right characteristics: in fact, in order to make its storage against climate change effective, CO_2 has to be stored for a large number of years. Therefore, the basic requirement of each storage facility is that certain conditions, such as the presence of a physical barrier, must be met to ensure that they remain in the tank. Currently known geological storage methods are:

Deep salt formations. Saline formations are rock formations saturated with water, in which are dissolved high amounts of salts. For the storage of CO_2, they shall have the following requirements:

- impermeable rock layers at the top to prevent the return of the injected CO_2;
- geological stability, to avoid cracking of the impermeable layer;
- adequate thickness and porosity to ensure high storage capacity.

With these requirements it is estimated that there are basins with a storage capacity of 1,000 billion tons [21]. The CO_2 injected in these deposits tends to reach the upper layers due to its lower density than the water present, but the confinement is guaranteed by the layer of compact rocks above.

In ocean depths. The oceans represent an enormous potential for the storage of the CO_2 produced from the activity human. Already the oceans contain the equivalent of about 140,000 Gton of CO_2. Once liquefied carbon dioxide can be easily transported via pipeline and be reinjected underground, dispersed in the seabed at depths between 1000 and 1500 meters, presumed sufficient to exclude the possibility of return to the surface. The passage of CO_2 from the earth's atmosphere in the oceans occurs naturally, but very slowly, therefore the injection of carbon dioxide into the deep seabed would represent the acceleration of a natural process: it is assessed that injecting CO_2 into the depths of the oceans, this could stay there for over 1000 years [31].

In exhausted oil and gas wells, un-exploitable coal fields, un-exploitable geothermal fields. There are several estimates of containment capacity worldwide: IPCC (2005) estimated a storage capacity of over 1,800 Gt CO_2 for oil and gas exhausted fields only: this quantity could cover the worldwide production of carbon dioxide over a period of over the next 30 years, and far greater seems the potential of saline aquifers and ocean storage [21].

All these options are known as CCS (Carbon Capture and Storage) and alone has the capacity to cut the CO_2 emission in the atmosphere, since there is plenty of capacity underground to store it. But capturing CO_2 to hide it underground is a like managing waste by simply dumping it in a landfill: high investment, high operating costs, and the needing of a continuous, permanent monitoring of underground storage sites, to prevent possible dangerous leakages. Conversely, using the same approach of wastes, also carbon dioxide can not only be eliminated, but used and transformed into something useful. This is an essential element of the circular economy.

2.1.3 Carbon Utilization

The technologies aimed to recycle the captures CO_2 are known as CCU (Carbon Capture and Utilization). This is another option compared to simple storage and consists in the possible reuse of CO_2.

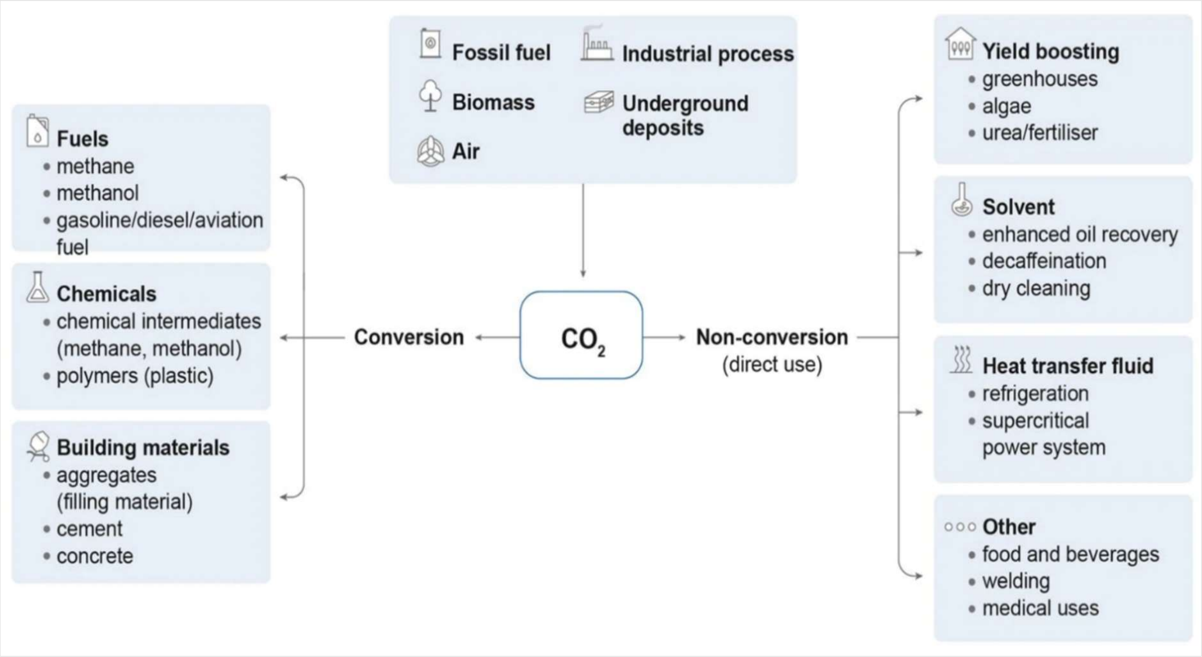

Figure 2.6*: Simple classification of pathways for CO_2 re-use* [17].

As it can be seen in Figure 2.6, once captured CO_2 can follow many different pathways in its way toward recycling. Some of these technologies are well known and already used in reality, some are still concept being studied in laboratories. In the following, some of the more important processes are summarized.

2.1.3.1 EOR and EGR

Enhanced oil/gas recovery (EOR/EGR) refers to the processes where CO_2 is injected into a reservoir to repressurize rock formation and to release any oil/gas that may have been trapped in the formation. In this way the carbon dioxide recovers gas/oil that otherwise would have not been extracted. Usually, the stream is then pumped to the surface, and the CO_2 emerging with the oil is separated and resupplied into the cycle to repeat the process [22], [32].

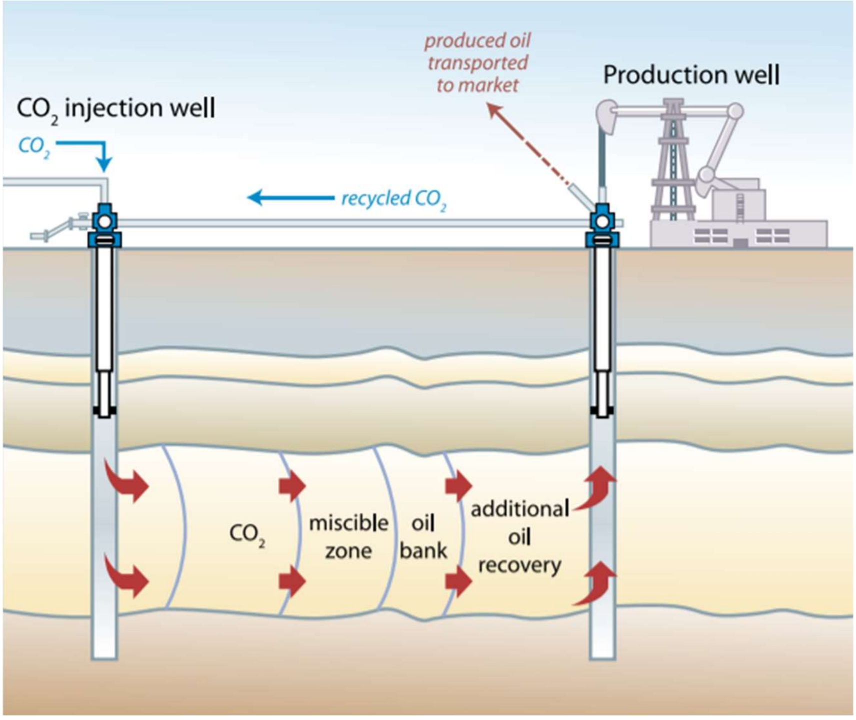

***Figure 2.7**:Concept of EOR process* [21].

Injection of CO_2 into suitable depleted deposits can increase oil recovery by 10-15% of the oil originally extracted [33]. If the technique is used in combination with CO_2 storage, the additional oil production can partly offset the cost of capturing and injecting CO_2. This storage technique has the advantages of using tanks that have already contained fluids for thousands of years, without significant losses; furthermore, there are already some of the tools needed for injection in the site. This technology is well known in petroleum process since 80s: as example, around 33 million tons of CO_2 per year have already been used in more than 74 EOR projects in the United States [34].

2.1.3.2 Enhanced Coal Bed Methane (ECBM)

A further method of storage is to use unexploitable coal beds. Coal has the characteristics of having a good permeability and many microporosities, within which gases can spread. CO_2 can then be injected into appropriate coal beds where it will be adsorbed, so as to be permanently blocked, provided that the coal is never extracted. Furthermore, within the microporosity of coal in the deposits, methane is trapped among the gases: by injecting

CO_2 into carboniferous veins, it can be released. So, as in the case of the EOR, even storage of CO_2 may result in the extraction of a hydrocarbon as a by-product, thus adding economic value which could decrease the costs of CCS. Coal can adsorb about twice as much CO_2 as methane, although this ratio varies depending on the type of coal and its location. This technique is currently in its infancy and a reliable estimate of the amount of methane that can be recovered is not yet available. Among all the technologies is in fact the one that presents the greatest number of unknowns, because it is not known the actual process of liberation of the gases and it is not known whether the structure of the coal, trapping the CO_2, can alter its mechanical properties. The ease with which CO_2 can be injected into the coal will be determined, among other factors, by the permeability of the coal itself [21].

2.1.3.3 CO_2 in chemical industry and other use

The chemical industry consumes almost 28% of the industrial and 10% of the global final energy [35]. Most of this energy is obtained from oil and other fossil resources. CCU technologies can substitute the conventional production of various chemicals including basic chemicals, fine chemicals, and polymers. Indeed, today around 230 Mt of CO_2 are used each year in this sector [36]. The largest consumer is the fertilizer industry, where around 130 Mt CO_2 per year is used in urea manufacturing, followed by the oil sector, with a consumption of 70 to 80 MtCO_2 for enhanced oil recovery [17]. CO_2 is also employed widely in food and beverage production, the fabrication of metal, cooling, fire suppression and in greenhouses to stimulate plant growth. It can be used as an alternative to fossil fuels in the production plastics, fibers, and synthetic rubber. Unlike the conversion of CO_2 to fuels and chemical intermediates, polymers from with CO_2 require little energy input, because CO_2 is converted into a molecule (carbonate) with an energy level that is even lower[37]: polymer processing is very important in the concept of recycling of CO_2, because is a product very competitive in the market since it has high market value and needs low energy to be produced. Another option for CO_2 re use is in the production of building materials to replace water in concrete, called CO_2 curing, or as a raw material in cement and construction aggregates [36]. CO_2-cured concrete is one of the most mature and promising applications of CO_2 use, while the integration of CO_2 in the production of cement itself is at an earlier stage of development.

Finally, there is another important sector in which CO_2 can be used: the production of alternative fuels. Bio- fuel or green synthetic fuel represent a good option among all the CCU solutions since they use the captured CO_2 from present fossil emitters to replace fossil fuels. CO_2 is used to create biofuel by enhancing yields of biological processes, such as algae production and crop cultivation in greenhouses; biofuels are then produced by this biomass and they include methane, ethanol, biodiesel, etc. [28]. In addition, green synthetic fuels will be described in the next chapter.

2.2 Dissociation processes for CO_2 re-use: Green Solar Fuels

As it has been described in the previous paragraph, the main advantage of CCU compared to CCS is that CO_2 can be transformed in fuels or other raw chemicals; one of the most important solution consists into the dissociation of CO_2 to form syngas. Syngas (Synthetic gas) is a mixture of H_2 and CO: its relevant role comes from the fact that can be used as fuel itself or as starting material for other chemical production. Ethanol, methanol, dimethyl-ether (DME) are all possible results of syngas processing, as well as other synthetic liquid fuels obtained with the Fischer-Tropsch (FT) technology; in this case, a catalytic chemical process converts syngas into mainly liquid hydrocarbons with different molecular weight, depending on operating parameter as temperature or catalyst [38]. Fischer-Tropsch diesel, methanol and DME are the most interesting fuels: methanol, for example, can be mixed with unleaded gasoline to create a fuel that can be used in conventional engines with small modifications; dimethyl-ether can substitute diesel with further modification to the engine [39].

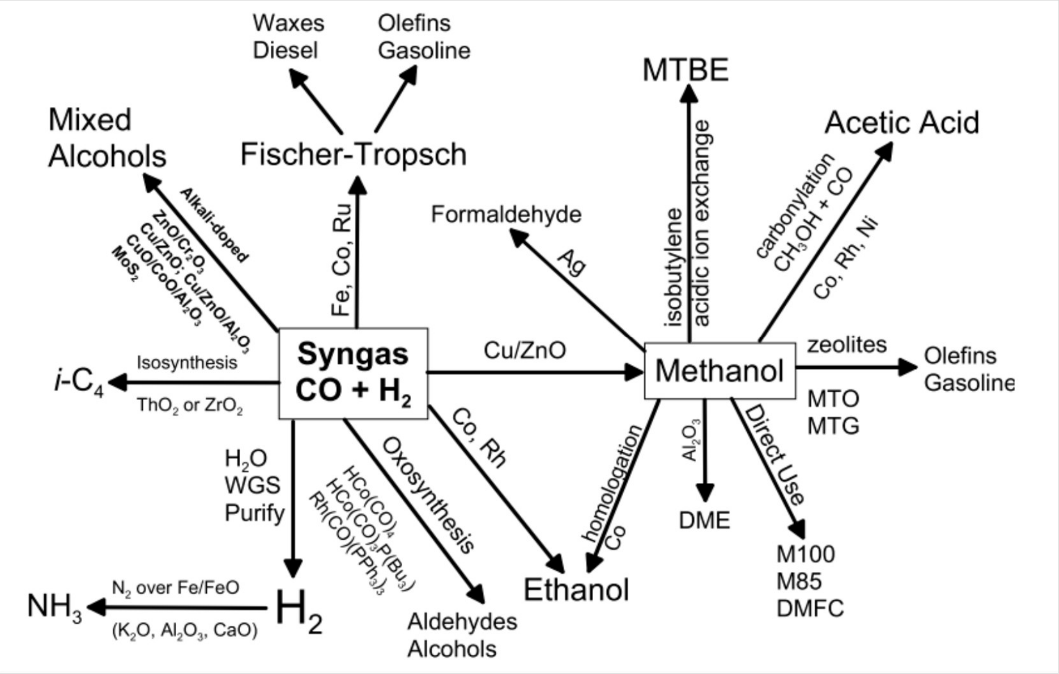

Figure 2.8*: Chemical production from syngas* [164]

All the processes of dissociation of CO_2 are endothermic, thus require external heat. The heat required can be provided by solar energy, using high temperature heat coming from CSP technology: when the used power source to produce energy carriers is the solar radiation, the products are called Solar Fuels [40]. Combining solar energy with the production of fuels has a double advantage: besides the mitigation of environmental issues thanks to avoiding CO_2 releasing in the atmosphere, it also provides a new pathway for energy storage: highly variable solar energy is indeed stored in chemical form [41]. There are four main alternatives for CO_2 conversion [42]:

- Hydrogenation.
- Photo electro chemical process.
- Electrochemical process.
- Thermochemical process.

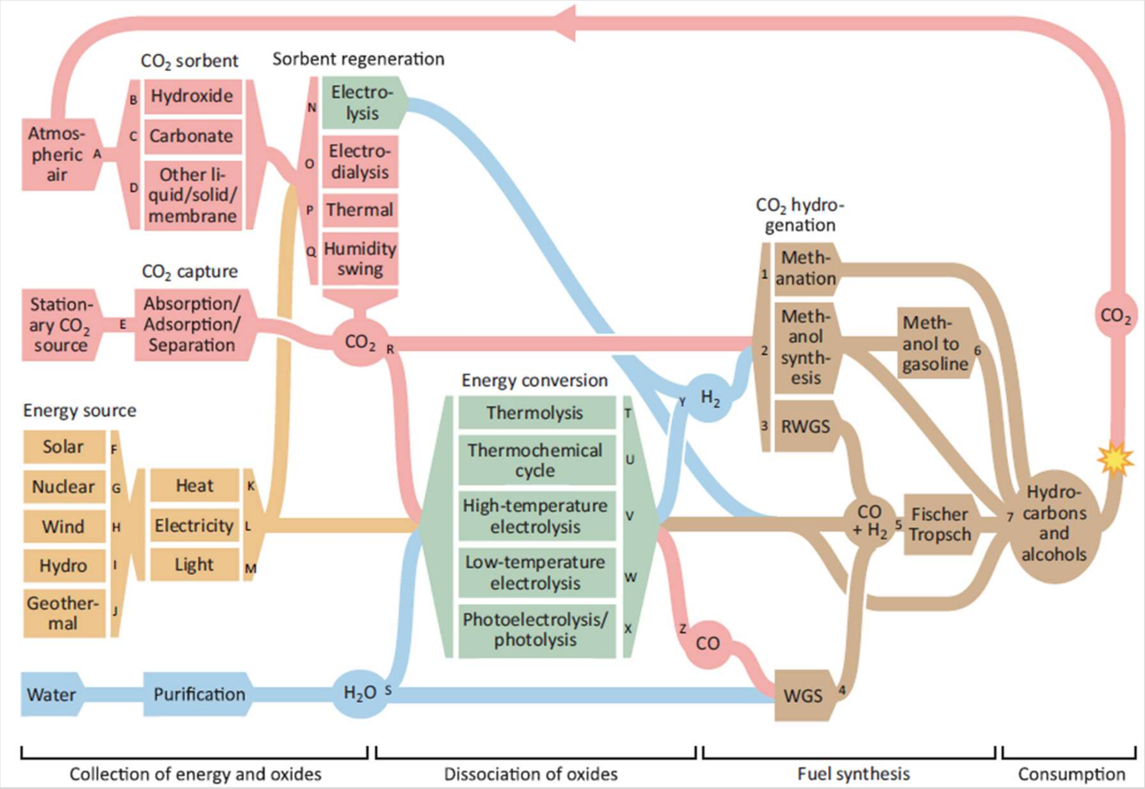

Figure 2.9: *CO_2 and H_2 dissociation pathways* [43].

Hydrogenation is the process in which CO_2 is reduced into CO using hydrogen or hydrocarbons (usually CH4): in fact, when CO_2 is combined with methane, syngas is produced [44] according to the following reaction:

$$CH_4 + CO_2 \rightarrow 2CO + 2H_2 \qquad (2.1)$$

Using H_2 produced with renewable energy resources is also an interesting solution: chemicals and fuels (formic acid, methanol, higher alcohols, higher hydrocarbons) are produced, while CO_2 emissions are reduced, and the shortage of fossil fuels is covered [45]. The main drawback of this kind of processes regards the high cost of hydrogen and hydrocarbons [46].

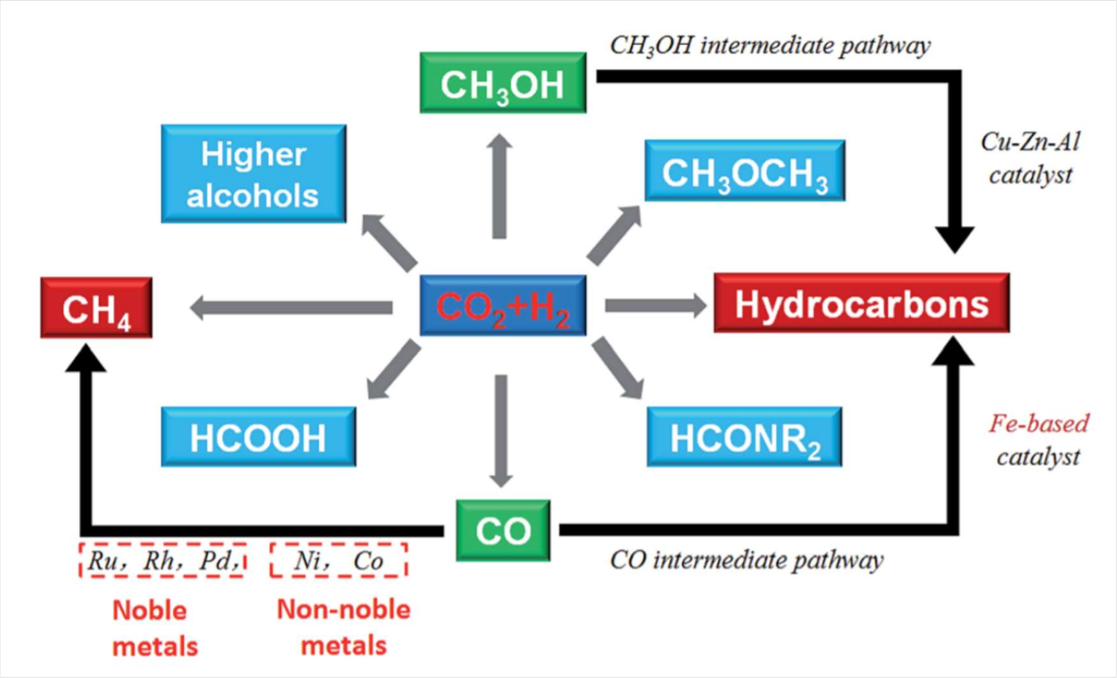

Figure 2.10*: Conversion of CO_2 to chemicals and fuels through hydrogenation with H_2* [47].

The solar photo-electrochemical process splits the CO_2 (or mixture of CO_2 and steam, or just water) using a part of the solar spectrum absorbable by a photocatalyst or sensitizer, in order to produce syngas or hydrogen [46]. The most important components of this process are the light absorbers and the electrocatalysts [48]; especially for the catalyst, the research is studying the possible use of some earth abundant materials [49], [50]. The main problems linked to the photocatalysts are the low selectivity, the lack of solar light utilization and the high tendency to charge recombination [50]. The selectivity can be increased by using a good semiconductor: graphite-like carbon nitride ($g - C_3N_4$) has been considered as good catalyst because of its high stability and low cost [51]. Direct photoelectrochemical splitting is also considered to have several advantages in comparison to electrolysis, where light absorption and electrocatalysis are not integrated in the same device: in addition to the minor cost of the whole system, with PEC (Photo Electro Chemical) a current density smaller than electrolyzers' is used (10-20mA/cm2, almost 100 times smaller), thus increasing the internal efficiency [52].

The already commercial electrolysis uses electrical energy to boost a non-spontaneous reaction, in order to split H_2O and CO_2. The device in which it is performed is a solid oxide electrolyzer (SOEC), where high temperature required for this kind of electrochemical splitting are reached [53]: the lower the temperature, the lower the efficiency of the reactions, resulting in slow kinetic. However, the most part of the losses happens in the solar-to-electricity process. This electricity can indeed be produced by means of PV panels or by solar thermal power plants: for both of them, the conversion performance is limited [54].

If we want a process of dissociation with high efficiency, we need to consider solar thermochemical processes. They use concentrated solar energy coming from CSP systems to perform the reactions (endothermic or exothermic) needed in the process to generate syngas and reach high overall efficiency ($\eta \sim 52\%$) [55]. Five different paths can be followed for the thermochemical production of solar fuels: reforming, cracking, gasification, thermolysis, thermochemical cycles [56]. Only the last two mentioned are emission-free methods, while the other three use fossil fuels and water, or mixture with CO_2 to produce H_2 and syngas, producing GHG emissions, even while using solar energy to drive the process: their only advantage in comparison to thermolysis and thermal cycles is that their technology is well mature and can be implemented in large scale [56]. On the other hand, thermolysis and thermochemical cycle only use water/ CO_2 and concentrated solar energy, resulting in a 100% clean process.

Thermolysis is the process of direct dissociation of CO_2 and theoretically is the simple way to break the molecule. The molecules splitting follows the reaction reported in the following equations (*Reaction 2.2* for the CO_2 direct dissociation, while *Reaction 2.3* for water dissociation).

$$CO_2 \leftrightarrow CO + \frac{1}{2}O_2 \tag{2.2}$$

$$H_2O \leftrightarrow H_2 + \frac{1}{2}O_2 \tag{2.3}$$

However, these reactions require extremely high temperature (even higher than 2500 K), and the products must be kept strictly separated to avoid their recombination and avoid explosions [42]: so, in practical condition, the realization of the process is quite difficult and requires really high costs using current technologies. Tou et al. [58] experimentally demonstrated a single-step continuous splitting of CO_2 using a solar-driven ceria membrane reactor. The CO_2 is dissociated into two separate streams (CO and O_2) operating at isobaric and isothermal condition: in particular, the solar reactor temperature is kept at 1600° C, while the pressure at $3 * 10^{-6}\ bar\ p_{O2}$. In Figure 2.11, a schematic of the used reactor is showed.

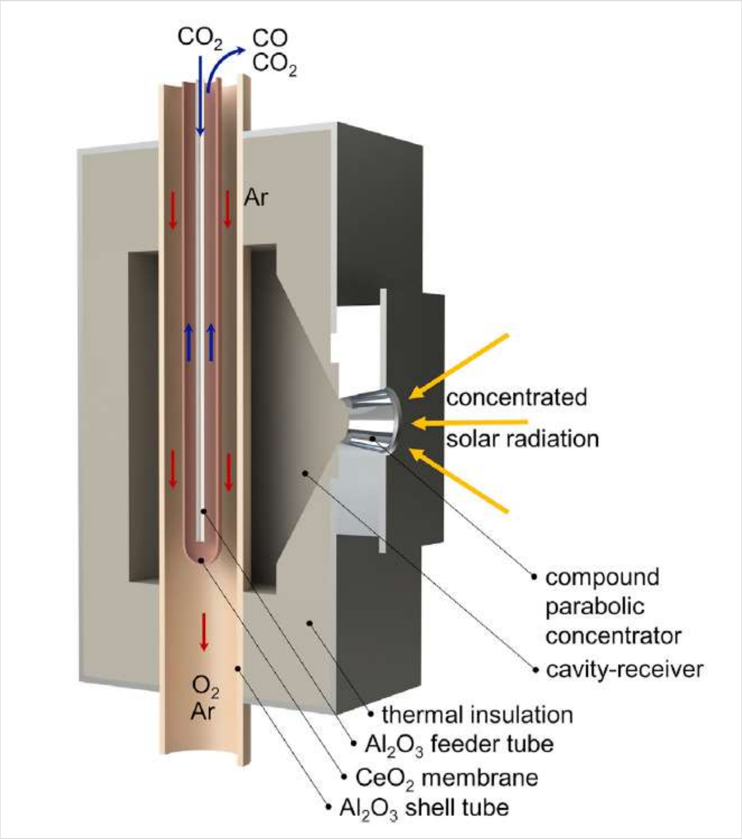

Figure 2.11*: Schematic of the solar reactor: it comprises a cavity-receiver containing a membrane of ceria, enclosed by a coaxial alumina tube. CO_2 is supplied to the inner side (oxidation side) while sweep inert gas is supplied to the outer side (reduction side) to control the oxygen partial pressure* [57].

This study experimentally demonstrated for the first time a single step CO_2 dissociation, but it needs further optimization in order to result feasible for a commercial utilization. Indeed, the resulting solar to fuel efficiency of this simulation is found to be less than 1%, while the theorical value at 1600°C should be around 40%, according to other comparable studies [58].

To overcome the problems of direct, one-step dissociation, thermochemical cycles are considered: they are multi-step processes with higher efficiency in which the problem of separation is by-passed, and the temperature required is lower [42]. This method, also called Chemical Looping (CL), basically consists in the production of CO and H_2 by exploiting the capacity of some material to assume different state of oxidation. The process is explained more in detail in the next chapter.

2.3 Chemical Looping Technology

Chemical Looping is an emerging technology that can be used in a different range of application for fuels, chemicals, and electricity production, ensuring to these processes a key role to reduce the CO_2 emission and to fight global warming [59]. During the process, the chemical reaction is divided into multiple sub reactions: each of them can be performed in a reactor or in different reactors. The link between the reactors is provided by an intermediate material who is able to assume different level of oxidation and exchange actively oxygen during the steps. The material (also called Oxygen Carrier) is typically a metal oxide and by circulating undergoes reduction and oxidation reaction, regenerating at the end of the cycle. The main characteristic of chemical looping processes is the typically high efficiency: they can be designed in a way that the energy and exergy losses of the overall process are minimum; another advantage is that the reaction can be performed in different reactors, overcoming all those problems linked to the management of the undesired mixed products, thus yielding to an overall efficient, low-emission process [60]. As an example, if chemical looping is used for a combustion process, the fuel and the air never mix: this is important, because it means that at the end the fuel combustion takes place in absence of nitrogen and so the flue gases are only CO_2 and vapor, easy separable by condensing [61]. Chemical looping is indeed an option considered in the Carbon Capture pathway [62]. In addition, there is actually a wide range of intermediates that can be used for the technology: that's why chemical looping is a very flexible and versatile process that can be used in a lot of different applications. The more interesting are: Chemical looping gasification; Chemical Looping Reforming (CLR); Chemical Looping air separation for oxygen production in oxy-fuel or IGCC operations; Chemical looping removal of ventilation air methane (VAM) in mining operations; Chemical Looping Combustion (CLC) [60]. Gasification with chemical looping, CLR and CLC are all considered as pre combustion CO_2 capture technique.

For what concern the gasification via using chemical looping, there are two main kinds of process: Syngas Chemical Looping (SCL) and Coal Direct Chemical Looping (CDCL). During these processes, carbonaceous fuels are converted to products as electricity, hydrogen and other synthetic fuels using a specific chemical intermediate [63]. The advantages of gasification instead of the typical coal-fired power plant, where the combustion fully oxidize the fuel to generate high pressure steam, which presents a corrosive nature (thus limiting the operative temperature and so the efficiency of the process), are well known. The implementation of CL concept in gasification methods can help to achieve the intensification and a more efficient carbon capture process [64]. In fact, it uses specially developed metal oxides to produce hydrogen and concentrated CO₂ in two separate reactors, exiting in two different streams and so avoiding costs of additional carbon separation.

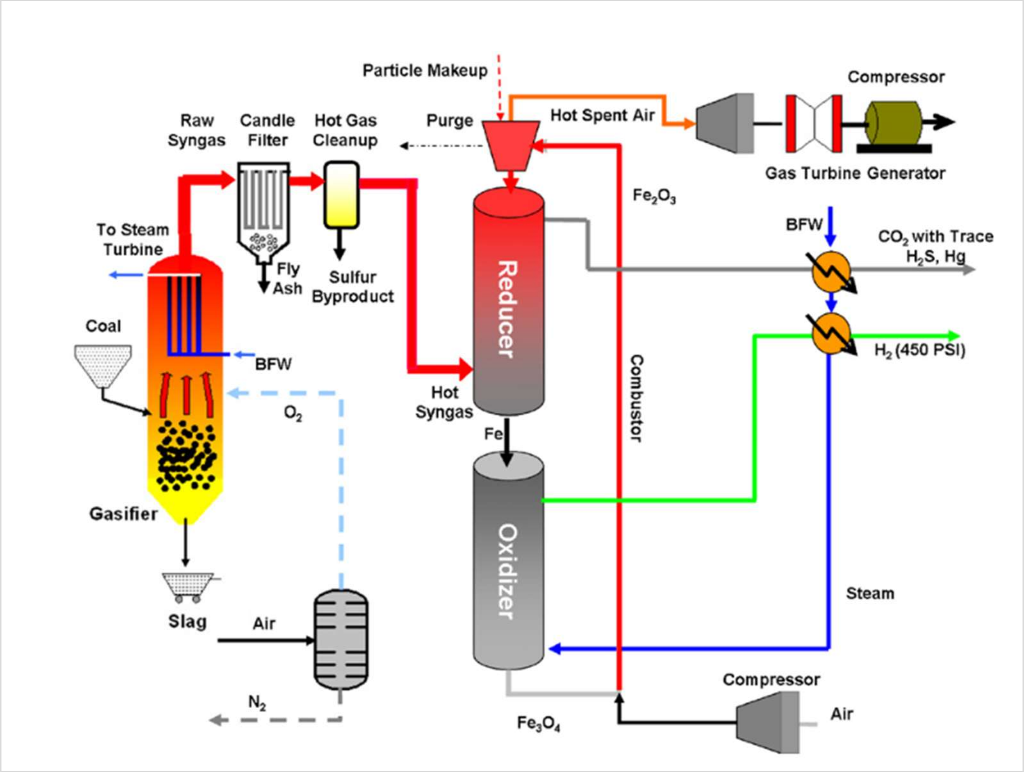

***Figure 2.12**: Simplified schematic of the syngas chemical looping process for hydrogen production from coal* [63].

In the SCL process the coal or biomass is firstly gasified and turned in syngas, then the hot syngas is sent to the reducer (Figure 2.12). In comparison to the traditional pathway coal-to-hydrogen (very complex system [65]), the SCL process uses only three main units to obtain the same output [63]. The coal direct chemical looping (CDCL) on the other hand uses iron-based materials for direct coal gasification: the main difference respect to SCL, which employs conventional system for the gasification part, is that CDCL uses coal directly as feedstock rather than syngas, leading to a minor oxygen consumption and to the intensification of the process [66]. In Figure 2.13 a simplified representation of the process is showed: in the coal reactor, coal is converted into water and CO_2 while reducing the iron oxide (Fe_2O_3) to Fe and FeO, which are then reoxidized in the hydrogen reactor into the Fe_3O_4 particles and finally to Fe_2O_3 again in the fuel reactor (3 step chemical looping process).

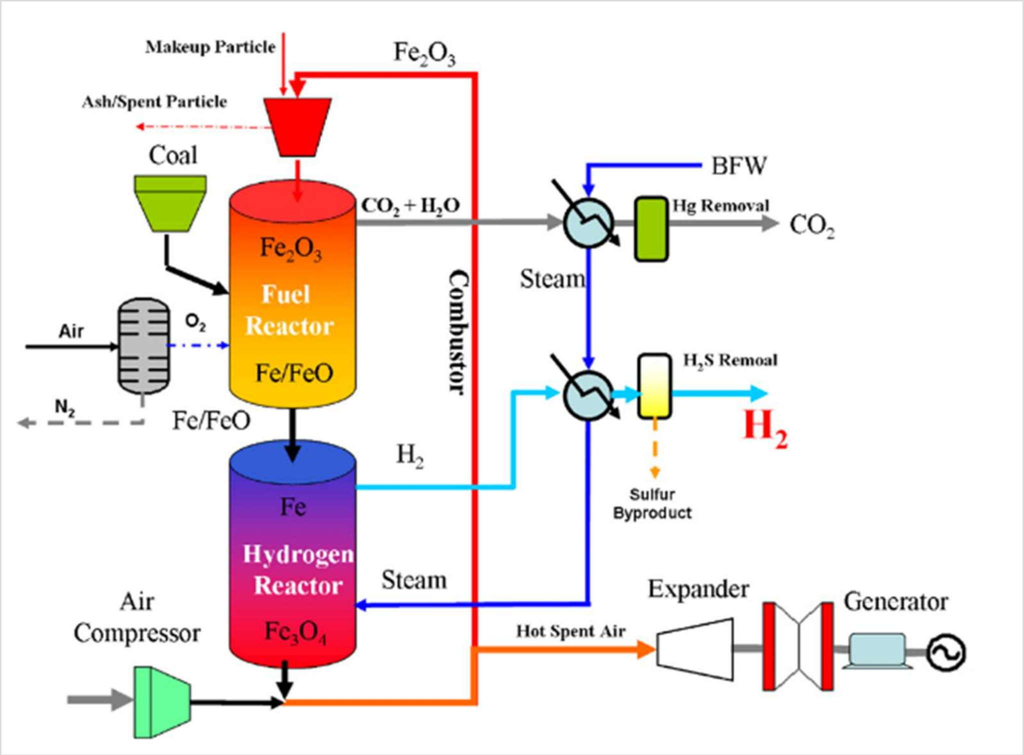

Figure 2.13: *Simplified schematic of the coal direct chemical looping (CDCL) system* [63].

Chemical looping gasification is a promising technology for biomass too, in which oxygen carriers continuously supply oxygen for the gasification of the biomass: in this case the added value is that the reduced oxygen carrier can be a good catalyst for biomass tar and char cracking, leading to a bigger efficiency of the process [67].

Chemical looping reforming is another technology aimed to create syngas, starting from hydrocarbons (methane mostly) through partial oxidation or steam reforming reactions.

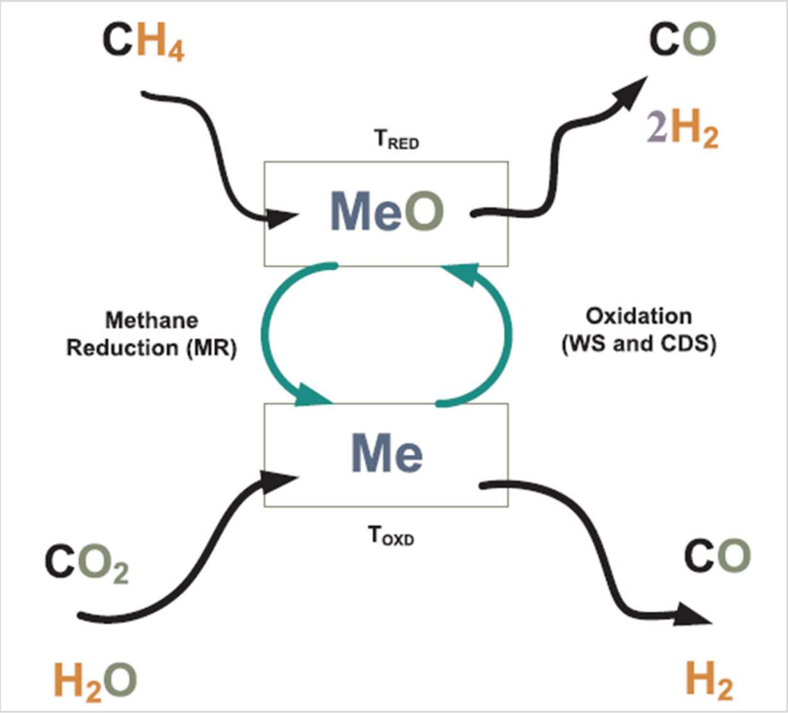

Figure 2.14: *Principle of chemical looping reforming* [56].

CLR follows the same principles of the chemical looping combustion but, instead of having as final goal the heat production, this time the process is aimed to generate syngas. Being methane a reducing agent, in CLR processes the reduction temperature required is lower and so the temperature swing between the reduction and oxidation reactors is lower [68]. In the first step methane is converted into syngas at temperature between 800 -1500°C, according to R*eaction 2.4*. After the reduction step, the oxygen carrier is re-oxidated using carbon dioxide and/or steam generating respectively CO or H_2 (*Reactions 2.5, 2.6*).

$$MeO_x + \delta CH_4 \rightarrow MeO_{x-\delta} + \delta(CO + 2H_2) \tag{2.4}$$

$$MeO_{x-\delta} + \delta CO_2 \rightarrow MeO_x + \delta CO \tag{2.5}$$

$$MeO_{x-\delta} + \delta H_2O \rightarrow MeO_x + \delta H_2 \tag{2.6}$$

If, in addition to the partial oxidation of the fuel, also steam reforming or dry reforming is wanted, H_2O and CO_2 can be added in the fuel reactor [69]. So, while at the exit of the reactor there would be only CO_2 and water for the CLC, in this case there is a mixture of H_2, CO, CO_2 and H_2O, as well some unreformed fuel: for instance, it can happen that at lower temperatures full conversion for the hydrocarbons can be hindered by pressure constraints. As example, in a simulation of chemical looping methane reforming performed in a laboratory reactor consisting of two interconnected fluidized beds ([70]), it was found that, at atmospheric pressure, the fuel reactor required 800°C in order to obtain up to 99% of CH_4 conversion; at a pressure of 15 bar, much higher temperature is needed (over 1000°C). It has to be noticed that the nature of solid oxygen carrier is an important parameter: in this study the oxygen carrier used is composed of 60% NiO and 40% $MgAl_2O_4$, composing the bed material, oxygen carrier and reformer catalyst. Other materials are considered for chemical looping, especially transition materials such as Cu, Fe, Mn and Co: each of them has some drawbacks in respect to the others; Fe is recognized having a low reactivity with methane and $Co\ and\ Mn$ follow the same behavior; Cu presents a low melting point and is likely to agglomerate [71]. Concerning the oxidizing reactor, air is another commonly used oxidant. The recovering of the oxygen carrier with air is an exothermic reaction and the heat production can be used both to compensate the need of heat during reaction or to produce electricity if in excess [70].

Another application for chemical looping technology regards its implementation in the oxygen production from air separation. Oxygen is at the second position between all the chemical production in the world (in volume), with a 30% of share in the global gas industrial market [72]. It is employed in a lot of different commercial applications, such as metallurgical industry, paper industry, glass production, chemical synthesis, petroleum refinery and health service [73]; it is also used in advanced power generation systems, such as integrated gasification combined cycle (IGCC), oxyfuel combustion, and solid oxide fuel cells (SOFC) [74]. Nowadays, oxygen is mainly produced using cryogenic air separation units (CASU), which are very energy intensive and are estimated to account for almost 3-4% of energy penalty in an oxy-fuel process [75]. In addition, in can be produced also from adsorption technology that have an energy cost similar to the previous ones because of the regeneration of the adsorption material, or with membrane separation, where a film of specific materials allows the selective separation of O_2 from air: in this case the energy required is lower, but membrane separation increase the complexity of the plant and has high costs of manufacture [76]. Chemical looping air separation (CLAS) is a new promising option for the production of oxygen. It has been demonstrated that the average specific power of a CLAS process is only the 26% of an advanced CASU [73]. In this technology two interconnected reactors are used: an oxygen carrier capture firstly the oxygen from air in the oxidation reactor, which is then released in the reduction reactor to a carrier gas, usually steam if pure O_2 is wanted, or a flue gas for create oxygen enriched gases.

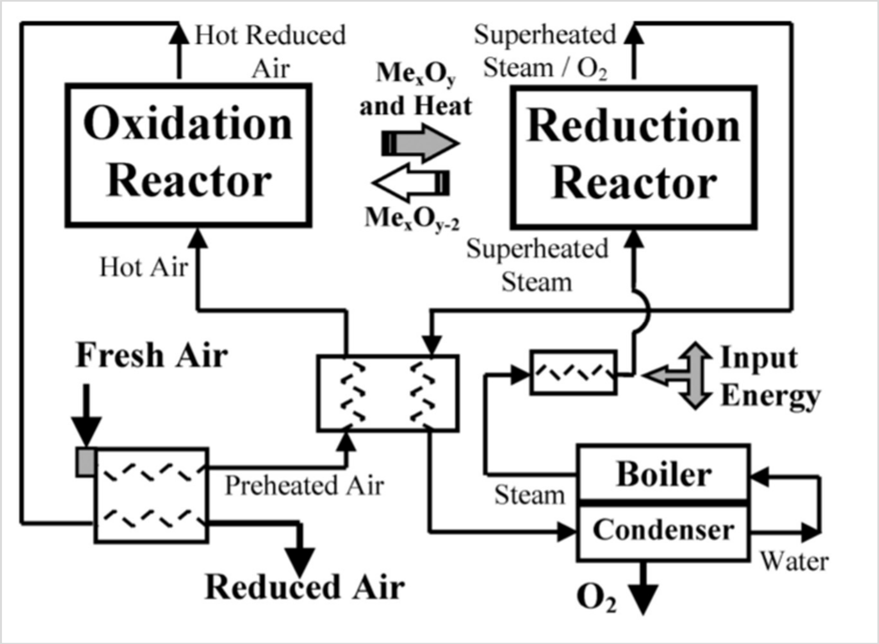

Figure 2.15: Schematic of the CLAS process [76].

To adopt this method on large-scale application, the key item regards the choice of the oxygen carrier and its capability of releasing oxygen under specific temperatures. Oxides of Ni, Cu, Co, Fe and Mn are typically considered for these cases: among all, copper oxide is the one with highest oxygen transport capacity and a good reactivity and stability [77]; SiO_2, TiO_2, ZrO_2 are all suitable binders for CuO, which increase its performances [78]. The reaction occurring in the two reactors are:

$$Oxidation: \quad Me_xO_{y-2}(s) + O_2(g) \rightarrow Me_xO_y(s) \tag{2.7}$$

$$Reduction: \quad Me_xO_y(s) \rightarrow Me_xO_{y-2}(s) + O_2(g) \tag{2.8}$$

The quite high efficiency of this process is due to its low energy demand: in fact, the theoretical heat needed is zero, since the heat produced in the oxidation reactor during the exothermic reaction is sufficient to support the endothermic reaction happening in the reduction reactor [72].

Chemical looping removal of ventilation air methane (VAM) in mining operations is a new concept invented by Moghtaderi and Doroodchi in 2014 [79]: by cycling metal oxide particles in a chemical looping process methane is removed from ventilation air. The contaminated air enters in the first reactor, while from the second one reduced air exits, together with water and carbon dioxide.

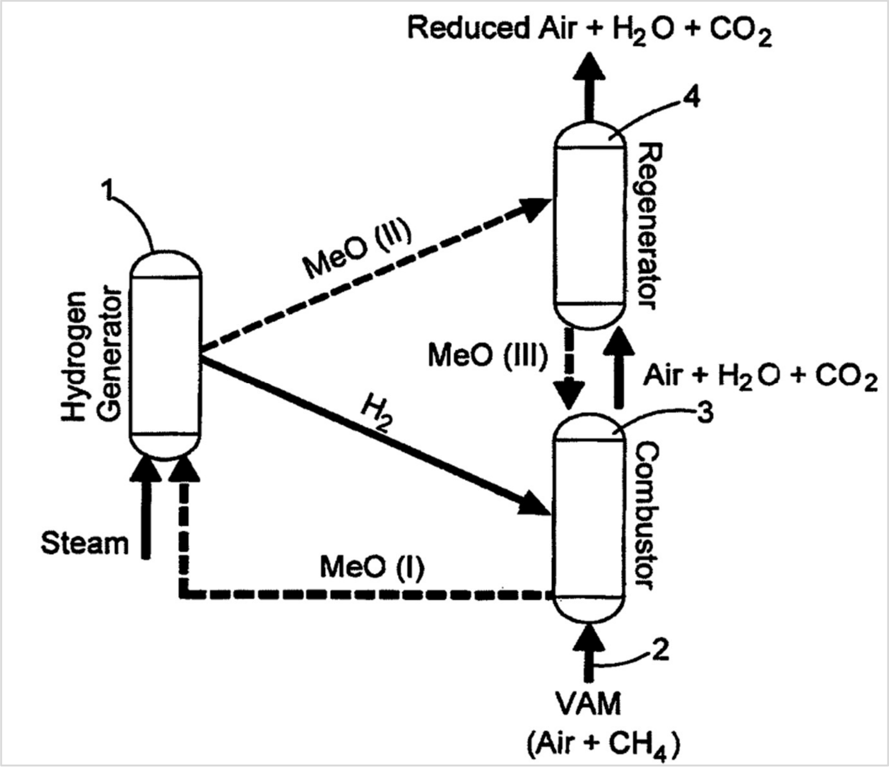

***Figure 2.16**: Schematic of the process* [79].

2.3.1. CO_2/H_2O dissociation by chemical looping

Despite all the possible applications of the chemical looping technology, actually one of the most interesting is its implementation in processes for the splitting of CO_2 and H_2O using clean energy, in order to produce green syngas ($CO+H_2$). Generally, the system consists in two interconnected reactors, namely the oxidation reactor and the reduction one. They contain metal oxide particles circulating in a closed circuit: during the reduction step, oxygen vacancies are created on the oxygen carrier lattice: the process occurs at high temperature and usually in presence of a reduction ambient (mixture of hydrogen and nitrogen has been used in this work); subsequently, during the oxidation phase, the metal oxide is re-oxidized by means of steam or CO_2, causing their splitting into H_2 and CO respectively. In Figure 2.17 a schematic of the process is showed.

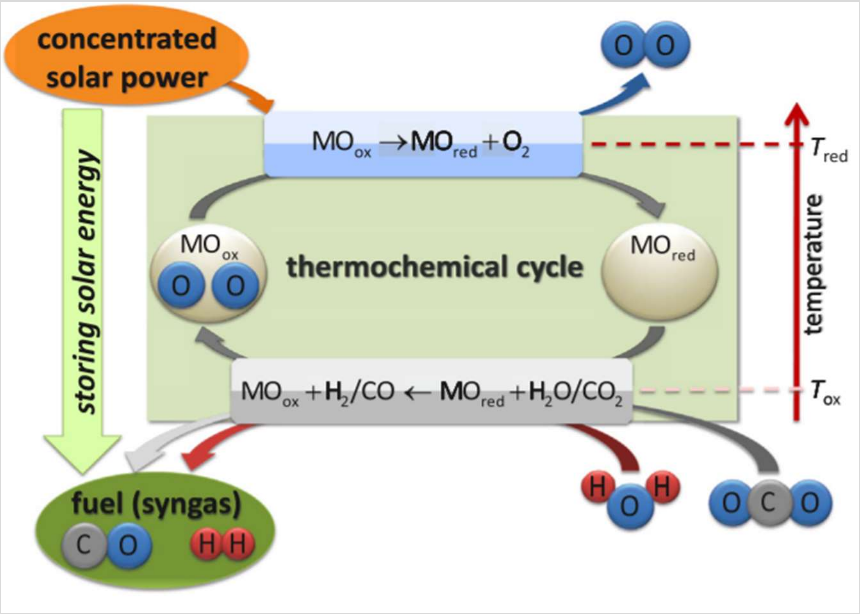

Figure 2.17*: Schematic of two-step thermochemical cycle* [42].

While the oxidation of the oxygen carrier is typically an exothermic reaction and can occur at lower temperatures, high temperature is required for the reduction: in this case heat is provided by means of concentrated solar energy. The exact temperature of the process depends mainly on the type of oxygen carrier that has been chosen, as well to other thermodynamic parameters of the mixtures. The ability of creating oxygen vacancies is also crucial in the choice of the material and usually its linked to its structure [80]. As general rule we can state that the reduction phase is certainly favorite at high temperature and low partial pressure of the oxygen, while the opposite conditions are the most suitable for the oxidation step: this would lead to a significant swing of pressure and temperature between the two reactors. In reality, particular operation conditions are chosen in order to make the process easier: by using a reducing fuel as hydrogen (or methane, CLR) in the reduction step, temperature can be kept lower and so match the one of the other reactors, as well as allowing an environmental pressure in the reactor. In the following, reaction occurring for each case are reported. In particular: thermal reduction (*Reaction 2.9*), reduction enhanced by H_2 as reducing agent (*Reaction 2.10*), oxidation step with water splitting (*Reaction 2.11*) and with carbon dioxide splitting (*Reaction 2.12*).

$$MeO_x \rightarrow MeO_{x-\delta} + \frac{1}{2}O_2 \qquad (2.9)$$

$$MeO_x + H_2 \rightarrow MeO_{x-\delta} + \delta H_2O + (1-\delta)H_2 \qquad (2.10)$$

$$MeO_{x-\delta} + \delta H_2O \rightarrow MeO_x + \delta H_2 \qquad (2.11)$$

$$MeO_{x-\delta} + \delta CO_2 \rightarrow MeO_x + \delta CO \qquad (2.12)$$

Concerning the reactor, it must be designed accurately to limit optical and energetic losses during all the process [81]. Usually, in chemical looping technology, conventional forms of concentrated solar power generation systems are used, such as line focus, parabolic though, heliostat fields and parabolic dish concentrators: the choice of one above the others depends mainly on the type of reactor and on the temperature level that we want to reach. Since a temperature higher than 1000°C is usually employed for thermal reduction of the metal oxide, heliostat field or central tower systems and parabolic dish technologies are the preferred solutions [40]. There are more types of reactors for chemical looping process and their choice is based on heat transfer mechanism from the CSP system to the reactor; generally, solar reactors are classified in Direct Process and Indirect Process [82].

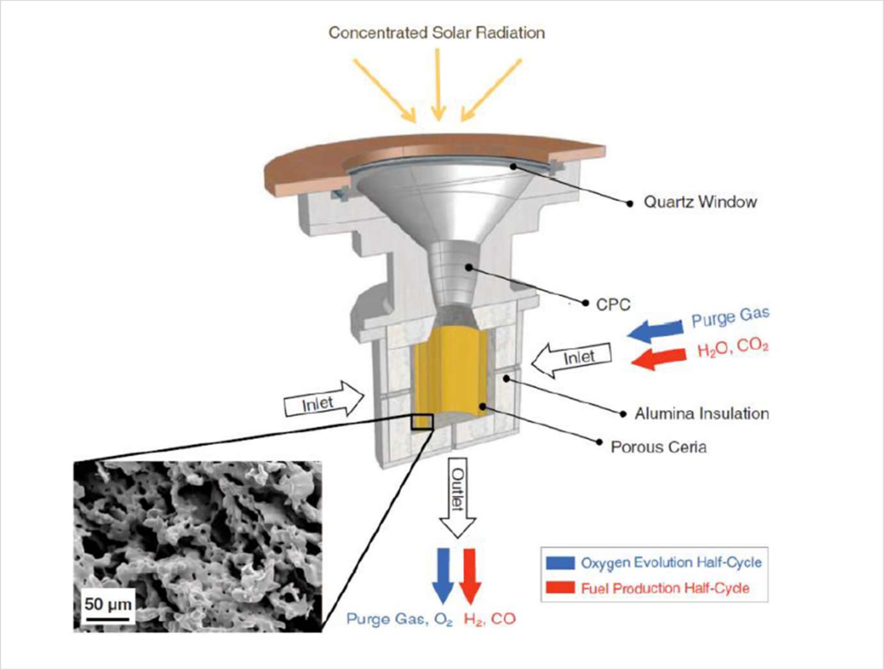

Figure 2.18*: Schematic of a structured process reactor* [83].

The first ones are solutions where reactor and receiver form a single unit (Figure 2.18), thus meaning a direct absorbing of the heat on the oxygen carrier, while indirect processes use an additional thermal fluid exchanging heat with the receiver. The choice of the type of the reactor depends again on the chosen oxygen carrier and particularly on the behavior it presents during oxidation and reduction reactions, in terms of structural change. A more detailed study of types of oxygen carriers and the development during the process are explained in the next chapter.

2.4 Materials for Chemical Looping

A lot of redox materials for the splitting of CO_2/H_2O have been investigated in literature and the research of the most suitable materials for the thermochemical cycles is still open. Different materials have different behaviors and the choice of one over the other is performed analyzing their drawback and advantages and how they fit in each application: the perfect oxygen carrier has redox activity at a temperature lower and far from its melting point, is able to perform and withstand multiple cycles without degeneration in both chemical and physical properties, should present a reproducible kinetics at high temperature and have high oxygen transport capacity: this is an important parameter, because the higher is the number of oxygen vacancies the material is able to form, the higher will be the fuel conversion and the circulation rate [84] . There are also other properties of the material to take in account depending on the technology used to perform the chemical loop: as example, if the process is carried out in a fluidized bed reactor, particles of the oxygen carrier should have a mechanical strength high enough to avoid attrition [85]. Generally, the most used materials are metal oxides, which are able to exhibit more oxidation states, allowing the releasing of oxygen during the reduction phase and the splitting of CO/H_2O in oxidation. They are divided in two different classes: “Volatile” oxygen carriers, which exhibit a physical transition to gas when reduced, and “Non-Volatile” oxygen carriers, which stay in solid phase during each step.

2.4.1 Volatile Oxygen Carriers

Volatile materials undergo to solid-to-gas phase change during the reduction step: this happens when the reduction temperature is higher than the vaporization temperature. This kind of behavior has some benefit, since the change of the physical structure is accompanied by large changes in entropy, which can be considered favorable for the thermodynamic of the process [86]. However, it implies also different issues at technical level, since require a fast cooling right after the reduction, in order to avoid the recombination of oxygen released and oxygen vacancies on the metal oxide [87]. These materials present a high endothermicity in reduction, needing higher temperature to reduce in comparison to the non-volatile ones; furthermore, at this extreme condition the recombination is favored [42]. The most common volatile metal redox pairs are $ZnO/Zn, GeO_2/GeO, CdO/Cd$ and SnO_2/SnO [88].

ZnO/Zn cycles are one of the most famous application of this type of material. Thermal dissociation of zinc oxide is highly endothermic (the ΔG of the reaction becomes null at 2235 K), while the oxidation of zinc is an exothermic reaction, becoming favorable from a thermodynamic point of view below 1400K. Zinc oxide was firstly employed for water splitting and later for the CO_2 splitting. ZnO presents a decomposition temperature of 2300K and a vaporization temperature of 1180 K [42]. The reaction occurring are listed in the following: thermal reduction (*Reaction 2.12*), oxidation with water (*Reaction 2.13*) and oxidation with carbon dioxide (*Reaction 2.14*).

$$ZnO \rightarrow Zn + \frac{1}{2} O_2 \tag{2.13}$$

$$Zn + H_2O \rightarrow ZnO + H_2 \tag{2.14}$$

$$Zn + CO_2 \rightarrow ZnO + CO \tag{2.15}$$

The different steps of the chemical looping process are presented in Figure 2.19. Thermochemical cycles based on zinc oxide have been considered and employed to obtain different products: hydrogen [89], [90] and syngas production [90], or for biomass gasification [91].

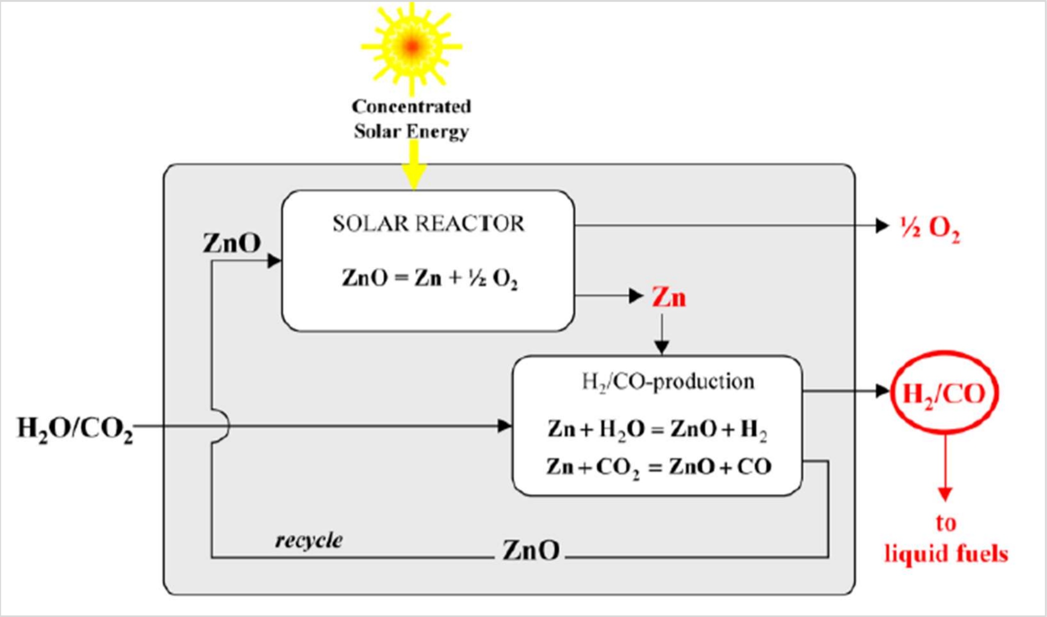

***Figure 2.19**: Zn/ZnO two step thermochemical cycle* [89].

Since ZnO thermal dissociation require a high quantity of heat, usually solar reactors for these applications (and the same for all the high temperature gas to solid reactions) are designed with the cavity receivers directly connected to the reactor, in order to expose directly the reacting particles to concentrated solar irradiation [56], [92]: in this case the limitations imposed by the indirect heat transfer and the losses associated are bypassed. A scheme of the one of the first reactor built for this application is showed in Figure 2.20.

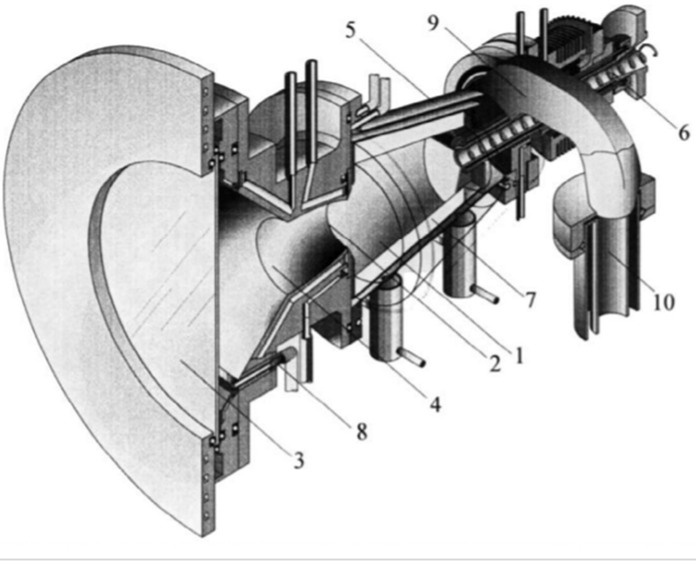

***Figure 2.20**: Schematic of ROCA reactor. Legend: 1=rotating cavity-receiver, 2=aperture, 3=quartz window, 4=CPC, 5=outside conical shell, 6=reactant's feeder, 7=ZnO layer, 8=purge gas inlet, 9=product's outlet port, 10=quench device* [90].

Germanium oxide is another phase change material that has been studied for hydrogen production. The cycle in this case is a two reaction steps: firstly, GeO_2 is decomposed to GeO at approximately 1400-1800 °C, then the germanium is re-oxided and hydrogen is produced through hydrolysis at temperature below 700°C [93]; During XRD analysis of the sample, the presence of Ge and GeO_2 phases were found, probably due to a disproportion of GeO in 0.5 Ge and 0.5 GeO_2 during quenching. The main advantage of germanium oxide cycles relies in the fact that the reduction temperature required are lower in comparison to zinc oxide or to tin oxide: SnO_2/SnO redox pair requires a reduction temperature of 1900 K, while the oxidation is at 900 K [94]. Another promising candidate for this class of material CdO/Cd cycle, which has recently been studied at University of Nevada [95]; this oxide requires a reduction temperature between 1150-1450 °C, which is lower in comparison to the others: unfortunately, its feasibility under real conditions was not yet demonstrated and so its strategical advantage remain actually a theory [42]. Since the deployment of volatile material is limited by the recombination issue, at the moment the research attention is shifted through other classes of materials.

2.4.2 Non-volatile materials

Despite the theoretical advantages of volatile materials, in chemical looping process metal oxides that remain in the solid state are a preferred solution. Oxides of $Ni, Fe, Cu, Mn\ and\ Co$ are all commonly considered materials to serve as oxygen carriers. Each of them has some disadvantages that have to be taken into account and can be diversified based on the type of oxide in which the metal is: in Figure 2.21 (a,b,c) the difference in term of behavior of a material in different state of oxidation is more evident. In general, the most visible drawbacks that can be observed are the low reactivity and low transport capacity of oxygen for $Fe\ and\ Mn$, the high cost and danger for health of Co and Ni and the low temperature of melting and thus the tendency to agglomerate of Cu [96].

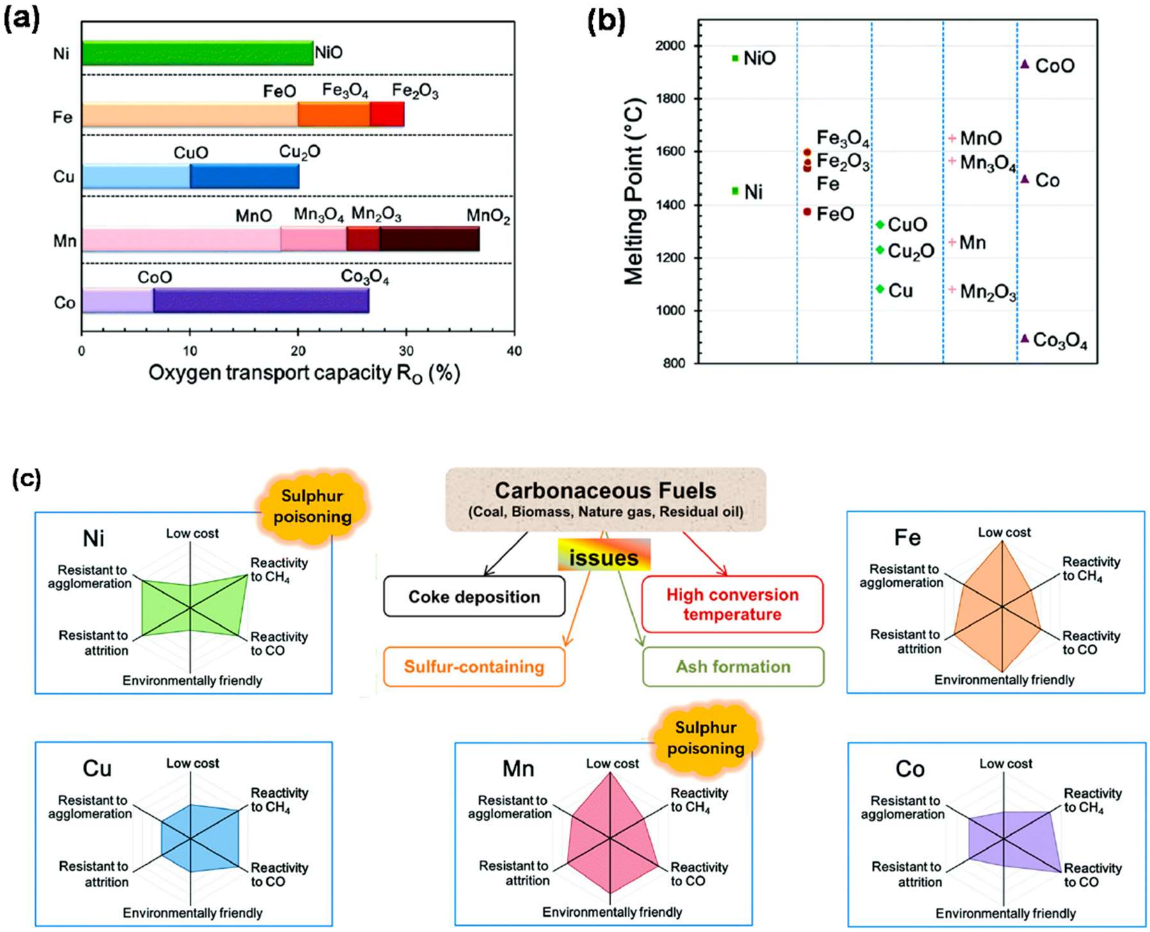

Figure 2.21*: Comparison between the key information for Ni, Cu, Mn, Co, Fe based material for chemical looping applications* [96].

One of the most important information understandable from the previous figure is that a lot of different factors should be considered when choosing a material for CL applications; first of all, the oxygen carrier should be selected based on the feedstock. If we consider the total cost of preparation of the material, including the cost of raw material, the promoters and the final preparation, Mn based carriers are the less expensive, followed in order by Fe, Cu, Ni and finally Co, which has the higher cost [71]. Despite that and environmental problems, Co based materials owe high reactivity and oxygen transport capacity. The highest oxidation state of Cobalt (Co_3O_4) is not stable at high temperature suitable for the chemical looping process and so the redox pair used is commonly Co/CoO [97]. The main problem of this oxidation state is its tendency to form unreactive phase with common promoter material used, such as MgO, alumina and titanium oxide: these unreactive phases ($Mg_{0.4}Co_{0.6}O, CoAl_2O_4 and\ CoTiO_3$, respectively) have been found in different studies [98], [99] and cause a fast deactivation of the oxygen carriers during the cycles. More advanced promoters have been considered in literature to overcome these issues: one of this, yttria-stabilized zirconia (YSZ) shows good reactivity and resistance to carbon formation [99].

Cu based carriers present a flexible redox behavior with high oxygen transfer capacity and high reactivity, as well as a low toxicity and low cost [97]. Copper reduced form can be both Cu and Cu_2O, while the oxidation state is CuO. However, their performances result affected by sulfur poisoning and weak mechanical strength, leading to attrition problem; in addition, the low melting point of Cu cause problem of agglomeration and thus requires an operation temperature under 800°C [85], [100] and a stabilization through inert promoters: some of the most considered are $Al_2O_3, ZrO_2, TiO_2\ and\ SiO_2$ [101].

Manganese carriers present various oxidation states, which includes $MnO_2, MN_2O_3, Mn_3O_4\ and\ MnO$: however, not all of these states are stable at high temperature and Mn3O4 is the only one that can exist at temperature bigger than 800 °C and so the redox pair for Mn based material is MnO/Mn_3O_4 [97]; this phase shows a low oxygen transfer capacity and low reactivity, especially toward CH_4 in CLR applications. Mn materials are still considered for chemical looping because of their low cost and low toxicity but presents many drawbacks: they suffer from deactivation as consequence of sulfur poisoning and tend to form unreactive phases with typical promoter like $SiO_2, Al_2O_3, TiO_2, ZrO_2\ and\ MgAl_2O_4$ [101], [102]. More advanced research has found high reactivity behavior, structural stability, and resistance to agglomeration for Mn based carriers when doped with MgO, CaO, Y_2O_3, La_2O_3 and CeO_2 stabilized by zirconia, keeping this type of material as option for chemical looping processes [103], [104].

Nickel is a well-known catalyst for reforming activity due to its high reactivity with methane and other light hydrocarbons: it has been assessed that an almost complete conversion of CH_4 can be observed using Ni based materials during a chemical looping reforming cycle [105]. However, this material presents some drawbacks: along with the high cost and toxicity, the loss of catalytic performance due to particle sintering and the repetition of cycles, as well as the tendency to deactivate for sulfur poisoning, make this material necessitate for promoters and others supports [106]. For Ni based oxygen carriers, there is a large number of possible promoters that have been object of different research: oxides such as Al_2O_3, SiO_2, TiO_2, ZrO_2 and stabilized ZrO_2 are considered, along with other type of structured materials (spinels) like $NiAl_2O_4$ [107], $MgAl_2O_4$ [108] and $CaAl_2O_4$ [109]. The couple with highest reactivity has found to be NiO/Al_2O_3, as well as an excellent thermal stability and resistance to formation of carbon during the cycle [110]; the main problem of this promoter is due to the formation of inactive spinel phase $NiAl_2O_4$ which implies a loss of initial reactivity. A possible solution is the addition of oxides like MgO and CaO to the oxygen carrier in order to form $MgAl_2O_4$ or $CaAl_2O_4$ spinel, which suppress the $NiAl_2O_4$ formation and so keep the reactivity of nickel unaltered [108]. Other promoters don't show the same performance of Al_2O_3: TiO_2 causes a stable phase of NiTiO3 and present a slow or almost null reaction rate [111], SiO_2 gives to the carrier a low reactivity and deactivation throughout the cycles [102], while for NiO/ZrO_2 or $NiO/stabilized\ ZrO_2$ oxygen carriers the high reactivity is hinted by weak mechanical characteristics [112], [113]. Another interesting solution consists in the use of other reducible oxide as support material for Ni based oxygen carriers. Particularly CeO_2 has been found to increase the oxygen transfer thanks to a new $Ni - CeO_2$ interface [114]. Bahvsar Et al. also investigated La_2O_3 as reducible oxides for nickel support: results indicate that ceria is more efficient during oxidation and also reduction kinetics results accelerated; however, both present a thermal stability and higher performances if compared to conventional and not reducible oxide supports (e.g., Al_2O_3, SiO_2).

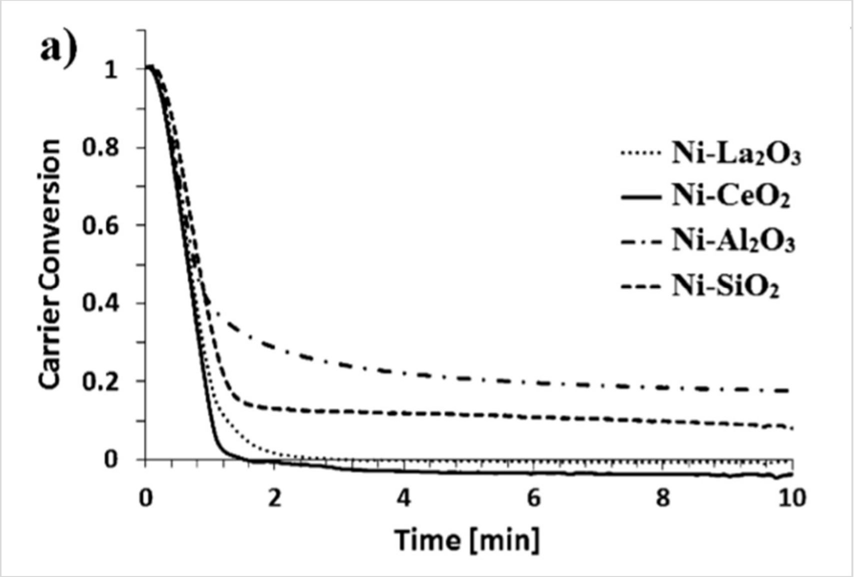

Figure 2.22: *Comparison of carrier conversion as a function of time for various Ni-based carriers during reduction* [114].

CeO_2/$CeO_{2-\delta}$ is actually investigated as one of the most important CL materials thanks to its high ionic diffusivity, oxygen storage capacity and fast kinetics. The main disadvantage of this material is the high temperature requested for the reduction, above 1500 °C: this level of temperature brings some resistance problems for the reactor materials, as well as a possible sublimation of ceria, which decrease the reduction capability of the oxygen carrier. CeO_2 is structurally stable and allows competitive productivity for what concern hydrogen production [115]. As increasing the temperature, the efficiency, the extent of reduction and CH_4 conversion increase too, leading to the stop the carbon formation at maximum temperature of 1300 °C [116]. CeO_2 presents a fluorite structure and its surface (110 type) undergo reduction forming two kind of oxygen vacancy, an in-plane or split [117].

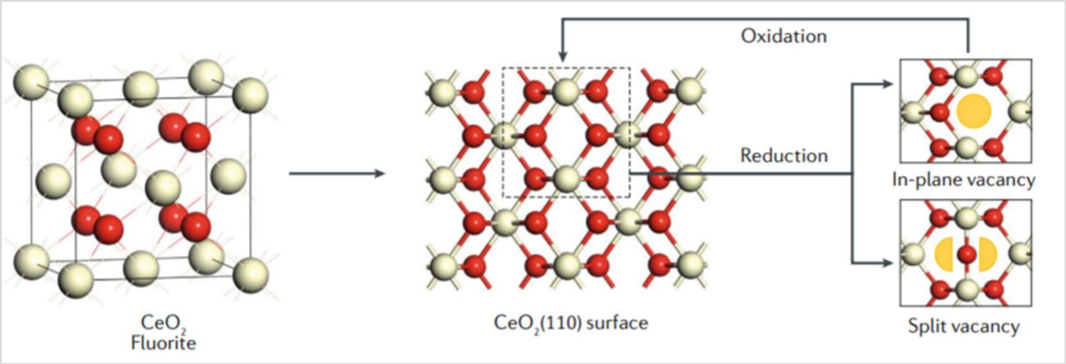

Figure 2.23*: Crystal structures of ceria oxygen carrier* [117].

According to literature, isothermal redox cycles have been discovered more efficient in terms of time and energy conversion [118]: this condition can be achieved by using a reducing agent, methane as example. In this way the reduction step can be performed at lower temperature in comparison to thermal dissociation only and thus bringing the temperature to the one of the oxidizing step. This is a condition more suitable and near to real application and has the advantage of producing additional hydrogen or syngas thanks to the ceria reduction with methane [119]. In the following reactions, thermal reduction of CeO_2 (*Reaction 2.15*), reduction using methane (*Reaction 2.16*) and the two types of oxidations (*Reactions 2.17, 2.16*) are reported.

$$\mathbf{CeO_{2(s)}} \rightarrow \mathbf{CeO_{2-\delta(s)}} + \boldsymbol{\delta 2O_{2(g)}} \tag{2.16}$$

$$\mathbf{CeO_{2(s)}} + \delta CH_4 \rightarrow \mathbf{CeO_{2-\delta(s)}} + 2\boldsymbol{\delta H_{2(g)}} + \boldsymbol{\delta CO_{(g)}} \tag{2.17}$$

$$\mathbf{CeO_{2-\delta(s)}} + \boldsymbol{\delta H_2O_{(g)}} \rightarrow \mathbf{CeO_{2(s)}} + \boldsymbol{\delta H_{2(g)}} \tag{2.18}$$

$$\mathbf{CeO_{2-\delta(s)}} + \boldsymbol{\delta CO_{2(g)}} \rightarrow \mathbf{CeO_{2(s)}} + \boldsymbol{\delta CO_{(g)}} \tag{2.19}$$

Despite the excellent oxygen ion mobility and redox kinetics, ceria-based cycles present thermal stability loss and low solar to fuel efficiency and so its property can be improved by doping with other materials: generally, while increasing the dopant concentration, the process performance increases [42]. A possible solution consists into doping the ceria with zirconium [42], [120], leading to an increase of the splitting properties of CeO_2 and of the oxygen diffusion capability.

Fe- based materials are well known oxygen carriers in the chemical looping application; their spread into this field is due to the low price, high mechanical strength and a secure and environmentally nature [97]. Additionally, they can be used in all type of processes, including ones with carbonaceous and sulfur-containing fuels since don’t have the tendency to deposit carbon or sulphur [121]. Iron oxides are the most employed materials for CO_2 splitting, since it has been found that contain almost 0.7 mol CO_2/mol Fe over a range of temperature up to 1800 °C, which represents one the highest oxygen storage capacity from CO_2 [122]. However, Fe-based materials can’t be adopted for all the application: in fact, they show a low reactivity to gaseous fuel and tend to agglomerate because of the formation of magnetite [123]. Reduction and oxidation reactions are listed.

$$\mathbf{Fe_3O_{4(s)} \rightarrow 3FeO_{(s)} + 12O_{2(g)}} \tag{2.20}$$

$$\mathbf{3FeO_{(s)} + H_2O_{(g)} \rightarrow Fe_3O_{4(s)} + H_{2(g)}} \tag{2.21}$$

$$\mathbf{3FeO_{(s)} + CO_{2(g)} \rightarrow Fe_3O_{4(s)} + CO_{(g)}} \tag{2.22}$$

Furthermore, pure Fe oxides are susceptible to sintering during the cycle at high temperature, causing a degradation of the material and the deactivation: thermal reduction occurs for temperature higher than 1300°C and at this level sintering phenomena appears [124]. Sintering resistance ability can be increased by adding proper materials: as for others oxygen carrier, also in this case appropriate promoters can be used for increasing properties. A lot of studies with different promoters are present in literature: Al_2O_3 [125], MgO [126], TiO_2 [127], SiO_2 [128], $MgAl_2O_4$[129], [130], CaO [131], ZrO_2 [132] and CeO_2 [133]–[135]. The bigger drawback while using these promoters is the formation of new phases like $AlFe_2O_4$, $MgFe_2O_4$, $FeTi3$, and Fe_2SiO_4, $Ca_2Fe_2O_5$ and $CeFeO_3$, which still prevent the iron oxide from sintering, but at the same time cause a decrease of the carrier reactivity, since these metal- ferrites need make more difficult the regeneration of the active iron oxide: in this way, the overall oxygen storage capacity decreases [136]. Among them, however, ceria is considered as the most interesting option, since its role doesn’t limit to just a physical promoter, but it is also a chemical active promoter with high reactivity towards $CH_4$and good re-oxidation capacity towards carbon dioxide and water [137]. In particular, the addition of ceria in Fe-based materials increase the reducibility of Fe_2O_3 thanks to the interaction $CeO_2 - Fe_2O_3$: if $Ce4+$ ions are replaced by $Fe3+$ cations with lower valence, the creation of active sites (oxygen vacancies) occurs; as final effect, we can state that the cerium ions help the oxygen storage and release from its bulk fluorite lattice [97].

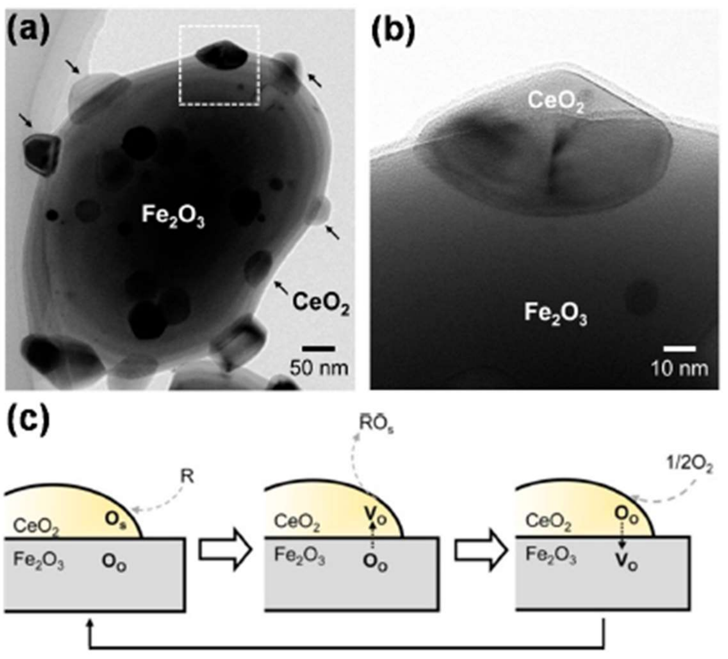

Figure 2.24*: CeO_2-grafted Fe_2O_3 oxygen carrier. TEM image (a) and an enlargement of the square region (b); Schematic representation of its oxygen release and storage mechanism (c). VO: oxygen vacancy, OO: lattice oxygen, Os: surface oxygen [97].*

2.4.3 Perovskite oxygen carrier

Perovskites are a particular class of materials characterized by a ABO_3 structure and their employment as oxygen carrier in chemical looping applications is appreciated thanks to their thermal stability, enhanced redox properties and high oxygen mobility [97]. Actually, various perovskite materials are being studied for chemical looping and they can be very different from each other depending on which material occupies the site A and B: indeed, the great interest towards these materials rely in the fact that they can be composed by a wide range of composition of elements with different characteristics, in order to adjust the properties of the oxygen carrier in relation to the particular application; the importance of these materials derives from the property that the structure presents. Perovskites present various and usually very different patterns of cations, compensation of vacancy and transitions caused by the lattice distortion due to different materials. Typically, A site is occupied by large alkaline earth or by a rare earth element and is responsible for the thermal resistance, while B is a cation of a small transition metal and is the one that determines the final reactivity of the carrier [86]. The choice of A and B elements is crucial for the performance of the perovskite carrier, not only because of the properties they bring to the structure, but also because their interaction can affect the structural stability and the reactivity, as well as the selectivity towards different type of fuels [138]. A is larger than B and the elements can be positioned in three possible combinations, as shown in Figure 2.25; A and B sites can be occupied also by more elements and thus forming doped or double perovskites [139].

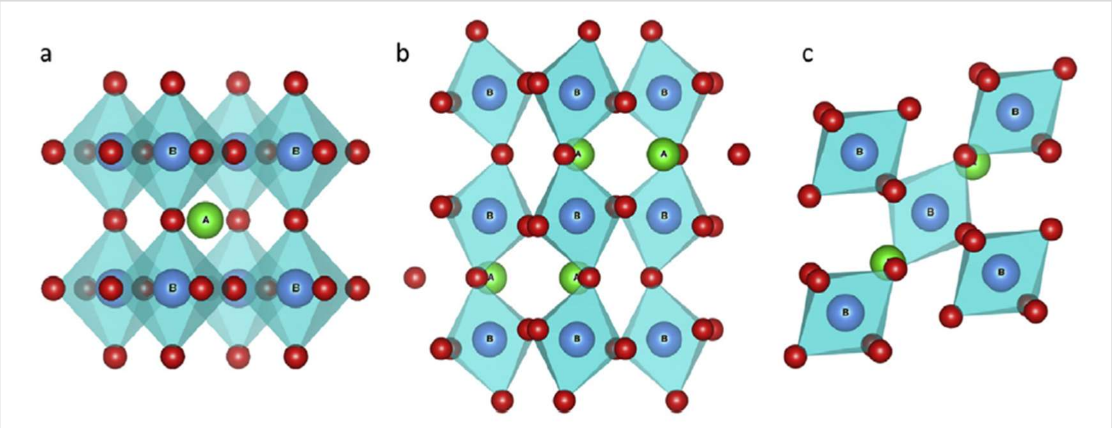

***Figure 2.25**: Schematic of perovskite structures with ABO_3 formula: (a) cubic, (b) orthorombic, and (c) rhombohedral. Atoms: A (green), B (blue) and O (red)* [139].

Perovskites show a non-stoichiometric reduction and the reactions happening are:

$$\mathbf{ABO_3 \rightarrow ABO_{3-\delta} + \delta 2O_{2(g)}} \tag{2.23}$$

$$\mathbf{ABO_{3-\delta} + \delta H_2O_{(g)} \rightarrow ABO_3 + \delta H_{2(g)}} \tag{2.24}$$

$$\mathbf{ABO_{3-\delta} + \delta CO_{2(g)} \rightarrow ABO_3 + \delta CO_{(g)}} \tag{2.25}$$

Thanks to its enhanced properties for this application, $Fe3+$ is an obvious choice for the B-site cation and it has been subject of different research [140]–[143]. Different A site elements were considered in these studies. Dai et al. [140] used $La, Nd, and\ Eu$ as A material and discovered that the best performance for what concern stability and syngas production was showed by $LaFeO_3$. The possibility to perform a partial substation in A-site cation by a metal such Sr, which presents a lower oxidation state, was also investigated: in this way a variable oxygen non-stoichiometry is introduced in the structure, increasing the oxygen vacancy capacity; actually, $La_{1-x}Sr_xFeO_3$ are widely considered for CLR processes [142], [143]. Further, a partial substitution of B-site cations can be also performed with the aim of increasing the catalytic activity due to the valence changes and introduced non-stoichiometric microdefects [97]. $La_{1-x}Sr_xFeO_3$ was modified by adding transition material as $Ni, Co, Cu\ and\ Cr$ [142]; in this case the best combination between all the analyzed perovskite structures was found to be $La_{0.7}Sr_{0.3}Cr_{0.1}Fe_{0.9}O_3$, because the partial substitution of Fe by Cr has showed the highest syngas production, redox properties and almost zero carbon deposition. The use of magnesium is considered too, since the presence of $Mg2+$ in the B site can increase the thermal stability and reduce the sintering phenomena [144]: $La_{0.5}Sr_{0.5}Mn_{0.9}Mg_{0.1}O_3$ (LSMMg) results to be a good oxygen carrier with high fuel production. In an experimental study of chemical looping process [145], Lanthanum-Strontium-Manganates ($La_{1-x}Sr_xMnO_{3-z}$) has been tested and compared to performance of ceria during reduction at 1000°C: even if the oxygen released is higher than the metal oxide, at lower temperature perovskites don't show a complete re-oxidation from CO_2. $La_{1-x}Sr_xMn_yAl_{1-y}O_{3-z}$ on the other hand showed a good repeatability when reduced at 1400°C and re-oxidized with both water and carbon dioxide [146]. In the same work single-phase powders of $Sr_xLa_{1-x}Mn_yAl_{1-y}O_{3-z}$ (called SLMA1-3) were tested and compared to performance of CeO_2 for CO_2 and H_2O splitting at typically used condition for chemical looping applications. In figure 2.26, H_2 and CO production rates are showed for all four tested materials (SLMA1-3 and CeO_2) when reduced at 1350°C and oxidized at 1000°C: using these operation temperature, H_2 production rate results almost nine times higher than ceria one, while for CO is 6 times bigger.

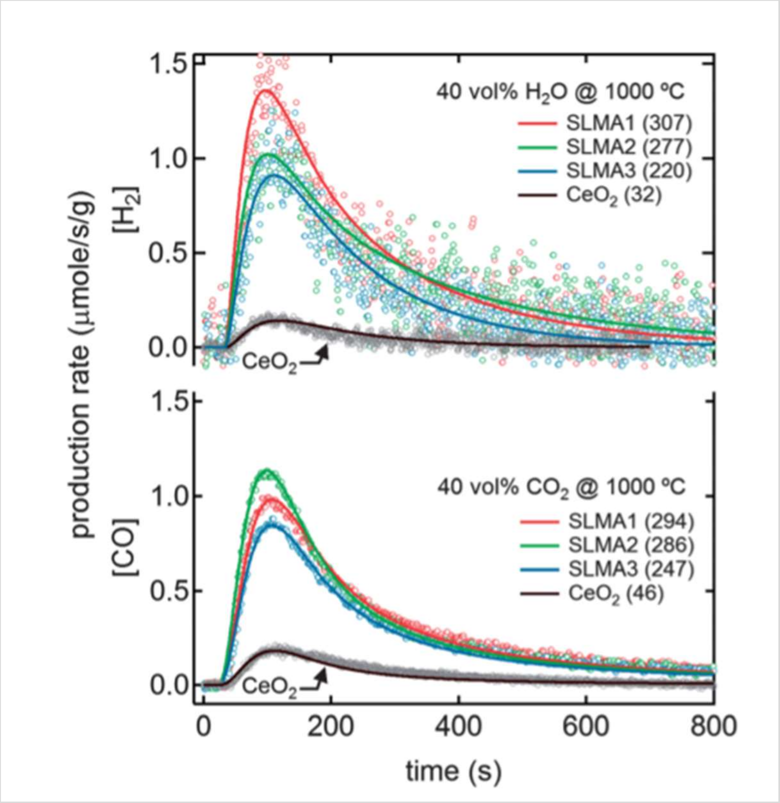

Figure 2.26: *H_2 and CO production rates (top and bottom respectively) as time function measured during oxidation in 40 vol% H_2O or CO_2 at 1000 °C. after being thermally reduced at 1350 °C in He. The total amount of H_2 or CO produced in micro moles per g material is shown in parentheses* [146].

Cooper et al., also studied Ca incorporation into $La_{1-x}Sr_xMn_yAl_{1-y}O_{3-z}$ perovskites [147]: among all the material analyzed in this study, $La_{0.6}Ca_{0.4}Mn_{3-z}$ and $La_{0.4}Ca_{0.4}Mn_{0.6}Al_{0.4}O_{3-z}$ achieved the highest productions of fuel. Qiongqiong et al. [148] developed a solar-driven chemical looping steam methane reforming process by using $La_{1-y}Ca_yNi_{0.9}Cu_{0.1}O_3$ perovskite as oxygen vector: they have found that the reactivity of the material improves while increasing the calcium substitution and so, between all the various synthetized perovskite's structure, $La_{0.1}Ca_{0.9}Ni_{0.9}Cu_{0.1}O_3$ has the highest reactivity, regenerability and the strongest resistance to carbon deposition. In the following figure (Figure 2.27) the results of the TPR executed for all the materials considered: it can be seen that by increasing the amount of calcium, curves peak is more visible for both surface absorption (happening at lower temperature) and the lattice absorption, as well more calcium brings to a temperature reducing for the starting of the phenomena.

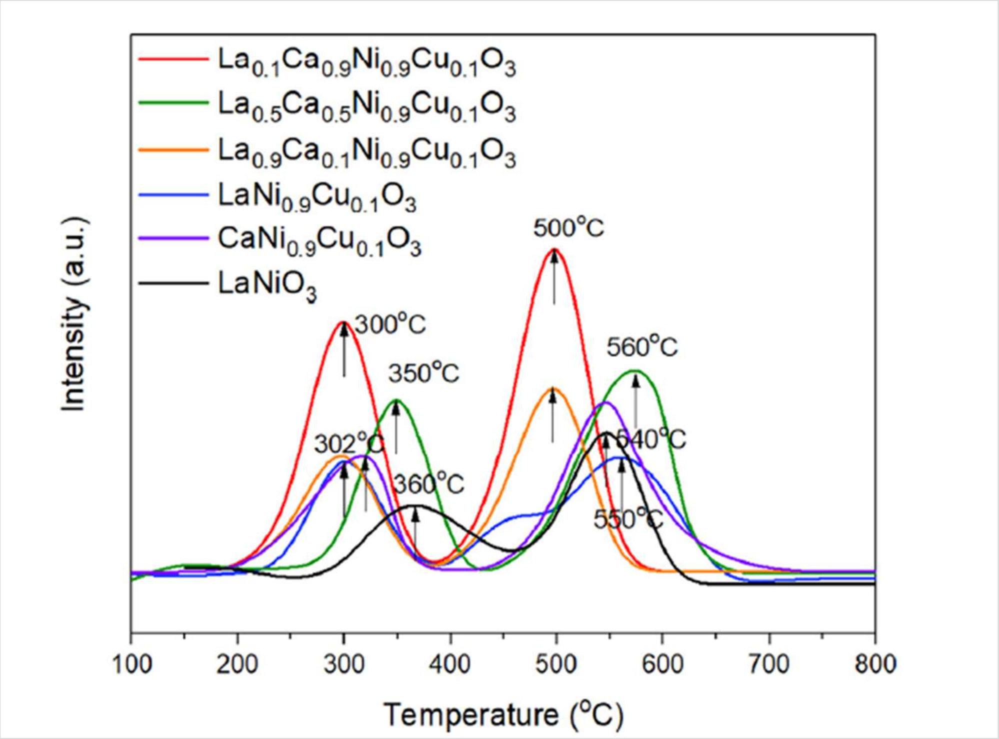

***Figure 2.27**: TPR results of hydrogen for different perovskites* [148].

Ba-based perovskites have been investigated for H_2O splitting by Barcellos et al. [149], in which an optimal doped perovskite was obtained by mixing $BaMnO_{3-z}$ and $BaCeO_{3-z}$, reaching a high level of non-stoichiometry and re oxidation conversion: the mixed material so obtained ($BaCe_{0.25}Mn_{0.75}O_{3-z}$) is indeed required, since $BaMnO_3$ alone results too difficult to re oxidize, even if easier to reduce, while the opposite happens for $BaCeO_{3-z}$. Another perovskite is the one synthesized by Dey at al. [150] by using yttrium in A-site cation: $Y_{0.5}Sr_{0.5}MnO_{3-z}$ (YSM) showed the highest distortion and size disorder and a very high level of conversion for the splitting of CO_2, reporting one the highest reaction rates, even if the reduction is performed at 1200°C and the oxidation at 900°C. $CaMnO_3$ has also been studied lately as promising perovskite material: new modified calcium manganese (CM) structure has been synthetized and their performance analyzed in a 2016 study [151]. In this structure a transformation in Ca_2MnO_4 can occur, leading to a possible decrease of the efficiency at high temperature: the solution proposed to make the structure more stable consists in the use of other transition material such as $Ti, Fe, Zr\ and\ Cu$ to dope the B site together with manganese.

In conclusion, several oxygen carriers have been reported for CO_2/H_2O splitting through chemical looping technology: literature is rich of studies for different type of perovskites and at the moment the main focus of the research rely precisely in finding new and alternative materials to reach a higher level of efficiency: both the presented technology for chemical looping and the listed material present some limitations that want to be overcome. The optimal material we are searching for will be able to perform properly at lower temperature, as example, leading to benefits regarding the structural stability of the OC, the sintering and agglomeration phenomena and also the component life of the reactor. Beside the aspect of temperature, also the properties of the oxygen carrier are taken into account: their ability to create O_2 vacancies and the susceptibility to acquire and release oxygen molecule are very important and the possibility to enhance them thanks to doping. The cost of the material is also important, especially in the future perspective to adopt them for a bigger industrial scale. At the moment, the state of art for chemical looping applications is ceria because of its high kinetics and redox properties; however, ceria requires operating temperature too high and thus moving the interest through more interesting material, such as perovskites precisely. This thesis work, which comes from a collaboration between the Polytechnic of Turin, Massachusetts Institute of Technology (MIT) and University of Udine, focuses on the study of a new perovskite material, namely $Sr_2FeNi_{0.4}Mo_{0.6}O_{6-\delta}$ (SFNM04), in order to analyze its performance and chemical behavior by changing operating parameters.

2.4.4 SFNM04 as oxygen carrier

$Sr_2FeNi_{0.4}Mo_{0.6}O_{6-\delta}$ (SFNM04) is a perovskite material studied by University od Udine for the "PRIN17 – Direct Biopower" project [152] and synthesized starting from $Sr_2Fe_{1.5}Mo_{0.5}O_{6-\delta}$: this material is a double perovskite, thus presenting a $A_2(BB')O_6$ structure where A is a alkaline metal and B' are transition materials, which in this case are iron and molybdenum. SFM double perovskites are already studied in literature to be employed as electrode material for solid oxide fuel cells [153], [154]: indeed, it has suitable properties for a reversible fuel cell, such as high electronic and ionic conductivity, stability at high temperatures, both in oxidant and reductant ambient. When nickel is added to SFM, $Ni2+$ cations enter in the lattice and are expected to substitute $Fe2+$ ones, leading to a prevalence of $Fe3+$ over $Fe2+$: this change brings to a higher electronic conductivity, both for the new ratio between *Fe (2)/Fe (3)* and also for the higher one of the nickel atoms.

Another fundamental phenomenon which characterizes this new material is exsolution: Fe and Ni tend to exsolve from the lattice in a reducing ambient, implying in this way a creation of a $Ni - Fe$ alloy on the surface; the main advantage brought from exsolution is that this alloy presents a bigger resistance to coke and sulfide poisoning than just metallic nickel and so the electro-catalytic performance of the perovskite are enhanced. The nanoparticles of nickel can be incorporated by using mainly two different procedures. The infiltration method is the most mature but presents some limitation for the high cost and doesn't ensure an optimal control on the new created morphology. On the other hand, nanoparticles growth in situ are characterized by a uniform distribution, they are faster and less expensive [155].

The synthesis of the sample is realized in this case using Self-Combustion Synthesis (SCS) with citric acid as complexing agent, followed by a calcination at 1110°C in order to obtain a pure cubic structure. X-ray diffraction (XRD) test was performed to characterized different phases of the perovskite, both for the starting material $Sr_2Fe_{1.5}Mo_{0.5}O_{6-\delta}$ (used as reference material) and for the new synthesized ones. From the results of the composition spectrum, it is possible to notice a limitation in nickel solubility in the double perovskite lattice in SFNM-05 sample: in this case indeed a NiO segregation happens on the surface, meaning that not all the nickel is entered in the structure. Since for SFNM-04 this phenomenon doesn't show, the solubility limit of Ni in the molybdate structure is found to be between 0.4 and 0.5 molar compared to the other metallic cations.

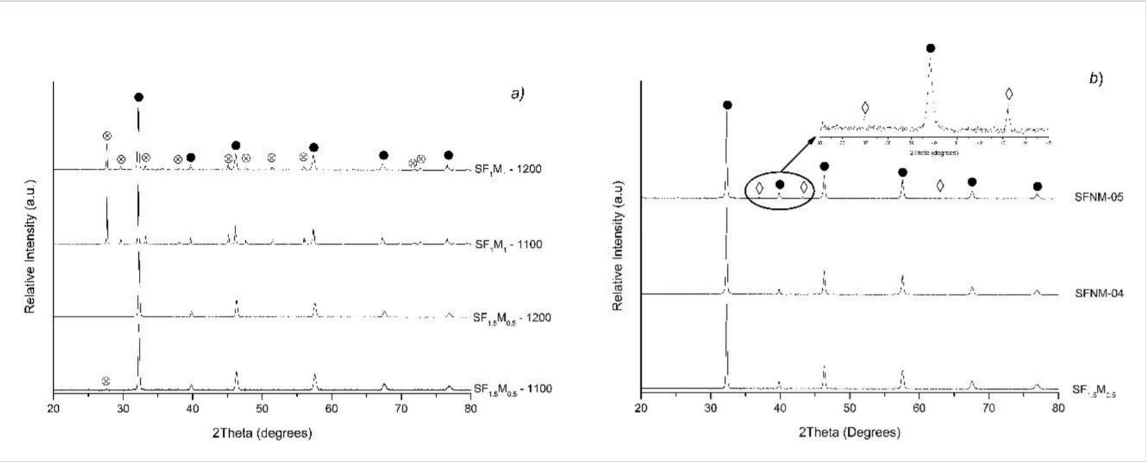

Figure 2.28: XRD pattern of a) Sr2Fe1.5Mo0.5O6-δ (SF1.5M0.5) and Sr2FeMoO6 (SF1M1) cubic phases at different calcination temperatures. (●) SFM, cubic; (Ⓧ) SrMoO4, tetragonal. b) SF1.5M0.5 (Sr2Fe1.5Mo0.5O6-δ at 1200 °C), SFNM-04 (Sr2FeNi0.4Mo0.6O6-δ) and SFNM-05 (Sr2FeNi0.5Mo0.5O6-δ) [152].

An X-ray photoemission spectroscopy (XPS) and an energy dispersive X-ray (EDX) analysis have been performed too on SFNM-04 and SFNM -05 samples, in order to verify the real chemical composition: the results showed a small surface segregation of Sr in the first one, while a significant amount of nickel on the surface of the second one, due to the overcome of the solubility limit.

Once the structural characterization of the sample has been done, a further functional study has been carried out. This was possible thanks to a temperature programmed reduction analysis (TPR), which helped to investigate the evolution and stability of the material during redox cycles. The chosen procedure for the study followed 5 steps: a first pre-treatment until 500°C (10°C/min) in air, an hour dwelling at this temperature, a TPR analysis up to 900°C using 4.5% of hydrogen (in N_2) with a volumetric flow of 35 ml/min and finally a cooling ramp until room temperature with nitrogen, followed by a final re-oxidation ramp as the beginning. The process has been repeated for four cycles, in order to check the repeatability too. It has to be noticed that the initial pre-treatment in air has been done to remove impurities and other species from the surface, as well to perform the oxidation of the sample after the reduction. The same approach in air will be used also for our test.

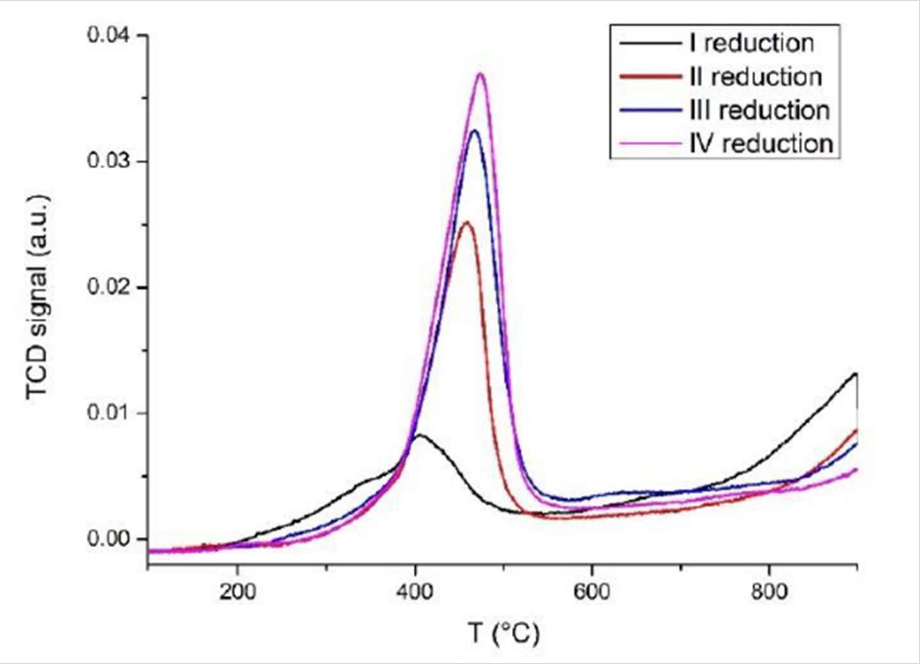

Figure 2.29: *TPR analysis of SFNM-04 in 4.5%* H_2/N_2 [152].

From the results we can see a difference between the first cycle and the others: after the first cycle the profile starts to show more stability and constancy and the same for the following ones. The explanation of that was found in the creation of a transition phase more stable in reduction during the first cycle, and it was confirmed thanks to XRD analysis: it is noted the present of a Ruddlesden-Popper (RP) phase, more precisely $Sr_3FeMoO_{6.5}$. This phase is not absolute but is present simultaneously in the structure with the double perovskite phase. Generally, RP phases are indicated as $A_{n+1}B_nX_{3n+1}$: indeed, more types of this structure exist and some of them are reported in the following figure (Figure 2.30).

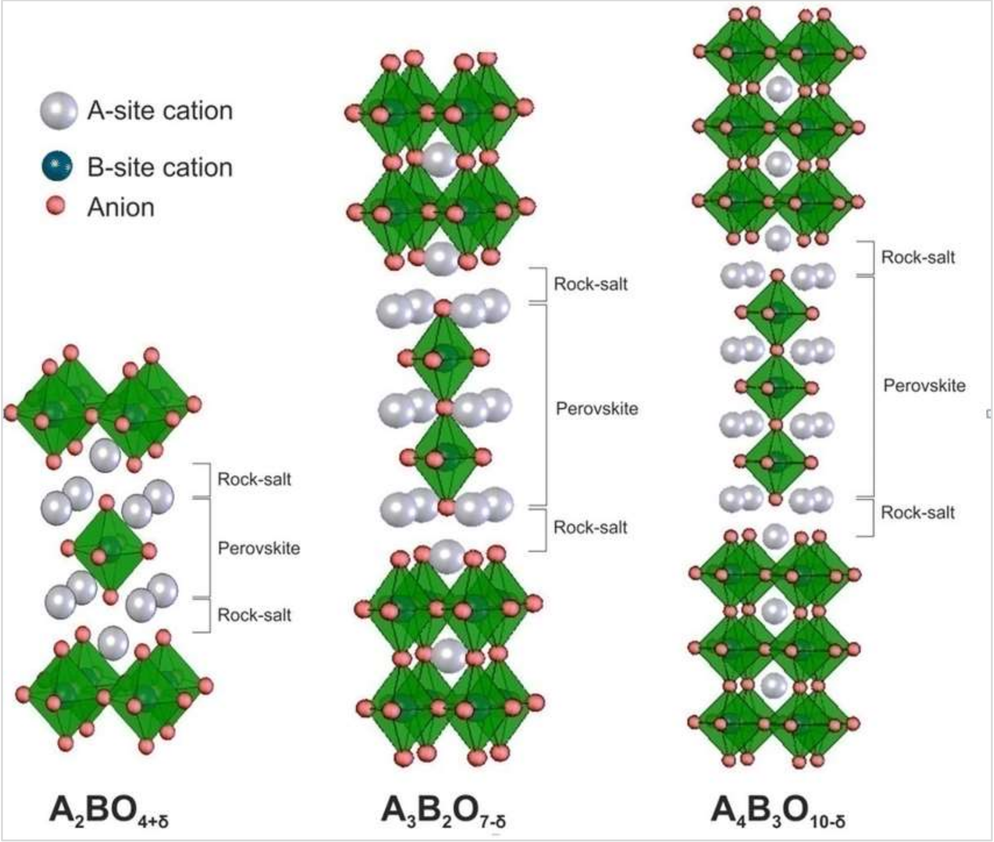

Figure 2.30: *RP perovskite structures represented by single or multiple perovskite layers between rock salt layers. From the left: n=1,2,3* [156].

It has to be noted that also formation of $FeNi_3$ is detected in the XRD analysis, as consequence of the occurring of ex solution phenomenon. Increasing the number of cycles, the RP phase shows a decrease in the signal entity from XRD, while the peak signal associated to $FeNi_3$ tends to increase. This behavior clearly indicates that the exsolution process doesn't show immediately, but it proceeds during the cycles, thus justifying the increment in hydrogen consumption with TPR evolution. This phenomenon is clearly shown in the magnification of Figure 2.31.

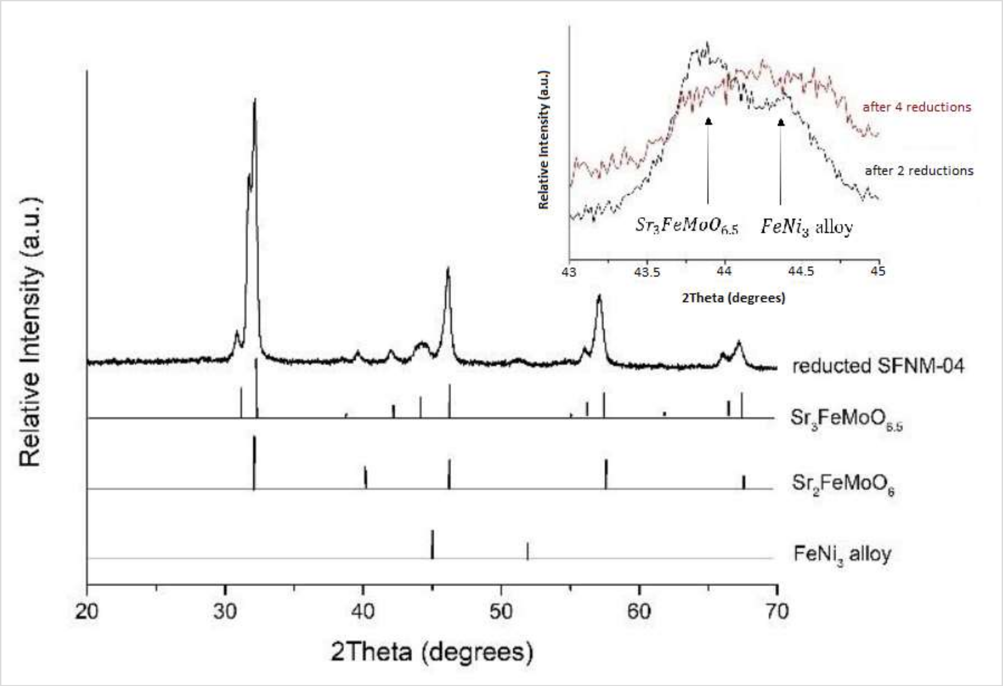

Figure 2.31: *XRD of SFNM-04 after 4 cycles. On the right: magnification in the range 43° and 45°, showing a comparison of the sample after 2 and 4 reductions* [152].

Stability of SFNM-04 in CO_2 environment was investigated too. Indeed, the main concern about the sample was that nickel presence in the lattice could accelerate $SrCO_3$ formation because of the reaction of SrO with the CO_2 surface absorption; this brings to the creation of a stabile phase of $SrMoO_4$, which is an insulant and so compromises the performances in presence of a hydrocarbon fuel. The formation of these two phases was both reported in literature [157] and also found by the University of Udine during XRD and TGA analysis of untreated sample and on one treated with 30% C_3H_8 at 800°C for two hours: the difference between the two case is evident from Figure 2.32.

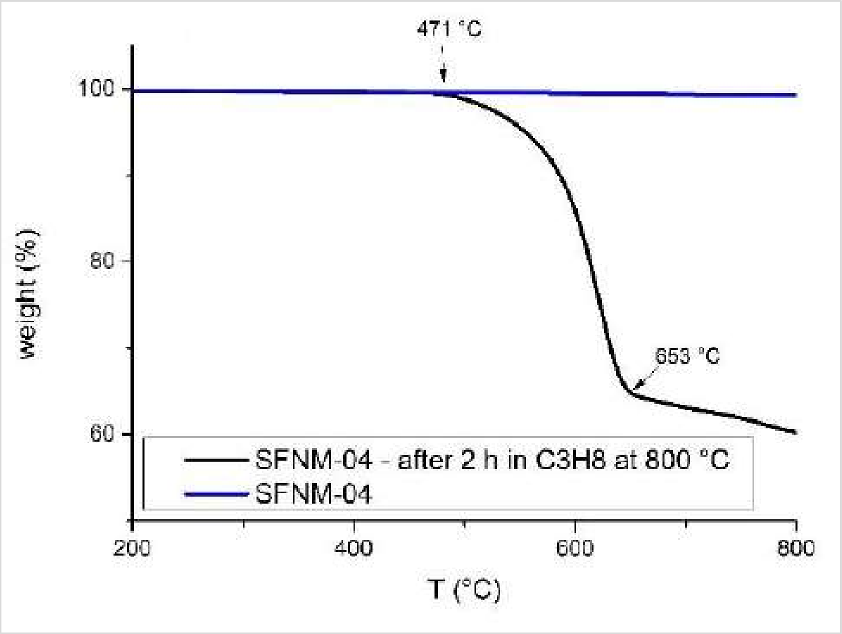

***Figure 2.32**: TGA for treated SFNM04 (black curve) and untreated (black curve) [80].*

In conclusion, the SFNM-04 double perovskite material has been described in this chapter. Further characterization will be provided in the following chapters, thanks to experimental tests performed in the laboratory.

Chapter 3

3. Experimental Set up

3.1 Chemical Looping Test Bench

In this chapter the test bench used to investigate the redox performance of SFNM-04 in chemical looping application is described. The bench is located at the CO_2 Circle Lab in the Environment Park of Turin, Italy. Schematic of the experimental bench is presented in Figure 3.1.

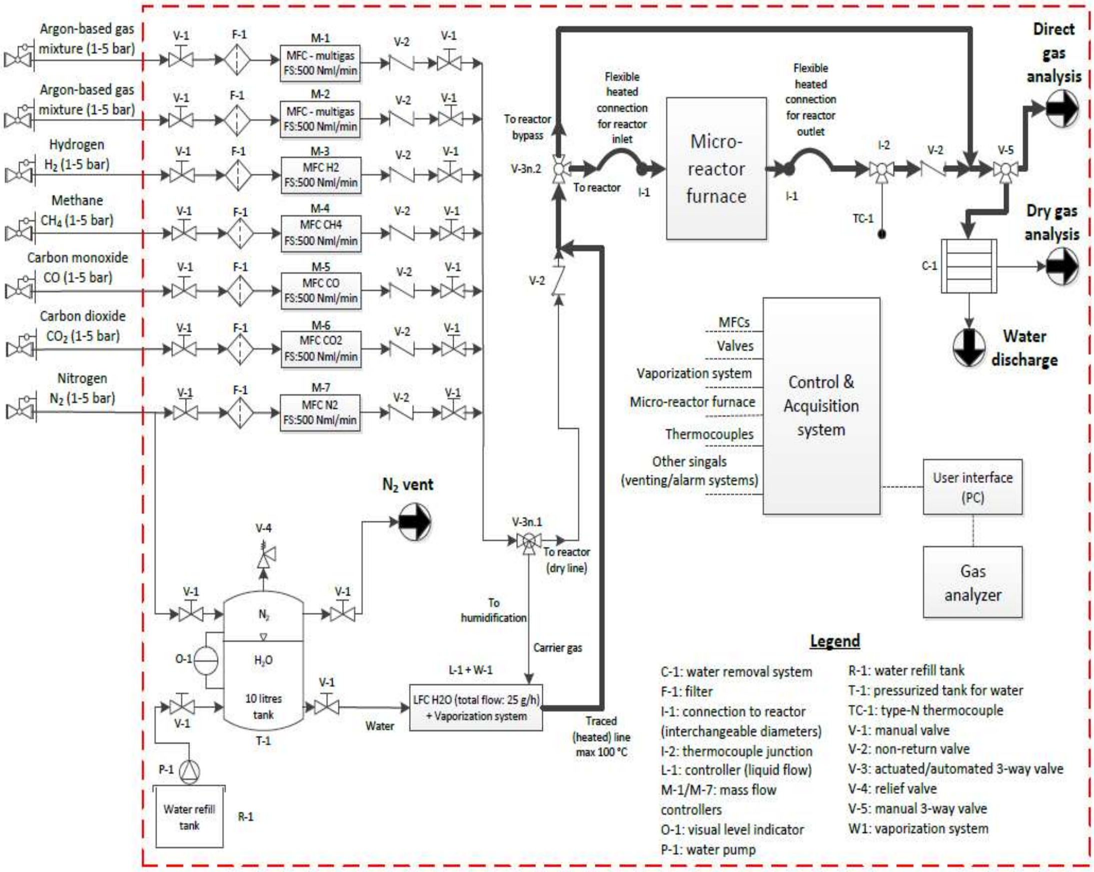

Figure 3.1: *Schematic of the used CL test bench.*

The description can start from the left-up part of the figure and then follows the real flow of the gases. Here there are mass flow controllers (Bronkhorst EL-FLOW) that are used to feed the system automatically, with the wanted mass flow set from remote control. This system includes a steam generation unit and seven gas lines: as it is indicated in the figure the supplied gases are N_2, CO_2, CO, CH_4, H_2 (which come from laboratory lines using pressure reducers) and two on-site cylinders activated through pressure reducers directly installed on them. Except the nitrogen gas lines where the pressure is imposed at $3.5\text{-}5\ bar$, all the other lines present a pressure of $2.5\ bar$. The N_2 line is kept at a higher pressure because it is also used to pressurize the tank of demineralized water. Downstream the pressure reducers (valves V-1), there are the mass flow controllers (MFCs): the connection pipes are made of steel for the lines connected to the laboratory feeding and of Teflon for ones connected to cylinders. The possible mixture contained in the two cylinders are $Ar\text{-}H_2$ (5 % max), $Ar\text{-}CH_4$ (5 % max), $Ar\text{-}CO_2$ (5 % max), $Ar\text{-}O_2$ (5 % max), and air mixture. The MFCs are necessary to control, regulate and measure the gases instantaneous flow rate. After MFCs, all gas pipelines merge into a three-way valve (V-3n.1) where can be chosen if sending a dry mixture to the reactor or otherwise adding steam and so humidifying before the entry. It must be noticed that, for this work, humidified mixtures have never been used. The second three-way valve (V-3n.2) gives the possibility to send the gas mixture on the reactor or, alternatively, the bypassing of the reactor (sending the gases directly to the analyser). This valve is very important, because it allows the proper calibration of the following instruments, as well to understand the delay seen in the analyser due to gases passing through the reactor. After that we arrive at the core of the system, the microreactor. It is an electric furnace (Carbolite Gero) with an alumina tube inside (where samples are positioned) and it is designed to guarantee isothermal condition until 1600°C (while the minimum is environmental temperature). After the microreactor there is a manual valve (V-5) that allows to send the exiting gases to the condenser or directly toward the gas analyser system. The instrument used to analyse the outlet gas composition is an Emerson X-stream gas analyser, which measures the concentration of some gases (CO_2, H_2, O_2, CH_4, CO). The outlet of the gas analyser is connected to the vent.

***Figure 3.2**: Photo of the test bench. From the left: one of the cylinders and the wall pipelines, the MFCs, pressure reducers and the microreactor on the right.*

3.1.1 Microreactor and Furnace Section

This work is incorporated in a research study that is started some years ago. To date, most of the test to evaluate the redox performance of the oxygen carrier material for WS/CDS through chemical looping employed a Thermogravimetric analysis (TGA), and the same generally is done in literature studies. However, using a microreactor instead of a TGA presents some advantages and therefore this option was preferred in this work. Some of these advantages are an enhanced heat and mass transfer mechanism, and a more flexible setup of the microreactor with a higher efficient control of the parameters. Another important difference relies in the measuring method of the two instruments: TGA evaluates a mass variation of the sample and is based on a balance mechanism, but doesn't show if the mass variation is due to the occurring of the actual redox reactions, the formation of other chemical species (such as carbonates) or for the carbon deposition phenomena; the microreactor coupled to the gas analyser, instead, measures directly the CO produced during the oxidizing step. Furthermore, with this set up, the sample analysable is bigger than in TGA and the interaction of the fluid stream with the tested sample is more effective, thus approaching the scale of a realistic application. The sample weight generally used in TGA is up to *10÷15 mg,* while in the microreactor we used a SFNM-04 sample of *200 mg.* The microreactor located in the lab is the Carbolite Gero [158] and is connected to a power supply unit (PSU) as shown in Figure 3.3: this component supplies the electricity to the resistance inside the reactor, allowing to reach the selected temperature and to keep the isothermal environment. The electric furnace is controlled by an Eurotherm PID of Schneider Electric, which allows the remote control of the temperature, with the possibility of setting a pre-fixed temperature program through to the software Eurotherm iTools [159]: this is very useful to perform the thermochemical cycle, because in this way we can set both the ramp temperature (up and down) in terms of K/min, and also the duration of the isothermal steps.

Figure 3.3*: The Carbolite Gero microreactor (left) and the PSU (right).*

The used microreactor is classified as a continuous flow reactor with a horizontal alumina tube inside with a length of *1 m* and a diameter of *32 mm,* where the mixture flows. There are also several insulation elements to limit both heat dispersion and flow leakages. In

Figure 3.4, a simplified section of the reactor is showed: both heating and insulation elements can be recognized.

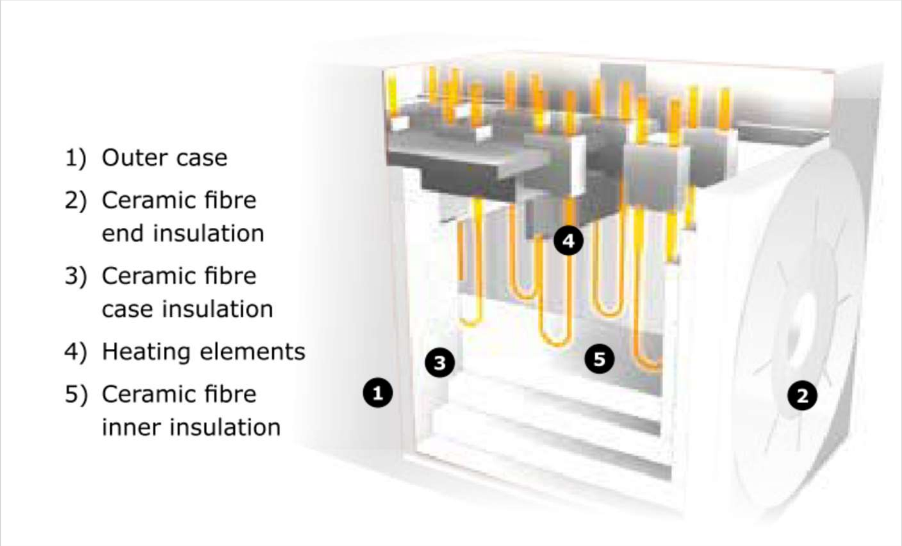

Figure 3.4: *Inside of the Carbolite reactor* [158].

Inside the tube, at the centre, the sample is positioned using an alumina boat-shaped crucible (Figure 3.5). The quantity of the sample used is 200 mg and is accurately measured thanks to an analytical balance with a high level of accuracy and resolution, which provide a protected section to perform the measurement to avoid undesired air currents that could distort the measurement.

***Figure 3.5**: Photo of the alumina crucible with SFNM-04 powders inside.*

Once the temperature program is created, the desired mixture at the inlet of the reactor must be prepared: the composition is selected according to each step and will follow temporally the furnace program. This can be set by using an appropriate SCADA (Supervisory Control And Data Acquisition) software that controls valves and MFCs from a remote computer [160]: in this way gas flows recipes and sequences are created and can be sent simultaneously with the temperature program, allowing the simulation of more cycles automatically. It also can be set manually, useful for calibration of the analyser as example. In Figure 3.6 the interface of this software is showed: there is a simple scheme of the bench with the seven pipelines and the main valves. By closing/opening the first valve (Valve 1) is possible to decide between a dry or humidified mixture, while the second one (Valve 2) controls the bypass of reactor.

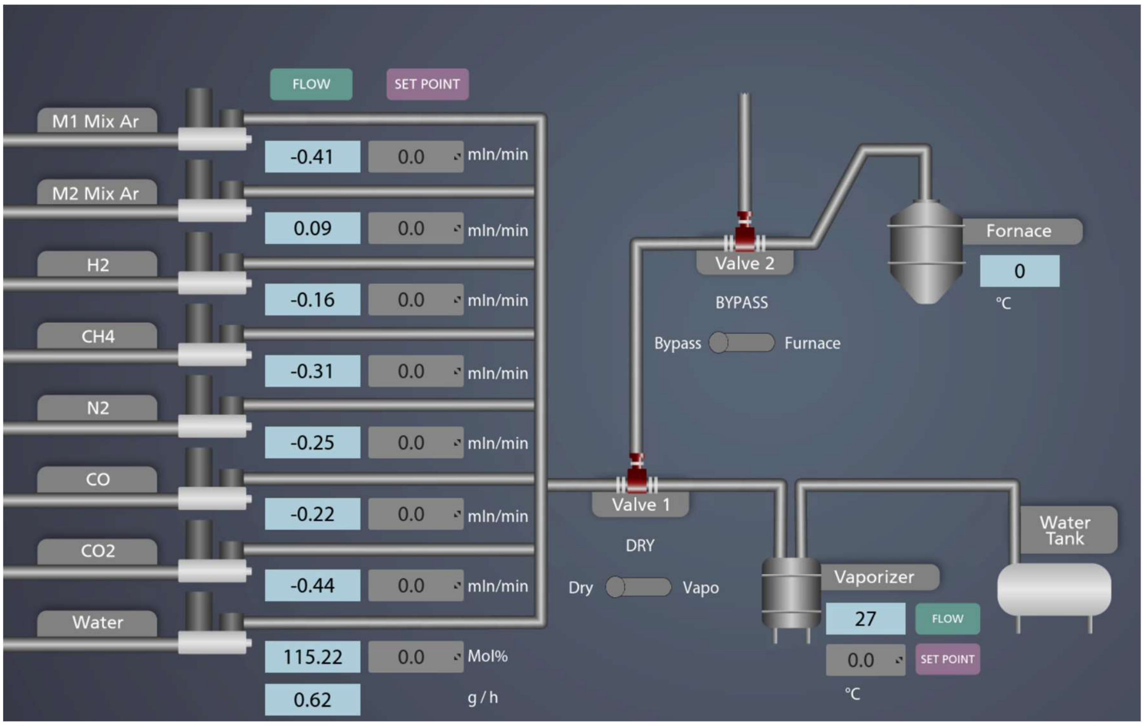

Figure 3.6: Interface of the SCADA software.

3.1.2 Gas Analyser

The used analyser is an Emerson Rosemount X-Stream XE gas analyser. It works appropriately only with dry and conditioned mixtures: so, entering gases must be cleaned in order to eliminate dust or others possible contaminants that will lead to a damaging of the component. In fact, before entering the analyser, gases pass through a condenser where moisture is removed. The instrument performs the analysis using two different types of technology for detection: a Thermal Conductivity Detector (TCD) and an Infrared Detector (IRD). Thanks to this diversification, the instrument can detect and measure the composition of five different species: CO_2, CO, O_2, H_2 and CH_4. Generally, there are two macro areas in which gas sensing technology can be divided [161]: one is based on an electrical variation, while the other is comprehensive of all others type of variation. The choice of one over the other depends on each application and can made basing on different indicators, such as the sensitivity, selectivity, cost, energy consumption, response time and adsorptive capacity.

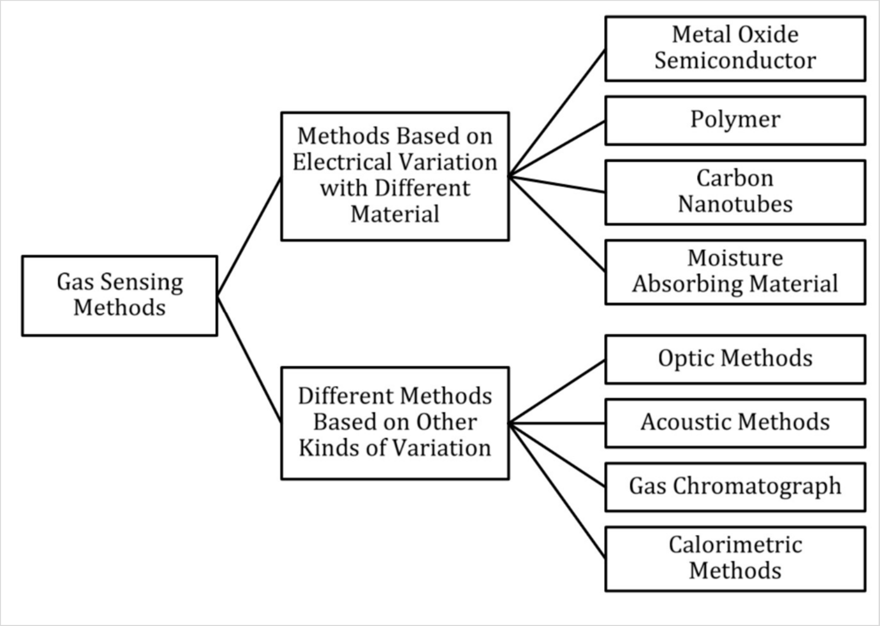

Figure 3.7*: Scheme of different gas sensing methods* [161].

As already reported, Emerson X-Stream uses two different technologies for the detection. The Infrared Detection (IRD) distinguishes different chemical species basing on the amount of irradiated light absorbed by the gas flow: by irradiating the gas with an infrared, the system analyses the different wavelengths that can pass through, while the others are considered absorbed. If this happens, it means that the wavelengths have the same vibrational frequencies of the mixture components; since each atom can vibrate only at its characteristic frequency, it is possible to associate the correspondent chemical specie. This process is described accurately by Twiss at al [162] and is schematized in Figure 3.8. There are two infrared sources which send the infrared radiation through two cells, one compensating cell with air inside and another one in parallel connection containing the investigated sample, and two correspondent sensitized cell; in the first cell the radiation is completely absorbed by the sensitized cell, because air doesn't absorb the IR, while in the other cell some part of the radiation is absorbed and some passes toward the sensitized cell. At the end, the two sensitized cells will present two different temperature and particularly the left one (the one corresponding to just air) will be hotter: this temperature gradient causes a deflection on the gold leaf diaphragm located in the middle of the instrument. The entity of this deflection can be easily translated to determine the content of hydrocarbon in the sample cell.

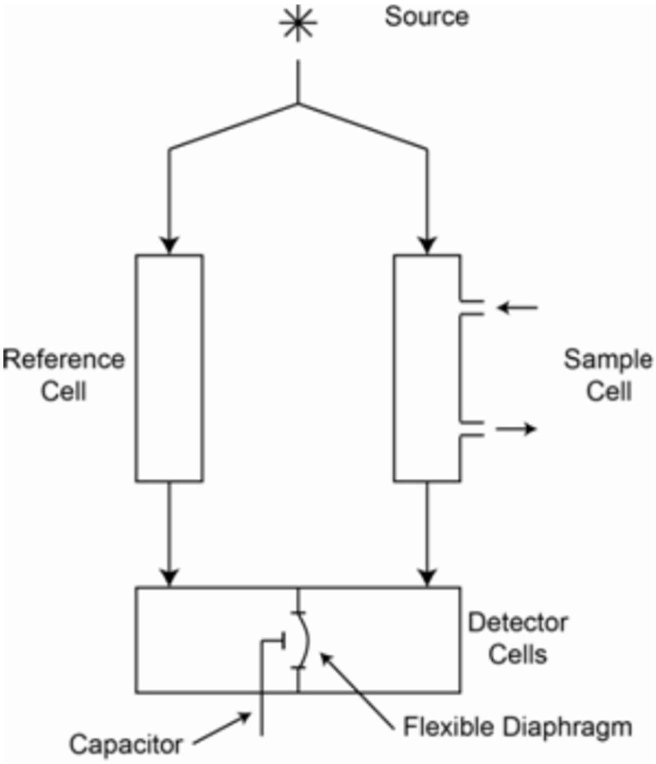

***Figure 3.8**: Example of a scheme for a non-dispersive infrared spectrophotometer* [163].

The other detector of the Emerson is a Thermal Conductivity Detector (TDC), which measures the thermal conductivity of the investigated gas by using a Wheatstone Bridge (Figure 3.9): there are four temperature sensitive resistors with constant current passing through, where one is immersed into the sample gas stream, one to the reference gas stream. When all the four resistances are equal, the output potential in null and the bridge is considered balanced. When the investigated gas is introduced into the sample gas stream, the corresponding resistance will be cooled in comparison to the other reference and the circuit will be unbalanced, producing a signal voltage related to the concentration of chemical species in the sample.

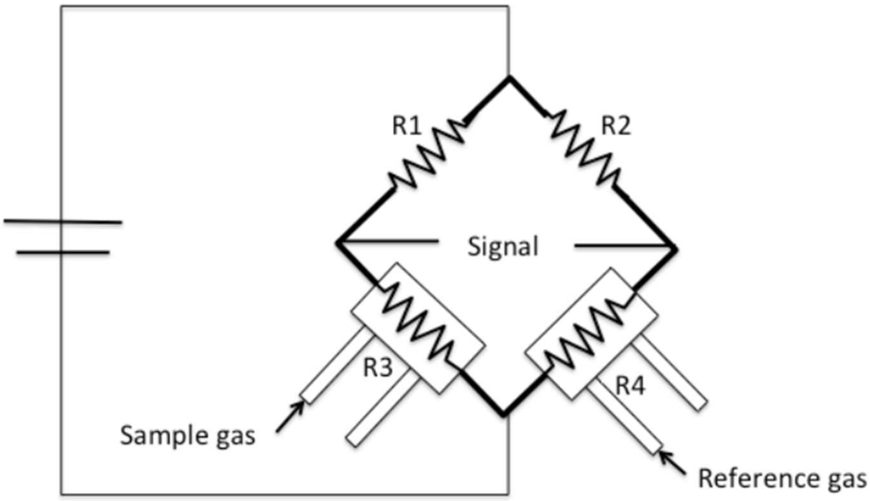

***Figure 3.9**:* A simplified circuit diagram of a thermal conductivity detector [164].

3.2 Preliminary experimental procedures

Before starting the experimental test, some procedures have been adopted. First of all, while the reactor is still cold, the sample of SFNM-04 is inserted in the alumina tube (after a proper weighing of the powder) inside the boat-shaped crucible. During this operation, it is very important that all the pipelines are closed and that the reactor was previously cleaned with purge gas (we used nitrogen) before removing the flanges. The temperature of the reactor must be the environmental one too, with the PSU switched off. At the end of the setting procedure, a leakages test is performed to ensure the sealing of the reactor: in this case, a leakage between the 10% of the sent mass flows was considered acceptable, otherwise the reactor was opened and closed again. When the microreactor was correctly tested, the gas analyser was calibrated. The calibration procedure consists in firstly choose the range of concentration (in volume) for the channels of each measured gas (according to the expected concentrations), then verify the zero and the span value by sending the known concentrations: if the output readings of the analyser didn’t correspond to the sent value, the calibration was performed. At this point both the Emerson X-Stream and the reactor was ready to start with the real experimental test on the sample.

Chapter 4

4. Experimental test on the microreactor

Before starting the description of the tests performed at the lab, some consideration about the CO yield of the cycles must done. The redox performance of the SFNM-04 sample is characterized by changing for each test some parameters, in order to observe the effective behaviour and response of the material according to them. In particular, the temperature range considered, both for oxidation and reduction, is from *550°C* up to a maximum of *850°C;* a higher temperature has not been considered because exceeding was considered ineffective, since the main goal of perovskites research is finding a promising oxygen carrier with good results at temperature lower than traditional material. The gas mixture compositions change from *5%* to *100%* of H_2 for the reduction step, while from *6%* to *100%* of CO_2 during oxidation; in both cases, the remaining complementary part was nitrogen. Pure N_2 gas flow is also used as purge gas between each step and also during the temperature ramp to reach a selected temperature: in fact, each oxidation and reduction step is never performed during a temperature variation, but always in isothermal conditions. Furthermore, the time in which the sample stays in the oxidizing and reducing environment is changed too: for reduction step, the range is from *15* to *120* minutes; concerning the oxidation, the time considered is 30, 90 and 420 minutes. In all the experiments that will be presented the mass of the sample is kept constant at *200 mg* of SFNM-04 and the volumetric mixture flow rate at *200 NmL/min*. N indicates the NTP (Normal Temperature and Pressure) conditions ($T = 293.15\ K\ ,\ \ p = 1\ atm$). In addition, before starting a new test, the sample is always oxidized in air at *500°C* for 1 hours, in order to assure that each test starts from the same fully oxidized condition of the oxygen carrier and to remove possible contaminants.

In the following table (Table 1) all the experimental tests are summarized.

***Table 1**: Scheme of all the test performed with the corresponding experimental parameters.*

TEST		Temperature	Gas Composition	Reactions Times	N° cycles
TEST (I)	Oxy Step	850 °C	20% $CO2/N2$	90 min	5
	Red Step	850 °C	10 % H_2/N_2	60 min	
TEST (II)	Oxy Step	550,650,750,850 °C	20% $CO2/N2$	30 min	5
	Red Step	850°C	10 % H_2/N_2	60 min	
TEST (III)	Oxy Step	750°C for 1-3 cycles 850°C for 4-6 cycles	20-40% CO_2/N_2	30 min	3+3
	Red Step	750°C for 1-3 cycles 850°C for 4-6 cycles	10 % H_2/N_2	60 min	
TEST (IV)	Oxy Step	750°C for 1-10 cycles 850°C for 11-20 cycles	6-100% CO_2/N_2	30 min	10+10
	Red Step	750°C for 1-10 cycles 850°C for 11-20 cycles	10 % H_2/N_2	60 min	

TEST		**Temperature**	**Gas Composition**	**Reactions Times**	**N° cycles**
TEST (V)	Oxy Step	750 °C	6-100% CO_2/N_2	30 min	10
	Red Step	850°C	10 % H_2/N_2	60 min	
TEST (VI)	Oxy Step	850°C	20 % CO_2/N_2	30 min	5
	Red Step	550,650,750,850 °C	10 % H_2/N_2	60 min	
TEST (VII)	Oxy Step	850°C for 1-9 cycles 750 °C for 10-18 cycles	20 % CO_2/N_2	30 min	9+9
	Red Step	850°C for 1-9 cycles 750 °C for 10-18 cycles	5-100 % H_2/N_2	60 min	
TEST (VIII)	Oxy Step	750°C	20 % CO_2/N_2	30 min	9
	Red Step	850 °C	5-100 % H_2/N_2	60 min	
TEST (IX)	Oxy Step	850 °C	20 % CO_2/N_2	30 min	6
	Red Step	850°C	10 % H_2/N_2	15,30,45,60,90,120 min	

TEST (X)	Oxy Step	850 °C	20 % CO_2/ N_2	7 hours	1
	Red Step	850°C	100 % H_2/N_2	2 hours	

4.1 TEST (I): Reference test at *T* = *850 °C* - 5 cycles

The first test performed is isothermal, with the temperature kept constant both for oxidation and reduction. This will be lately referred as reference test for all the others, since also the used gas mixture compositions are the considered nominal ones. During the oxidation step a gas flow with 20% CO_2/N_2 is sent, while 10% H_2/N_2 as reducing mixture. So, the test is composed by 5 identical cycles, each one with the same conditions: the main goal of this experiment is indeed to analyze and study the repeatability and so the stability of the SFNM-04 sample. The temperature program is set with a 20°C/min for the upward ramp until 500°C (where it is kept for one hour dwelling) and then with a 10°C/min ramp until 850°C is reached: at this point the real redox cycles can start. Each cycle is composed by the same steps sequence:

- Purging step with 100% N_2 for 5 min.
- Reduction step with a 10% H_2/N_2 gas mixture for 60 min.
- Purging step with 100% N_2 for 5 min.
- Oxidation step with a 20% CO_2/N_2 gas mixture for 90 min.

The results of the experiment coming out from the gas analyser are post-processed in order to evaluate the CO production rate in $[\mu mol/g \cdot s]$. The instrument gives an output of CO in $[ppm]$ terms, second by second (real time data). A proper procedure for the conversion is applied:

1- $[ppm]$ values are divided by 10^6 to obtain dimensionless numbers $[-]$.

2- Dimensionless values are multiplied by the volumetric flow rate and divided by the number of seconds in an hour, obtaining in this way the normal volumetric flow, but per second. The performed calculations are:

$$[-] \cdot 200 \left[\frac{NmL}{min}\right] \cdot \frac{1}{60}\left[\frac{min}{s}\right] = \left[\frac{NmL}{s}\right] \tag{4.1}$$

3- By using the Ideal Gas Law, the volume flow is converted into mole flow, considering that the molar volume of an ideal gas is constant and equal to 22.4 L. Once the litres are transformed in moles, they are multiplied by 10^3 to obtain a micro dimension. The followed procedure is:

$$\left[\frac{NmL}{s}\right] \cdot 10^3 \left[\frac{\mu L}{mL}\right] \cdot \frac{1}{22.4}\left[\frac{mol}{L}\right] = \left[\frac{\mu mol}{s}\right] \tag{4.2}$$

4- Finally, dividing the values by the sample mass (200 mg) and multiplying by 10^3 we achieve the desired unit of measurement:

$$\left[\frac{\mu mol}{s}\right] \cdot \frac{1}{200\ [mg]} \cdot 10^3 \left[\frac{mg}{g}\right] = \left[\frac{\mu mol}{g \cdot s}\right] \tag{4.3}$$

Following this procedure, the CO production rate is available for each second of the test. To have a comprehensive idea of the real final production of CO, we calculate the CO production yield too, expressed in $[\mu mol/g]$: in this case is necessary to find a proper integration method able to consider all the useful data and reject the unwanted ones of the oxidation curve. In fact, by observing the plot of the CO production curve in $[ppm]$ (Figure 4.1), it is evident that the curve presents a long tail that stabilize at almost 1400 ppm, never reaching the zero value. So, in order to avoid considering the negative tail effect, which would bring to a non-reliable CO yield, the first derivative of the curve is calculated: thanks to the derivative, a break point for the calculation of the yield is set once the value of the derivative function is under a tolerance range of $\pm$ 0.05 %. As it can be seen in Figure 4.2, this procedure seems conservative but necessary to find a reliable CO yield, since a variation lower of this value for the derivative means that the tail has reached a constant value and so we can consider fair the elimination of further fluctuations.

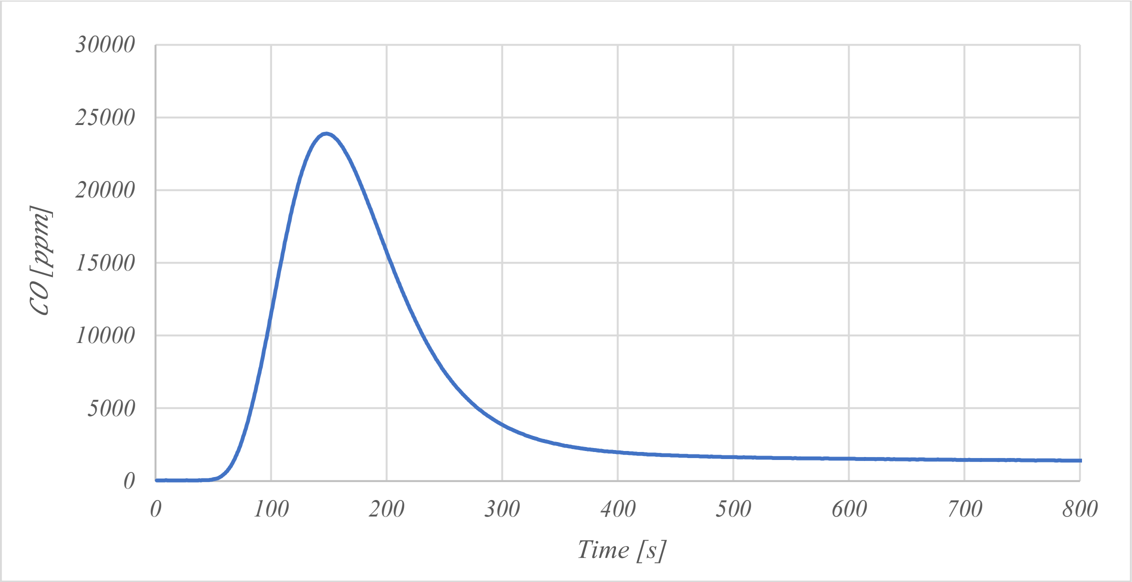

Figure 4.1: *CO production rate in [ppm] during the oxidation step with 20% CO_2/N_2.*

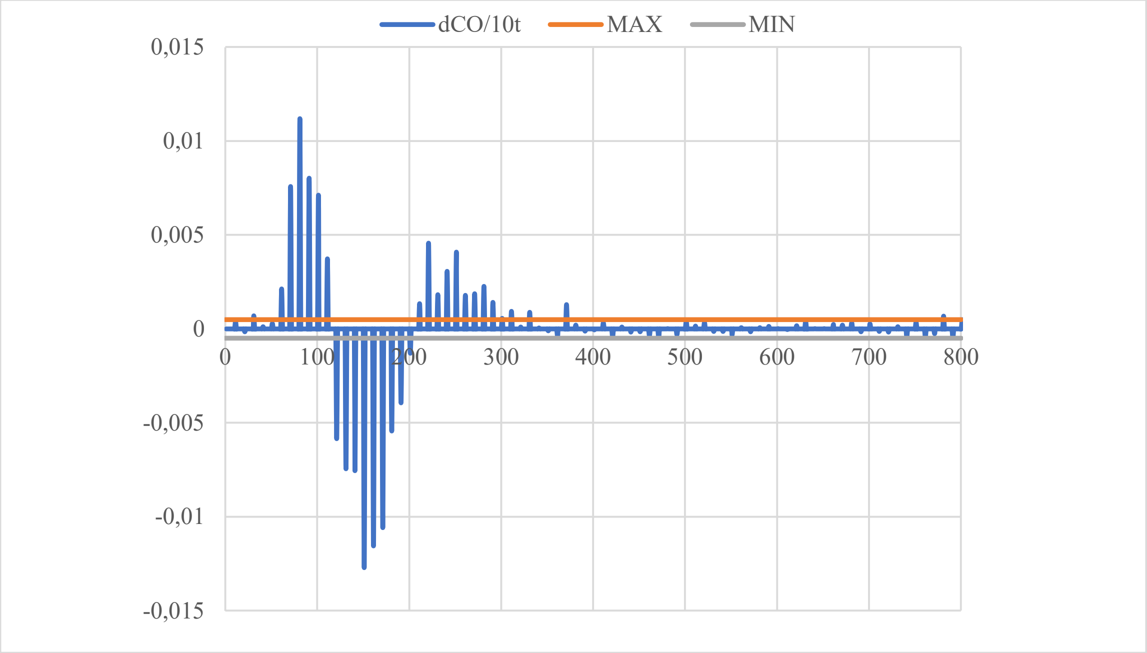

Figure 4.2*: First Derivative of CO production rate (in ppm) considering 10 subsequent time steps (blue lines). Maximum tolerance is represented by the orange line and minimum by the grey line.*

Analysing the derivative curve, the oxidation step can be considered finished after 450 s of reaction. In order to eliminate further values, a straight line is drawn starting from the beginning of the curve (first positive value above some ppm) and end at this breaking point:

in this way a lower limit for the integration is set and a real, reliable CO yield can be found. The method is graphically showed in Figure 4.3, while in Figure 4.4 is reported the final CO curve, whose integral represents the global CO yield in $[\mu mol/g]$.

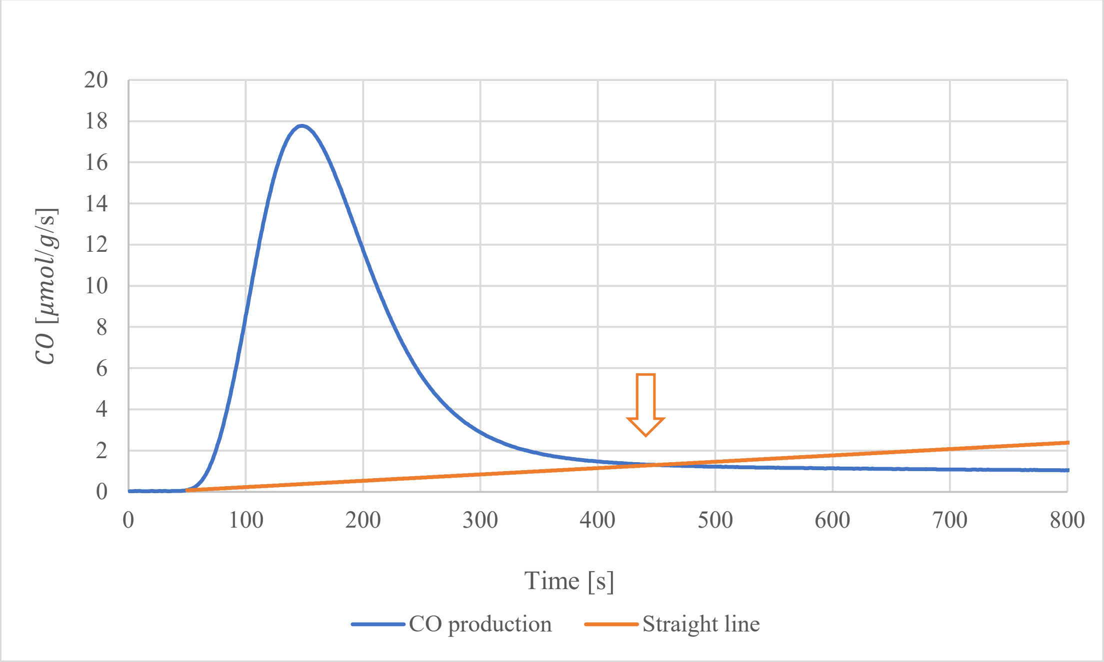

***Figure 4.3**: CO production (red curve) cut by the straight line (blue line) at t=450 s.*

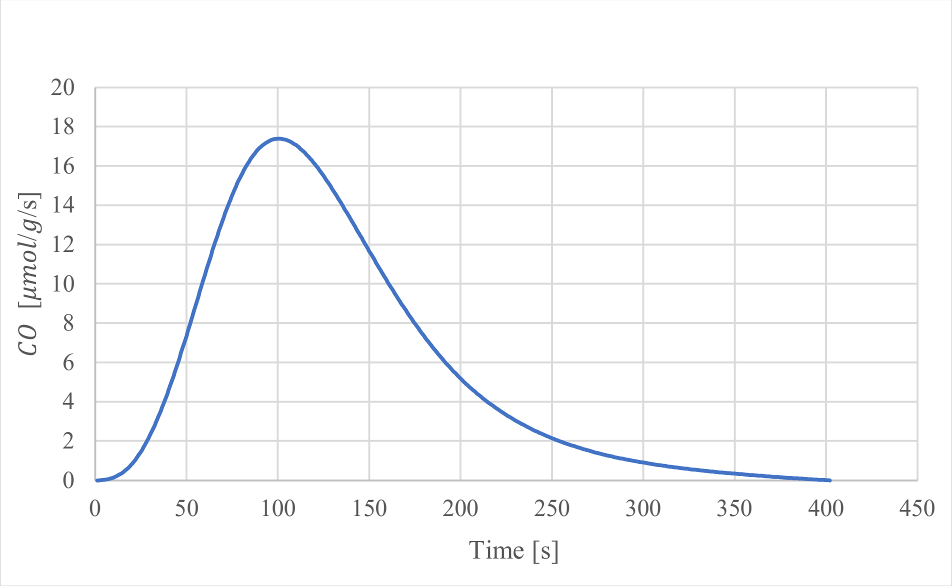

***Figure 4.4**: Final evaluation of the net CO production obtained subtracting for each second the values of the CO production curve to the values of the straight line.*

This procedure of integration is employed also for all the following tests and won't described again for each subparagraph. In Figure 4.5, the final CO production curves of all the cycles of TEST(I) are presented; on the left axis there is the production rate of CO calculated in $[\mu mol/g \cdot s]$, while on the right one there is the same quantity but expresses in [%] terms.

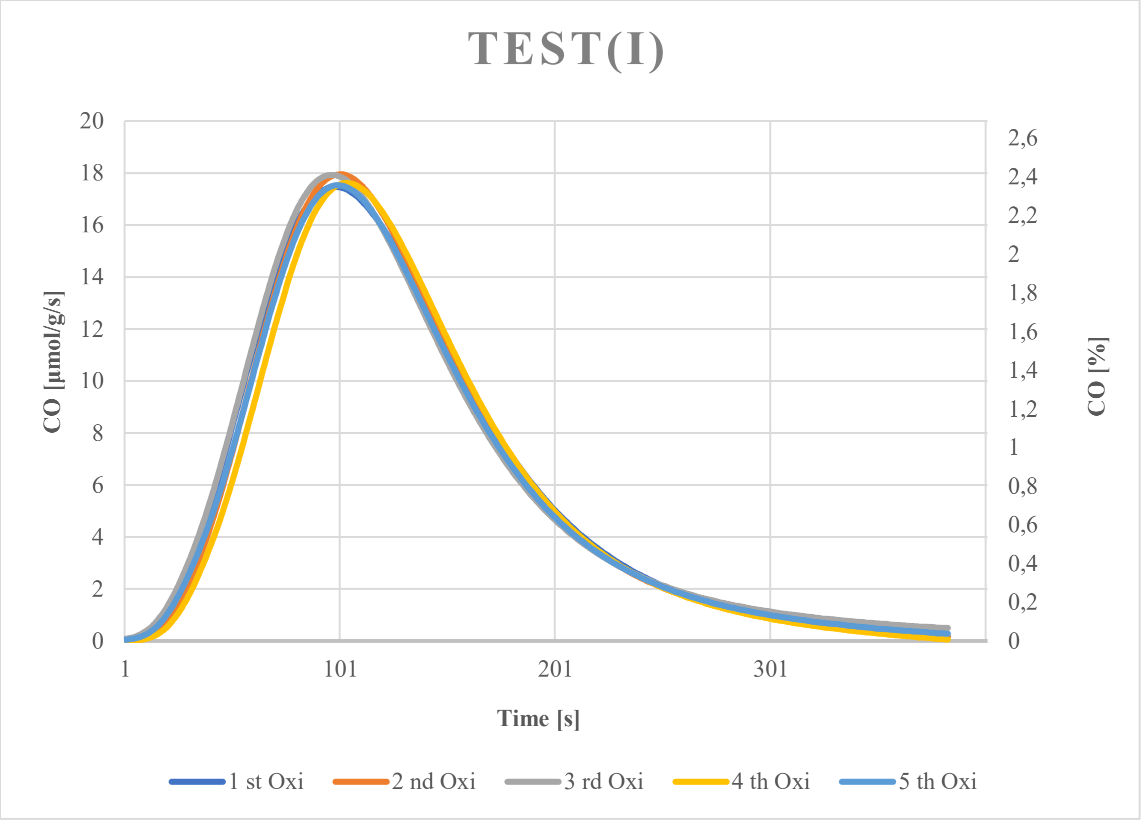

***Figure 4.5**: CO production of TEST(I).*

The five resulting curves shows a very similar trend and so we can assert the SFNM-04 stability over the cycles: this material shows a repeatable behaviour throughout the whole process and so can be considered as suitable material for chemical looping applications. The curves show a fast initial increasing of CO until a peak is reached, and finally a rough decrease. This is explained because at the beginning the ion incorporation inside the oxygen vacancies is very rapid, since the sample was previously reduced: the five cycles show a comparable redox kinetics. The maximum CO production rate is 18 $[\mu mol/g \cdot s]$, which correspond to a percentage of 2.4 % of CO produced. In the following table (Table 2) all the results are summarized, with CO_2 yield presented both in $[\mu mol/g]$ form and in percentage. Furthermore, the CO_2 conversion is also listed. This data is calculated by dividing the maximum CO obtained in % (peak value) with the initial content of CO_2 in the mixture. In this way we have a quantity of how much carbon dioxide is split and turn to CO. The calculation used is:

$$\frac{CO\ yield\ [\%]}{\frac{CO_2\ [\%]}{100}\ [-]} = CO_2\ converted\ [\%] \tag{4.4}$$

The last two columns contain an evaluation of the mass exchanged during oxidation in terms of grams of O_2 and CO respectively, with respect to the sample mass. For the calculation, the splitting reaction is considered as completely stoichiometric, with a molar ratio 1:1 of both the oxygen and carbon monoxide. The procedure applied to calculate these values is presented in the following equations, where 16 g/mol and 28 g/mol are the molar mass of O and CO respectively.

$$CO\ yield\ \left[\frac{\mu mol}{g_{SFNM}}\right] \cdot 16\ \left[\frac{g_O}{mol}\right] \cdot 10^{-6} \left[\frac{mol}{\mu mol}\right] = \frac{g\ (O)}{g\ (SFNM)}\ \left[\frac{g_O}{g_{SFNM}}\right] \tag{4.5}$$

$$CO\ yield\ \left[\frac{\mu mol}{g_{SFNM}}\right] \cdot 28\ \left[\frac{g_{CO}}{mol}\right] \cdot 10^{-6} \left[\frac{mol}{\mu mol}\right] = \frac{g\ (CO)}{g\ (SFNM)}\ \left[\frac{g_{CO}}{g_{SFNM}}\right] \tag{4.6}$$

***Table 2**: Results of TEST (I) for each cycle: CO yield in* $[\mu mol/g]$*, maximum CO yield in* $[\%]$*, CO_2 conversion rate in* $[\%]$*, $g(O)/g(SFNM)$ and $g(CO)/g(SFNM)$.*

N° Cycle	$\boldsymbol{CO}$ **yield** $[\boldsymbol{\mu mol/g}]$	**Max** $\boldsymbol{CO}$ **[%]**	$\boldsymbol{CO_2}$ **conversion [%]**	$\boldsymbol{g(O)/g(SFNM)}$ $[\boldsymbol{g_O/g_{SFNM}}]\cdot\mathbf{10^{-2}}$	$\boldsymbol{g(CO)/g(SFNM)}$ $[\boldsymbol{g_{CO}/g_{SFNM}}]\cdot\mathbf{10^{-2}}$
1	2278	2.35	11.75	3.65	6.38
2	2239	2.41	12.05	3.58	6.27
3	2286	2.41	12.05	3.66	6.40
4	2173	2.37	11.85	3.48	6.08
5	2212	2.36	11.80	3.54	6.19

After the graphical evaluation, also analytical results confirm the repeatability of the SFNM-04 during cycles. The average yield reached for CO is about 2238 $[\mu mol/g]$, corresponding to an average carbon dioxide conversion of 11.9%. The last two column values are very important, because indicate a relative value of the quantity of oxygen and CO exchanged with this material: this is crucial, also to compare the sample under investigation with the studies already present in literature. Particularly, they mean that from a sample of 0.2 g of SFNM-04, almost 0.036 g of oxygen and 0.063 g of CO are exchanged.

4.2 TEST (II): Test with different oxidation temperatures - 5 Cycles

In the first part of the tests, in particular from TEST (II) to TEST (V), the experimental analysis focused on studying the behavior of the SFNM-04 material when oxidation parameters are changed. Indeed, this test in performed by keeping constant reduction conditions for all the five cycles of the test, while varying the oxidation temperature. More in detail the first and last cycles are set at the same conditions (850 °C), in order to check if the sample behave in the same way or if the oxidation at lower temperatures bring some effect on the following cycles, while the other temperatures are set respectively at 550 –

650 – 750 °C. The reduction temperature is kept constant at 850°C, as well as the concentration of H_2 (10%/N_2) and the CO_2 one used for the oxidizing environment (20%/N_2). The temperature program follows a 20 K/min ramp for reaching the 500°C (at which the air oxidation step is performed for 1 hour), and then a 10 K/min ramp until the temperature reduction. The procedure for the 5 cycles is:

- Reduction step at 850°C and 10% H_2/N_2 for 60 min.

- Purging step with 100% of N_2. The duration of this step varies during the cycle because correspond to the temperature ramp up or down between oxidation and reduction. In particular, for the first cycle it lasts 10 min, corresponding to the cooling ramp until 550°C for the second cycle; the same is performed for cycles 3 and 4, but until 650°C, 750°C, and finally again 10 min at isothermal temperature for cycle 5.

- Oxidation step with a 20% CO_2/N_2 gas mixture for 30 min, with temperature of 850°c (cycle 1), 550°C (cycle 2), 650°C (cycle 3), 750 °C (cycle 4), 850°C (cycle 5).

- Purging step with 100% N_2 for 10 min (cycle 1), ramp upward to 850°C for cycles 2,3 and 4 and ramp- down until room temperature for the cycle 5.

In the following, both the graphical and numerical results of the test are presented. Once again, the sample confirms its repeatability by observing the first and fifth cycle values and curves, and both are similar to ones obtained in the reference (TEST (I)). In figure 4.6 and Table 3 the results are illustrated, as already explained in the previous paragraph for TEST (I).

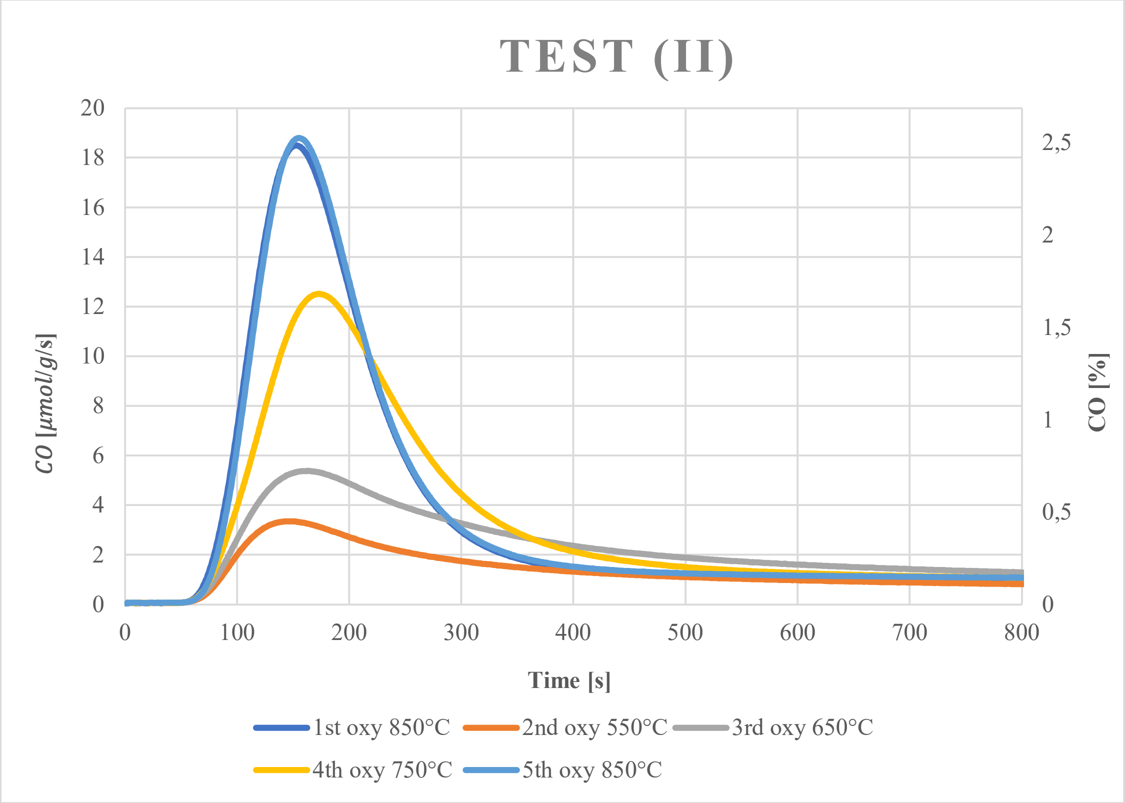

***Figure 4.6**: Resulting curves from TEST(I) of the CO production rate.*

***Table 3**: Results for each redox cycle of TEST (II).*

N° Cycle	T_{OXI} [°C]	CO **yield** [$\mu mol/g$]	**Max CO [%]**	CO_2 **conversion [%]**	$g(O)/g(SFNM)$ [g_O/g_{SFNM}] $\cdot 10^{-2}$	$g(CO)/g(SFNM)$ [g_{CO}/g_{SFNM}] $\cdot 10^{-2}$
1	850	2276	2.49	12.43	3.64	6.37
2	550	825	0.45	2.25	1.32	2.31
3	650	1534	0.72	3.62	2.45	4.30
4	750	1864	1.68	8.41	2.98	5.22
5	850	2274	2.53	12.63	3.64	6.37

The good influence of a high temperature of oxidation is evident analysing these results. The maximum production rate is reached at temperature of oxidation of 850°C and corresponds to 18 [$\mu mol/g \cdot s$]. The redox kinetics of each cycle follow the same trend (also equal to the reference test), with a fast initial CO increase for the first ionic incorporation and then an abrupt decrease. It can be stated that the temperature influence is strongly effective on the global yield of carbon monoxide produced. The difference in peaks between 550°C curve and 650°C is not so significant as the one occurring between 750°C and 850°C: this can be explained by the fact that at lower temperatures the kinetics is so slow that the CO yield stay low. Increasing the temperature, the kinetics presents an acceleration and the difference in CO produced between various temperature is more evident. The last cycle results indicate that the material reactivity is not affected by the previous cycles performed at lower temperature: the first and the last curve almost overlap. The numerical results confirm what already showed by the curves: at 850°C oxidation the CO yield is almost 3 times higher than at 550°C, while the converted CO_2 is six times higher in comparison to the 550°C step and 4 times higher for the 650°C one. It has to be noticed that the main aim of this work, as all the studies towards alternative materials for chemical looping application, is to find oxygen carriers with high performance obtained at low temperature. There are already good performing materials, such as ceria, but they need reduction temperature very high: in this optic, it is more relevant to investigate materials that can work at lower temperatures. However, when the temperature is too low, the performances are lower (as it can be seen from this simulation results) and, especially in oxidation, some undesired phenomena can happen, like the carbonates formation caused by CO_2 adsorption on Sr atoms: this affects a lot the final production because all the CO_2 turned into carbonate compounds ($SrCO_3$) means less availability for splitting and creation of CO, which is the useful effect.

4.3 TEST(III): Test with different CO_2 content – 6 cycles

In this test the behavior of the material according to the variation of oxidation parameters is further investigated. In this case the CO_2 content in the gas flow used during the oxidation step is changed while isothermal cycles are performed, three of them at 850 °C and the other three at 750°C. A temperature ramp after cycle 3 is used in pure nitrogen until reaching the second temperature. For each of these two temperatures the used CO_2 concentrations are 20-30-40%/N_2 and kept for a duration of 30 min. Concerning the reduction step, it is always with 10% H_2/N_2 gas mixture for 60 min. In the following the graphical and numerical results are reported.

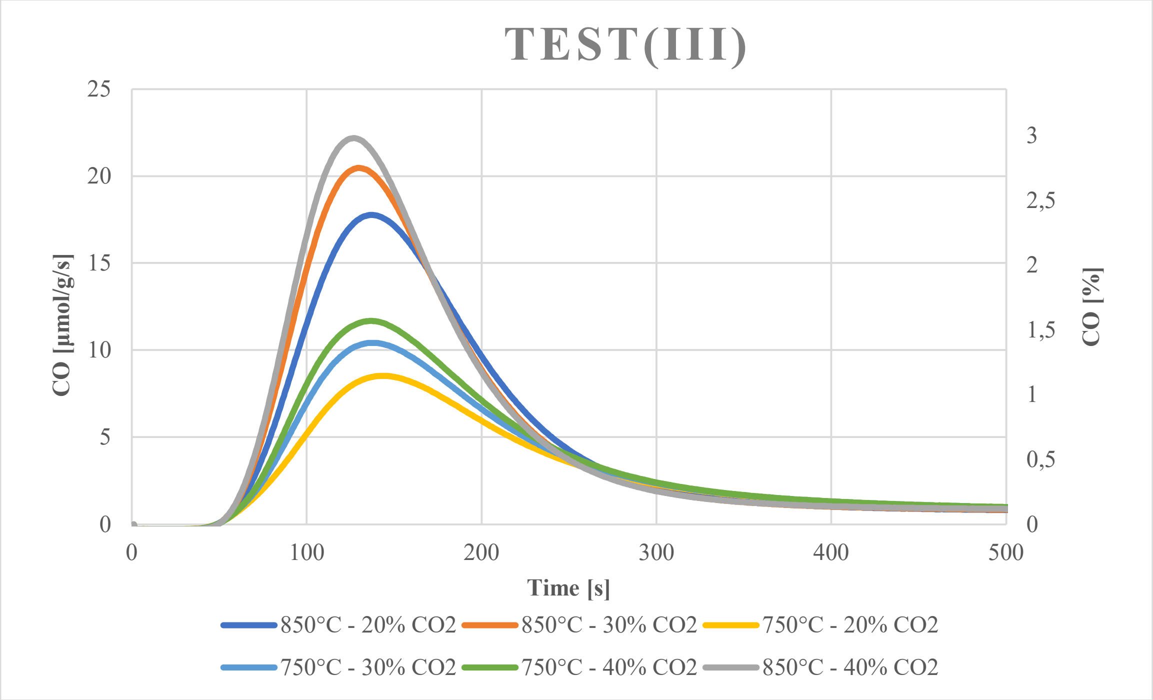

Figure 4.7: *Resulting curves from TEST(III) of the CO production rate.*

Table 4: *Results for each redox cycle of TEST (III).*

N° Cycle	T_{OXI} $[°C]$	CO_2 Content [%]	CO yield $[\mu mol/g]$	Max CO [%]	CO_2 conversion [%]
1	850	20	2183	2.39	11.94
2	850	30	2224	2.75	9.17
3	850	40	2341	2.98	7.46
4	750	20	1444	1.15	5.74
5	750	30	1634	1.40	4.67
6	750	40	1789	1.57	3.93

Once again, the importance of the temperature of oxidation is demonstrated: cycles oxidated at 850°C have significantly higher curves. The other interesting behaviour that can be observed is how the peaks change with different concentrations of CO_2: when this concentration increases, the production of the fuel clearly increases. The most profitable situation is obtained at 850°C with 40% CO_2/N_2 and reaches almost 22 $[\mu mol/g \cdot s]$ and so a 3% in volume of CO; sequentially for this temperature the production rate found are 20 $[\mu mol/g \cdot s]$ (with 30%CO/N_2) and 17 $[\mu mol/g \cdot s]$ (with 20%CO/N_2). Concerning the cycles at lower temperature, the trend remains the same but with lower values (the maximum is about 10 $[\mu mol/g \cdot s]$. The explanation for this phenomenon can be found in the fact that if the concentration of carbon dioxide is higher, hence its quantity is bigger, the probability that CO_2 molecules occupy the free oxygen vacancies is higher: so, more CO_2 in the oxidation gas mixture is found to promote better the oxidation of the reduced sample. A variation in kinetics can be observed too: when the entity of CO_2 is higher, the peaks are slightly shifted towards left in comparison to the lower ones, meaning that the redox kinetics is faster. This is expected, because the increased CO_2 concentration in the flux means that its partial pressure grows: the partial pressure gradient of carbon dioxide between the oxidizing flow and the sample surface is also higher, and the oxidation results more favorable. This behaviour is confirmed checking the numerical results of the postprocessing. It is confirmed again the importance of the temperature, especially when it is so high: a variation in the oxidizing condition of just 100°C bring a percentage variation in the converted CO_2 of more than 4 points. On the other hand, in this case the influence of the CO_2 concentration is less visible and almost negligible, presenting very similar values of the CO yield and maximum CO production. However, it must be noticed that this test is a preliminary analysis for the study of CO_2 content variation: lately, a wider range of concentrations is investigated.

4.4 TEST (IV): Test with different CO_2 content – 20 cycles

In this test the range of CO_2 percentage in the oxidizing gas mixture is extended from 6% to 100%. It is composed by ten cycles with all the variation of CO_2 at 750°C and then by further ten cycles with the same parameters but with temperature of 850°C; the duration of each oxidation is 30 min. The simulation is therefore a copy of the TEST(III) but extended, and also in this case the two temperature cases are considered. Each redox cycle is isothermal, so the reduction temperature follows the correspondent oxidation one, while for each of the 20 cycles a gas flow of 10%H_2/N_2 is used (reduction lasts 60 min). Graphical and numerical results for the first ten cycles are reported in the following.

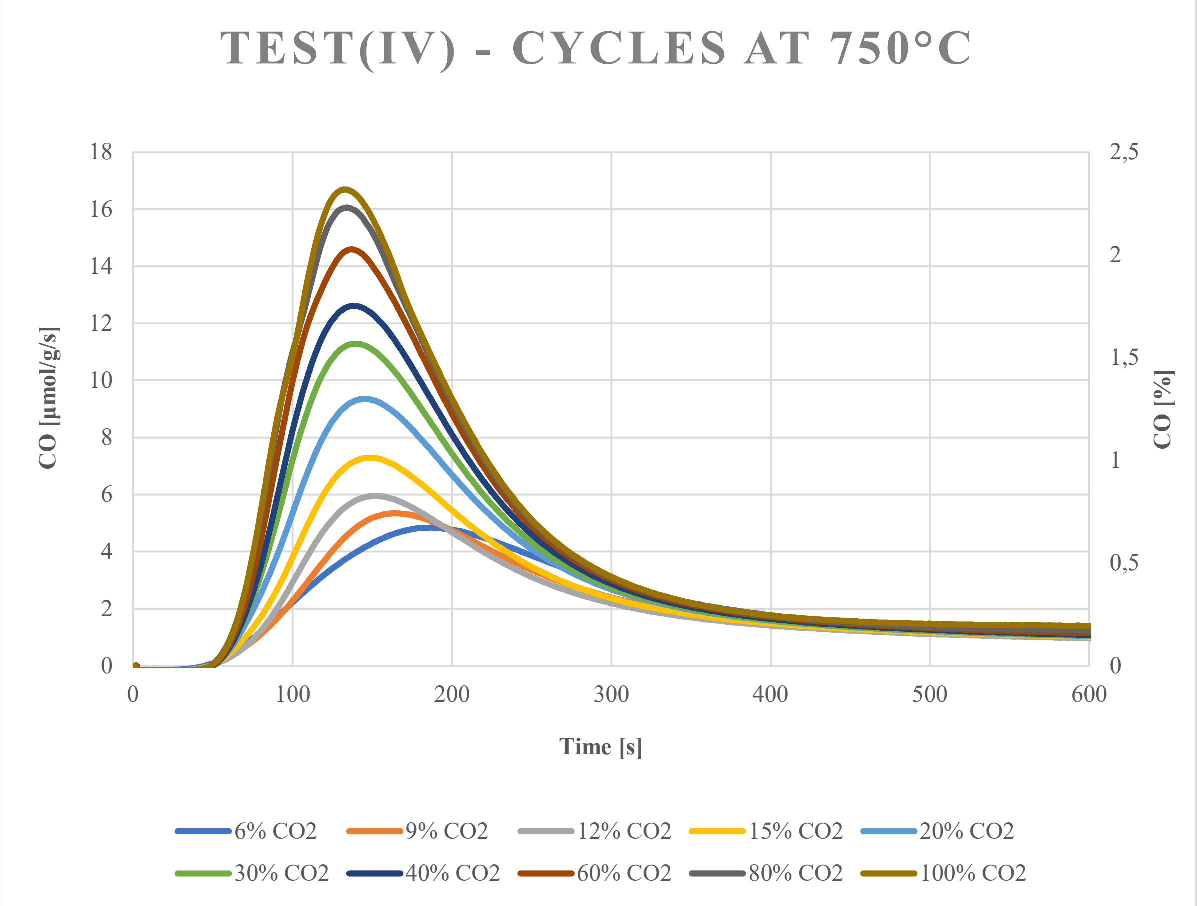

Figure 4.8: *CO Production of TEST (IV) for 10 cycles at 750°C.*

Table 5: *Results for each redox cycle of TEST (IV) performed at T=750°C*

N° Cycle	**CO_2 Content [%]**	**CO yield [$\mu mol/g$]**	**Max CO [%]**	**CO_2 conversion [%]**
1	6	1115	0.65	10.85
2	9	1118	0.72	7.99
3	12	1139	0.80	6.67
4	15	1194	0.98	6.54
5	20	1500	1.26	6.29

6	30	1723	1.52	5.06
7	40	1895	1.70	4.24
8	60	2111	1.96	3.27
9	80	2158	2.16	2.70
10	100	2270	2.32	2.32

As already stated in TEST(III), we can notice that the increment of CO_2 concentration leads to higher final CO production. It can be observed that for 20-30-40% of CO_2 results are consistent with the ones of the previous test, confirming again the repeatability of the SFNM-04 perovskite, even after a high number or cycles. The maximum CO production is obtained with 100% of CO_2, as expected, and it's equal to 17 $[\mu mol/g \cdot s]$, corresponding to a CO yield of 2270 $[\mu mol/g]$; to make a comparison, this value is slightly lower than reference value found with 20% CO_2/N_2 at 850°C. This means that if we want to reduce the oxidation temperature by 100°C, we must use a pure carbon dioxide stream for the oxidation. This can be a problem thinking about the chemical looping integration with carbon capture technology: usually, captured CO_2 from exhaust gases is present with much lower concentration. Now graphical and numerical results for the last 10 cycles at 850°C are reported:

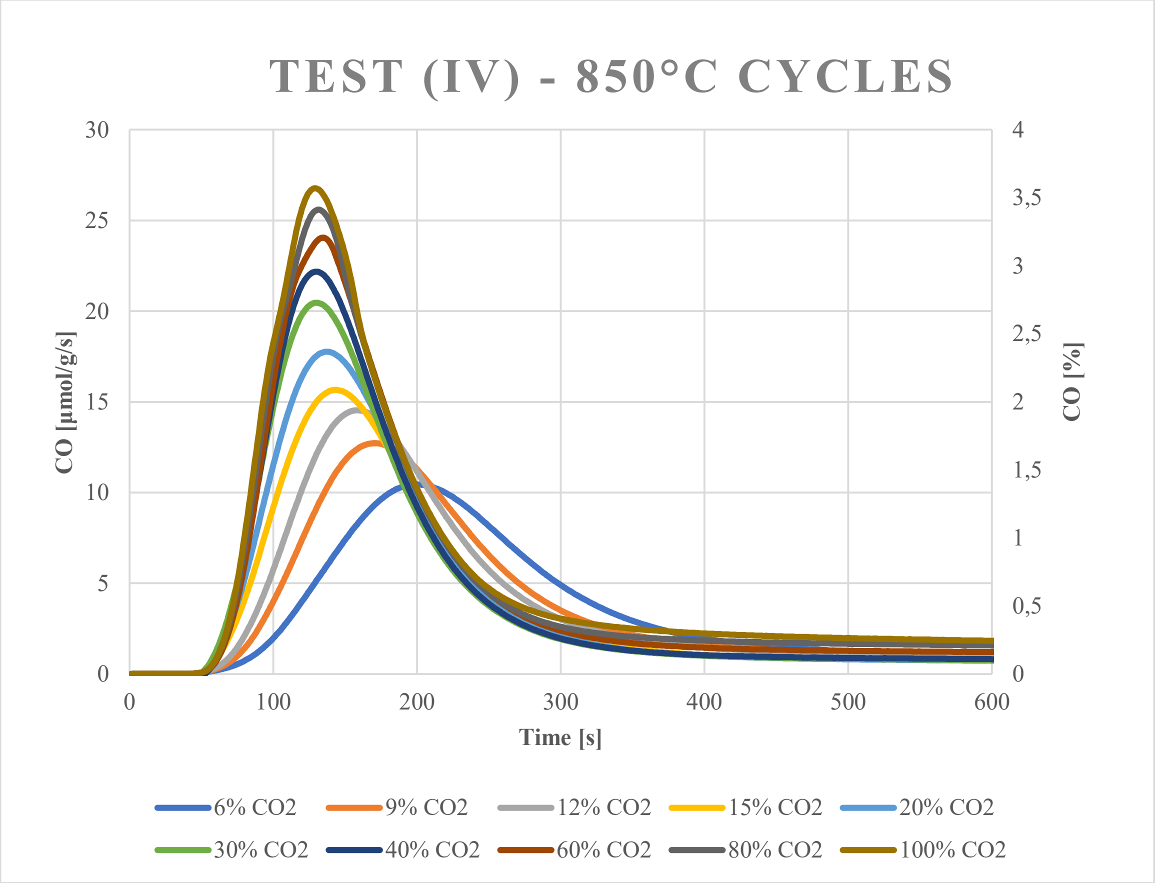

Figure 4.9: *CO Production of TEST (IV) at 850°C.*

Table 6: *Results for each redox cycle of TEST (IV) performed at T=850 °C.*

N° Cycle	CO_2 Content [%]	CO yield [$\mu mol/g$]	Max CO [%]	CO_2 conversion [%]
1	6	1800	1.41	23.43
2	9	1937	1.71	19.01
3	12	2027	1.96	16.29
4	15	2090	2.11	14.04
5	20	2183	2.39	11.94
6	30	2224	2.75	9.17
7	40	2341	2.98	7.46
8	60	2622	3.23	5.39
9	80	2689	3.44	4.30
10	100	2778	3.57	3.57

In this case two new evident phenomena can be observed. First of all, there is a shrinkage of the oxidation curve while increasing the CO_2 concentration, indicating a high difference in the kinetic velocity (faster while CO_2 content increase). Secondly, the difference between a curve and the near one is less evident at high concentration levels, while wider from 6% to 40%: this behavior can be found also in the previous cycles at 750°C, but now is more notable, revealing that the variation in the CO_2 content affects more the results when the percentage is low. In this case the maximum peak value is 26 $[\mu mol/g \cdot s]$, corresponding to a maximum CO yield of 2278 $[\mu mol/g]$. This value is significantly higher in comparison to the maximum found at 750°C: just with a 100°C higher temperature the CO peak value increases from 17 $[\mu mol/g \cdot s]$ to almost 26 $[\mu mol/g \cdot s]$. The repeatability of the investigated material through the cycles is again demonstrated, being the result obtained at 20% CO_2/N_2 almost equal to the reference ones.

__Table__ 7: Results for each redox cycle of TEST (IV) performed at T=850 °C, in terms of exchanged oxygen and mass of CO produced for in respect to the used sample.

N° Cycle	CO_2 Content [%]	Max CO yield $[\mu mol/g]$	$g(O)/g(SFNM)$ $[g_O/g_{SFNM}] \cdot 10^{-2}$	$g(CO)/g(SFNM)$ $[g_{CO}/g_{SFNM}] \cdot 10^{-2}$
1	6	10.11	2.88	5.04
2	9	12.42	3.10	5.42
3	12	14.24	3.24	5.68
4	15	15.45	3.34	5.85
5	20	17.49	3.49	6.11
6	30	20.04	3.56	6.23
7	40	21.78	3.75	6.56
8	60	23.70	4.20	7.34
9	80	25.16	4.30	7.53
10	100	26.08	4.44	7.78

In Table 7 the CO_2 conversions are listed. Plotting the quantity of CO_2 converted as function of the CO_2 concentration in the oxidizing gas, we can notice a logarithmic behaviour: with 6% of carbon dioxide the resulting conversion is almost eight times higher than the one with pure oxidant (23.43% of CO_2 converted against 3.57 %). This trend is reported in Figure 4.10, where on the x-axis there is CO_2 percentage, while the left y-axis corresponds to maximum CO yield (lower curve) and the right y-axis the exchanged grams of oxygen with respect to the mass of the sample (upper curve).

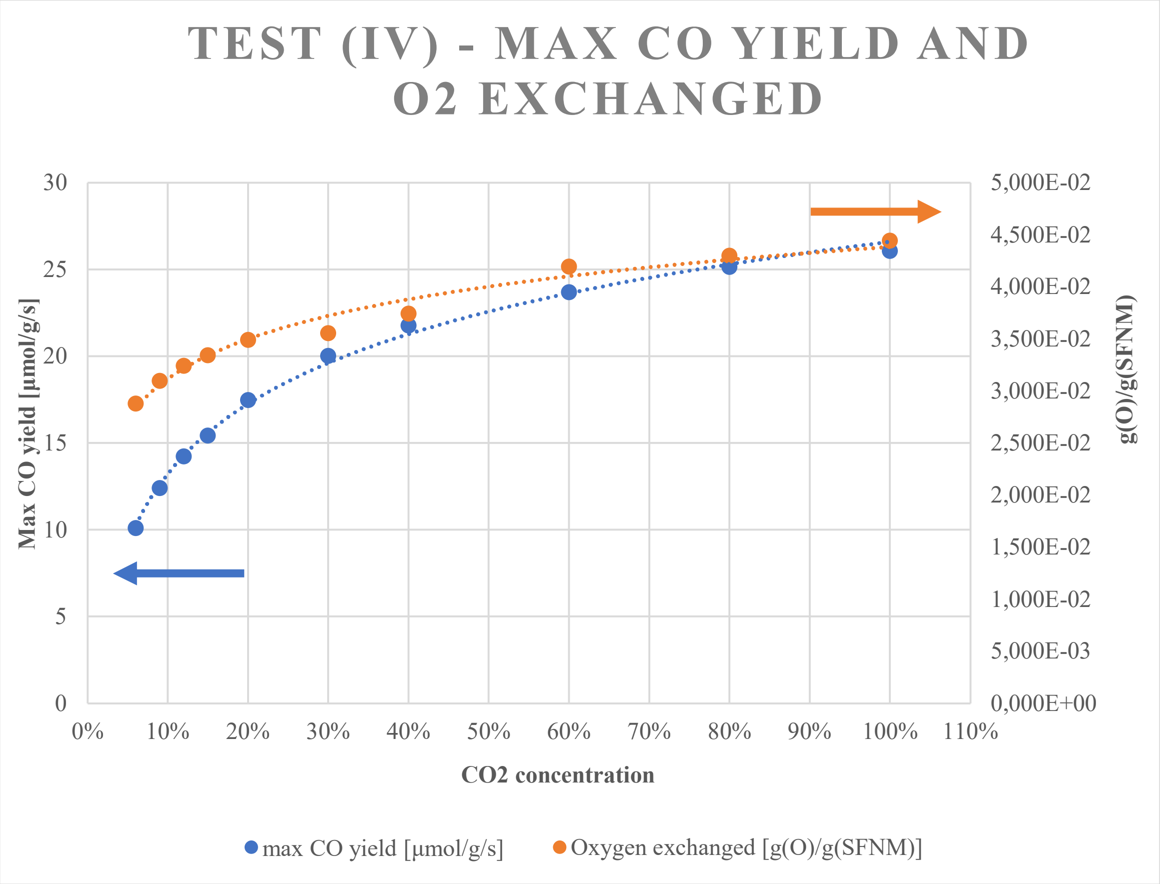

***Figure 4.10**: Maximum CO yield (left-y axis) and Oxygen Exchanged (right-y axis) as function of CO_2 concentration for 850°C.*

When increasing the CO_2 concentration, the maximum CO yield and the oxygen exchange per grams of sample increase too because, ideally, when we set a higher concentration, the probability of carbon dioxide molecules to occupy the oxygen vacancies created during reduction is higher. Finally, we can observe that the two logarithmic curve presents a tendency to reach a plateau while arriving at high concentration levels, meaning that we are possibly approaching the completed oxidized condition of the sample. Indeed, it can be asserted that this oxidation level is never reached in the cycles performed, because in that case the global yield should remain constant while changing the CO_2 concentration. Further consideration and tests should be carried on in order to verify this hypothesis.

4.5 TEST (V): Variation of CO_2 content in non - isothermal cycles - 10 cycles

This test is the last focused on the oxidation study. It is very similar to TEST (IV), but this time the temperature of each reduction and correspondent oxidation are not equal, thus cycles are non-isothermal. Indeed, the reduction temperature is kept at 850°C for each of the ten cycles, while the oxidation one is 750°C. The investigated range of CO_2 concentration is the same of the previous cycles: 6-100% of CO_2/N_2, while a 10% H_2/N_2 content is again used in reduction. The step duration for the oxidation is still 30 min, while for the reduction is 60 min. Since the two steps are performed at different temperature, the purging 100% N_2 step in the middle match with the requested temperature ramp up or down. In the following the results of the simulation are reported, both in graphical and numerical way.

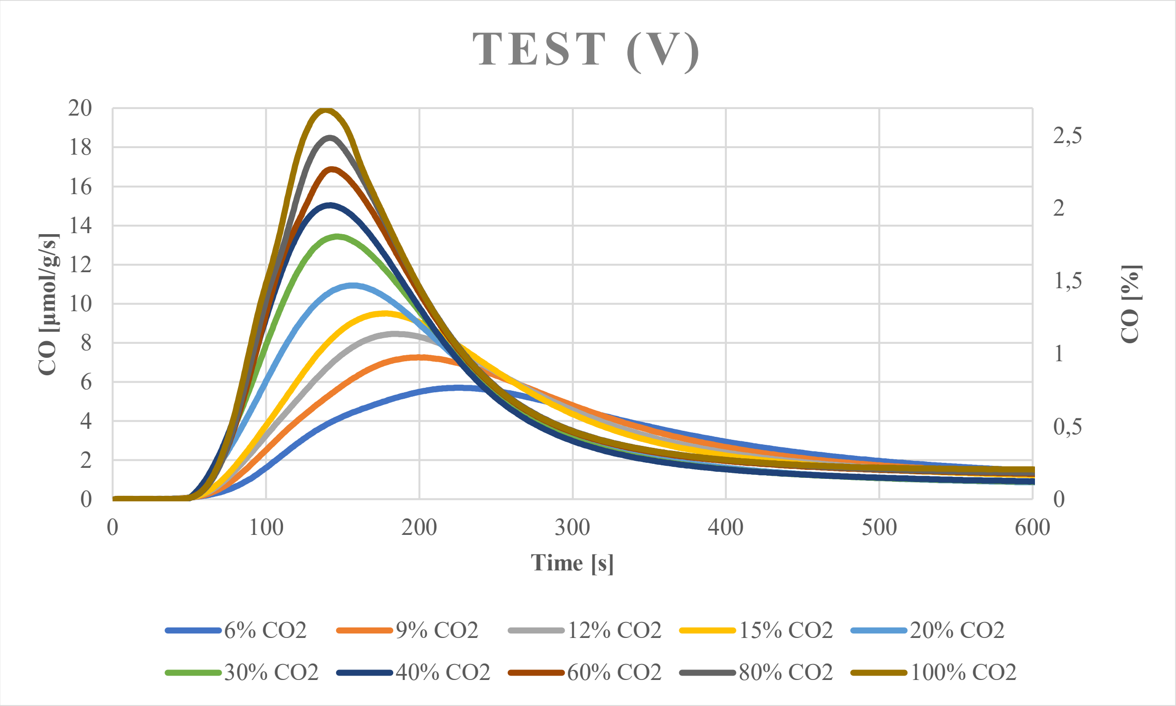

***Figure 4.11**: CO Production of TEST (V).*

***Table 8**: Results for each redox cycle of TEST (IV).*

N° Cycle	CO_2 **Content [%]**	CO **yield** $[\mu mol/g]$	**Max** CO **yield** $[\mu mol/g]$	$g(O)/g(SFNM)$ $[g_O/g_{SFNM}] \cdot 10^{-2}$	$g(CO)/g(SFNM)$ $[g_{CO}/g_{SFNM}] \cdot 10^{-2}$
1	6	1778	5.49	2.85	4.98
2	9	1760	6.98	2.82	4.93
3	12	1793	8.16	2.87	5.02
4	15	1862	9.22	2.98	5.21
5	20	1862	10.68	2.98	5.21
6	30	2070	13.17	3.31	5.80
7	40	2160	14.76	3.46	6.05
8	60	2375	16.58	3.80	6.65
9	80	2448	18.15	3.92	6.85
10	100	2413	19.47	3.86	6.76

As expected from the results of previous tests, also in this case the redox performance of the material improves while increasing the CO_2 content, leading to a faster kinetics and so to narrower curves. By the analysis of these data, it can be observed that the values obtained fit exactly between the first ones from the TEST (IV), where the cycles were set at 750°C, and the last ten, when the temperature chosen was 850°C. Indeed, the maximum peak in this case arrives at values of CO of 19.47 $[\mu mol/g \cdot s]$ for a pure carbon dioxide oxidizing flux, which stays between the 17 $[\mu mol/g \cdot s]$ of the first TEST (IV) stage and the 26 $[\mu mol/g \cdot s]$ of the others, both corresponding to the same level of CO_2. The same situation stands for all the other curves at lower concentrations. These results are expected. A higher reduction temperature promotes the oxygen vacancies creation mechanism and so the final CO production will be higher, since there is more place free to be occupied. However, the temperature swing inside the cycles adds some complexity for the system, and moreover it can create stability problem in the gas analyser readings: so, generally, isothermal cycles are preferred. In Figure 4.12 the co-dependency between the maximum CO yield in ($[\mu mol/g \cdot s]$) and the mass of exchanged oxygen and the CO_2 content is again reported.

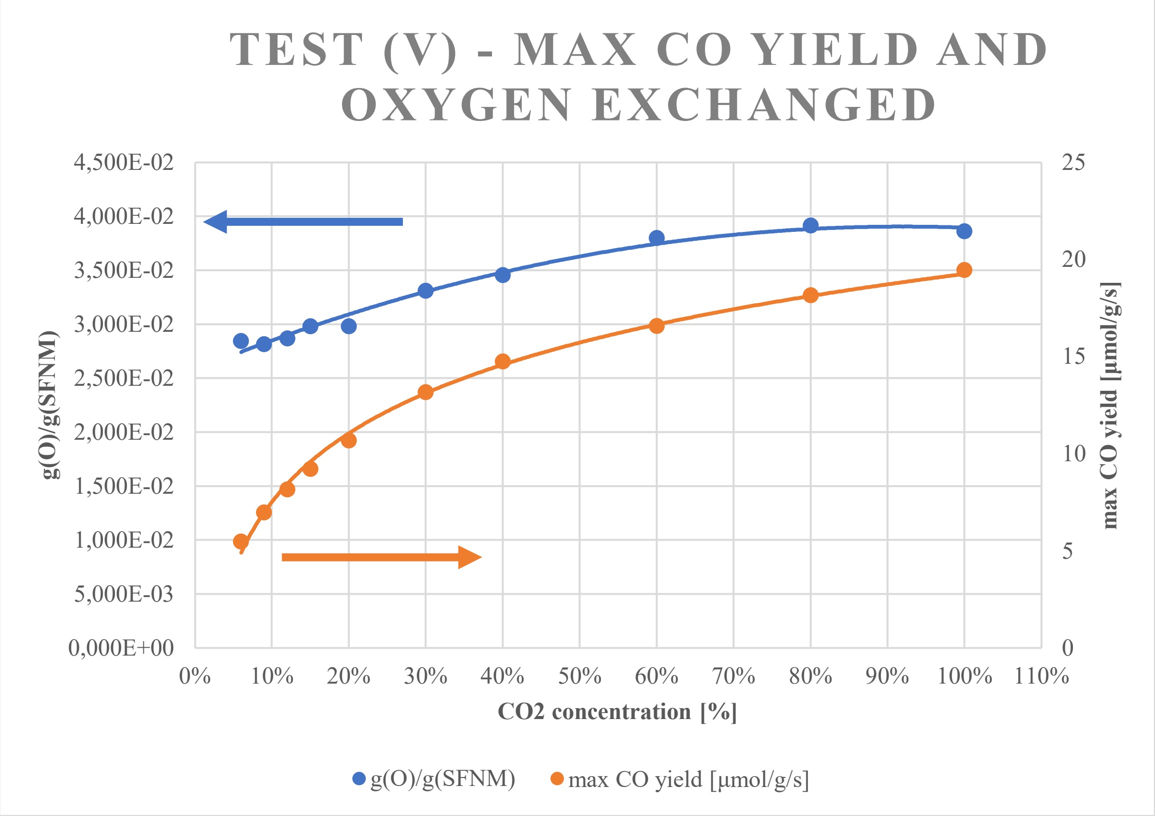

***Figure 4.12**: Maximum CO yield (left-y axis) and Oxygen Exchanged (right-y axis) plotted as function of the CO_2 concentration for TEST (V).*

In this case, as the previous test, a logarithmic trend of the two curves can be observed, confirming results consistency. With TEST (V), the investigation of SFNM-04 material redox ability is concluded. We can state that both reduction and oxidation temperatures are very important parameters for the rendering of the material, and the same is valid for the CO_2 content in the oxidizing flux. Furthermore, it can be observed that the test performed up to this point contains 46 redox cycles and a change in material response is never experienced. So, we can establish again the good stability and repeatability of the SFNM-04 double perovskite.

4.6 TEST (VI): Variation of the reduction temperatures – 5 cycles

With TEST (VI) the investigation about the reduction step starts. In this test 5 cycles are performed keeping constant oxidation conditions (850°C and 20% CO_2/N_2) and H_2 concentration (10% H_2/N_2); the reduction temperatures are distributed in this way: the first and the last cycles are performed at 850 °C to verify the data repeatability, while the others at 550-650-750 °C respectively. No change in the duration of the step is made for both oxidation and reduction. As for the other tests in which there was a temperature swing inside the simulation, all the purging steps with 100% N_2 follow the temperature program of the furnace, with ramps up of 10 K/min and ramps down of 6K/min; the only exception is the first ramp up that brings the temperature of the microreactor until 500 °C by 20 K/min (air pre-treatment step). The graphical and analytical results are reported in the following.

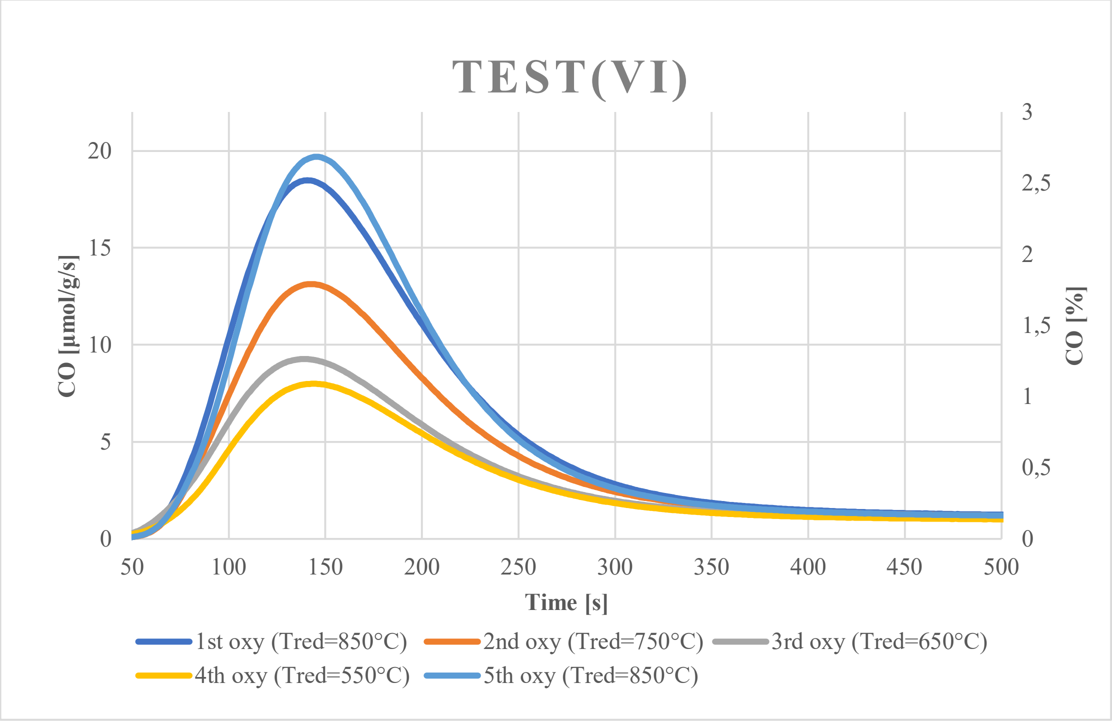

Figure 4.13: *CO Production of TEST (VI).*

***Table 9**: Results for each redox cycle of TEST (VI).*

N° Cycle	T_{RED} $[°C]$	CO **yield** $[\mu mol/g]$	**Max** CO **[%]**	CO_2 **conversion [%]**	$g(O)/g(SFNM)$ $[g_O/g_{SFNM}] \cdot 10^{-2}$	$g(CO)/g(SFNM)$ $[g_{CO}/g_{SFNM}] \cdot 10^{-2}$
1	850	2304	2.48	12.42	3.69	6.45
2	750	1725	1.77	8.83	2.76	4.83
3	650	1277	1.25	6.23	2.04	3.57
4	550	1116	1.08	5.38	1.79	3.12
5	850	2360	2.69	13.43	3.78	6.61

The first and the last cycles once again confirm the repeatability of the material (the curves are almost overlapped, and the numerical results are similar too). Concerning the variation of the reduction parameters we can make the same statement already found for oxidation: a higher reduction temperature brings to a bigger final CO production, since temperature promotes the vacancies creation. The obtained curves are very similar to ones from TEST (II), but a difference can be noted in the peaks shape. Indeed, in this case the oxidation steps remain at the same temperature and so the kinetics of the reaction is not affected: that's why all the curves in this test present a peak in the same time interval (about 300 s), with a similar width. Again, the max CO production is obtained at the maximum temperature and correspond to a peak of 19 $[\mu mol/g \cdot s]$. Regarding the lowest temperature test instead, the CO production reached is 1116 $[\mu mol/g]$, which is higher in comparison to the specular condition with 550°C oxidation temperature (825 $[\mu mol/g]$). This difference may be explained by the fact that a lower temperature affects more the reduction activity than the oxidation one: indeed, in TEST (VI) a value of 5.38 % of CO_2 conversion is reached, while in TEST (II) it was almost two times lower (2.25 %). By reducing the reduction temperature, the oxygen vacancies creation is penalized and so also the CO produced in the following step decrease. Furthermore, a low temperature during reaction doesn't allow the formation of the ex-solution phenomena of Fe and Ni cations, limiting the redox activity of the material.

4.7 TEST (VII): Variation of the hydrogen content – 18 cycles

This test contains the specular simulation of TEST (IV): this time the sample response to the variation of hydrogen content is analysed, by changing its concentration in the range 5-100% H_2/N_2. A smaller percentage of hydrogen couldn't be created because it's the minimum quantity that the MFC could send using a total flux of 200 NmL/min. This simulation is divided again in two stages: the first one corresponds to 9 cycles with different concentration and constant temperature (isothermal cycles) of 750°C; the second stage is equal, but at 850°C. After the first oxidation in air at 500°C, the redox cycles start and each one is composed by the two purging steps with 100 %N_2, a 60 min reduction and a 30 min oxidation (with constant CO_2 content at 20%/N_2). The graphical and numerical results of the first stage are now reported.

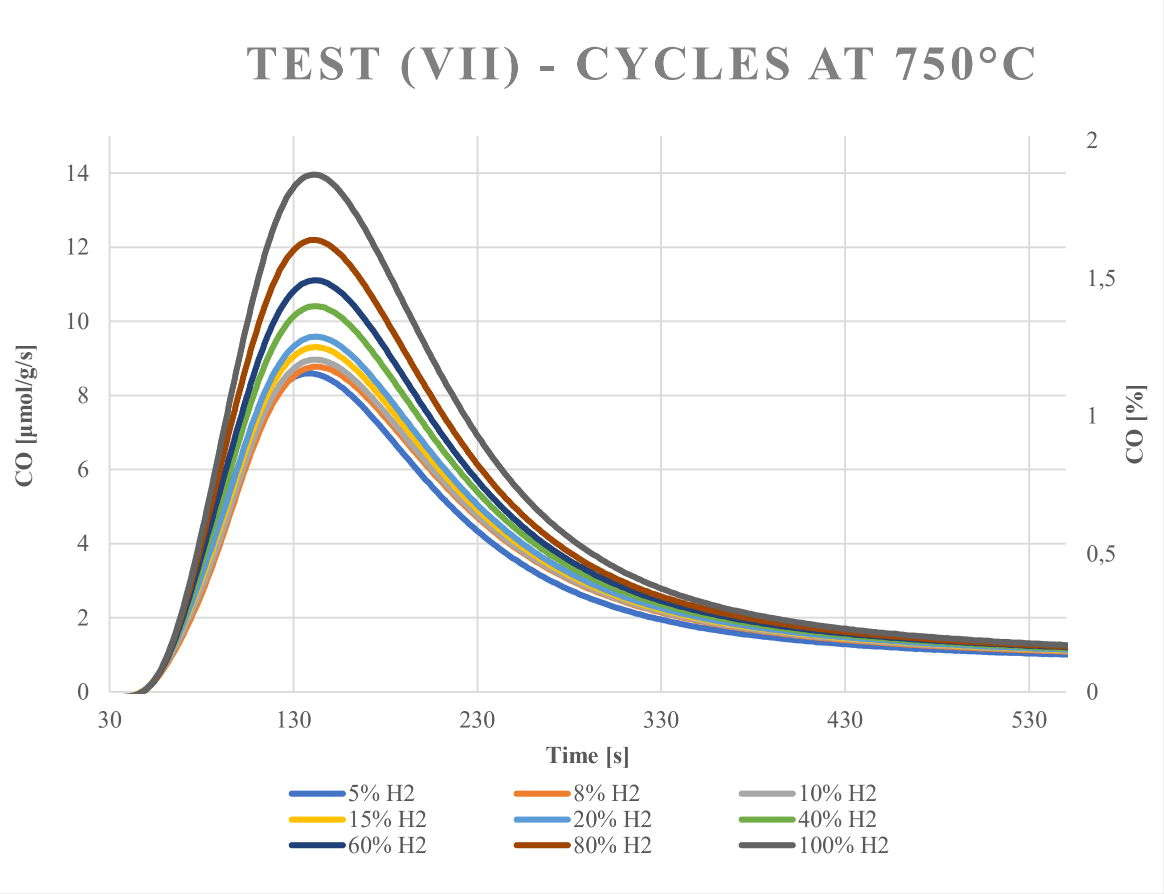

Figure 4.14*: CO Production of TEST (VII) for the first stage at 750°C.*

***Table 10**: Results for each redox cycle of TEST (VII) performed at T=750 °C.*

N° Cycle	H_2 Content [%]	CO yield [$\mu mol/g$]	Max CO [%]	CO_2 conversion [%]
1	5	1396	1.16	5.78
2	8	1434	1.18	5.90
3	10	1458	1.21	6.03
4	15	1514	1.25	6.26
5	20	1558	1.29	6.44
6	40	1688	1.40	7.00
7	60	1790	1.49	7.47
8	80	1944	1.64	8.20
9	100	2190	1.88	9.38

The results show that increasing the hydrogen concentration in the reducing gas mixture brings to a higher CO production. This result was expected: a higher concentration of the reductive agent in the reduction step brings to a further release of oxygen from the material lattice and so to the creation of more oxygen vacancies that can be occupied lately from the CO_2 molecules. Moreover, ex solution phenomenon is also enhanced when the content of hydrogen is higher, leading to a further increase of the SFNM-04 performance. Analysing these curves, we can also observe an increase of the distance between each curve at higher H_2 concentration. It must be noticed that the same situation didn't happen in TEST (IV) when the CO_2 content in oxidation increased: the difference between each curve was higher, but this distance was homogenously distributed for each curve. Another difference between the two simulations (TEST(VII) and TEST (IV)) can be found from a kinetic point of view: clearly the change in hydrogen composition doesn't affect the kinetic as it was for the variation in the CO_2 content of the previous test, where the peaks showed a shrinkage through the left (proof of a faster kinetic). Instead, in this case, all the peaks come after the same time intervals (about 150s). So, it can be stated that an increase of the CO_2 concentration in the oxidation step is more effective than changing the hydrogen in reduction. The maximum CO yield is obtained as expected with 100%H_2 and is 2190

$[\mu mol/g]$, corresponding to a volume of 1.88%. Comparing Table 11 with the one from TEST(IV) (Table 6) it can be confirmed what is showed by the curves: in this simulation the difference between the CO peak value at 5% H_2/N_2 and 100%H_2 is 5.36 $[\mu mol/g \cdot s]$, while in TEST(IV) the global difference was about 13.98 $[\mu mol/g \cdot s]$ varying from 6% CO_2/N_2 to pure CO_2. This big variation in the final production is explained by the fact the CO_2 content directly affects the CO forming in the oxidation step and so brings a higher impact in the result. The hydrogen content, instead, affects indirectly the CO_2 production, because is responsible for the number of oxygen vacancies created: of course, if this number is higher, the probability of combination between a CO_2 molecule and the vacancy is higher too, and the production will be higher; however, the entity of the benefit is lower than the direct influence of a bigger partial pressure gradient in the oxidation step. Another detail worthy to analyse is the similarity between the CO global yield and CO_2 conversion of the cycle with 100 % H_2 and the ones obtained in the reference test (TEST (I)). This put more attention on the fact that, even if the H_2 concentration change from 10% to 100% (keeping constant the CO_2 content), the parameter with higher impact remains the temperature. Indeed, at 750°C and 100% H_2 the CO_2 converted is 9.38%, while in the reference test at 850°C and 10% H_2/N_2 was almost 12%. In the following, the curves showing the trend of CO maximum production rate and CO_2 converted as function of H_2 content are reported.

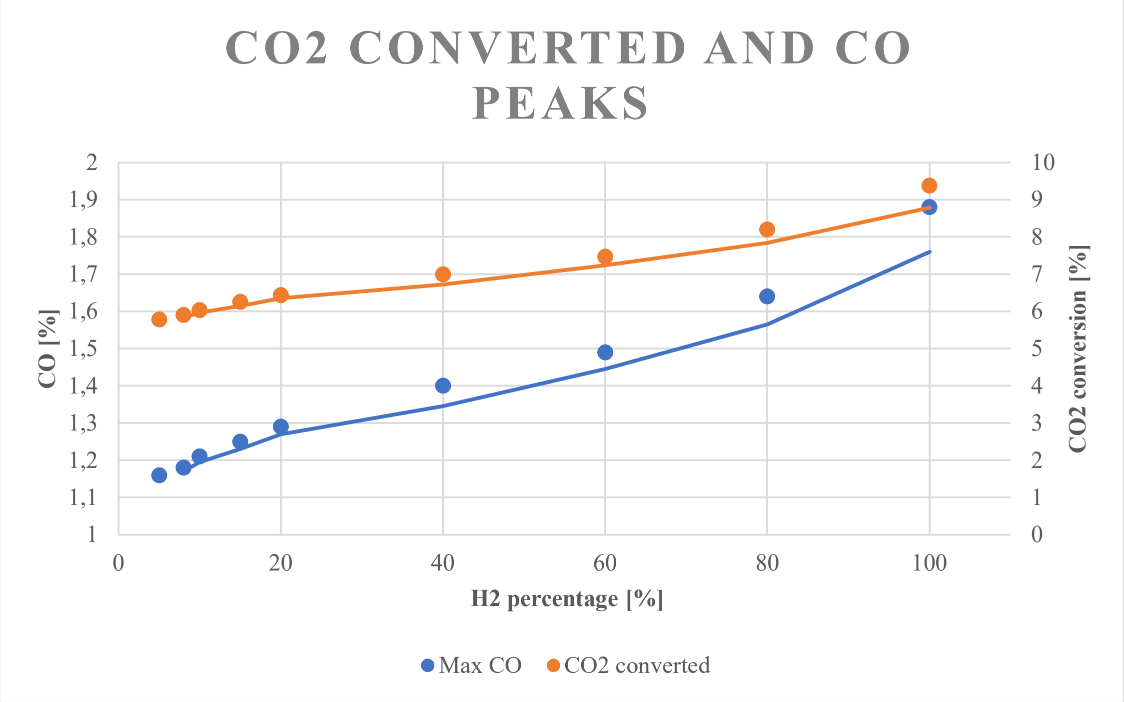

***Figure 4.15**: Maximum CO yield (left-y axis) and CO_2 converted (right-y axis) plotted as function of the H_2 concentration for the first nine cycles.*

We can observe that in this case the behaviour isn't logarithmic anymore, without presenting the final plateau at high concentrations; indeed, in this case the increase of y-axis values is continuous, almost linear, for the entire concentration range. This is probably caused by the indirect role that H_2 content has in the CO production mechanism. Now the graphical and numerical results for the last nine cycles are reported (second stage of the simulation at 850°C). This stage is the perfect copy of the previous one, but this time the H_2 content is changed for 850°C cycles.

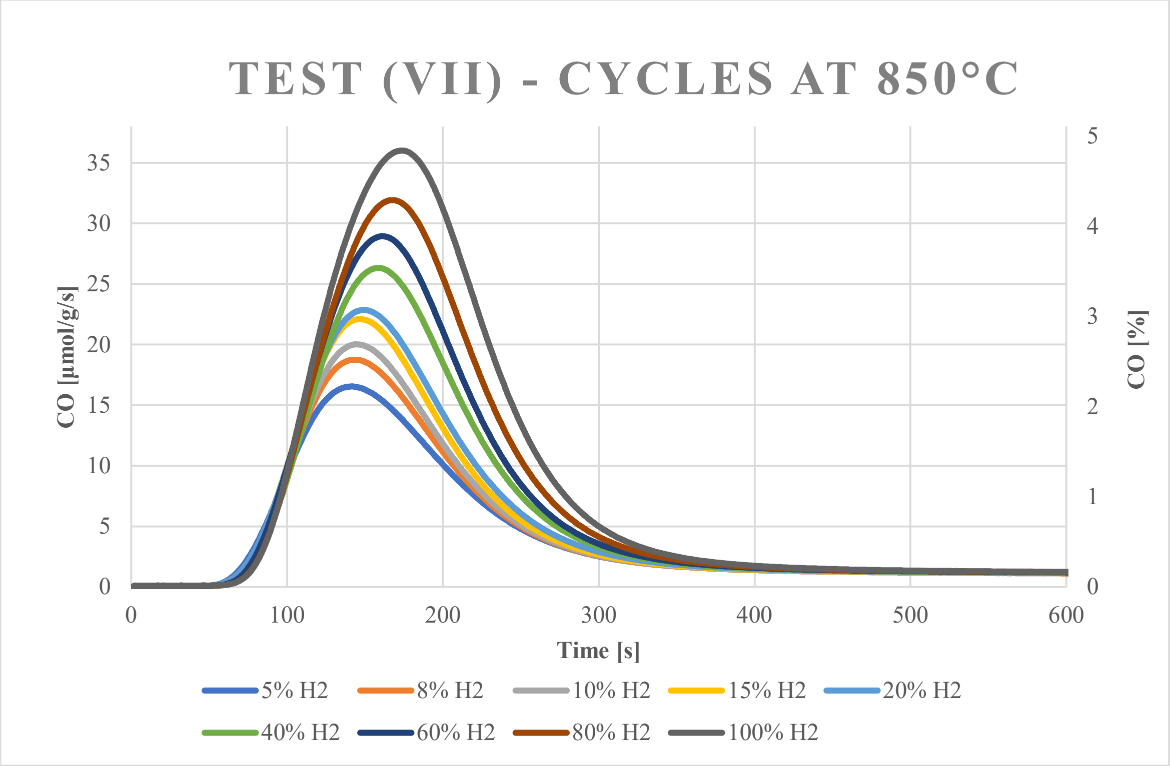

Figure 4.16: *CO Production of TEST (VII) for the second stage at 850°C.*

Table 11: *Results for each redox cycle of TEST (VII) performed at T=850°C.*

N° Cycle	H_2 **Content [%]**	CO **yield** $[\mu mol/g]$	**Max** CO **[%]**	CO_2 **conversion [%]**
1	5	2068	2.22	11.12
2	8	2252	2.52	12.61
3	10	2364	2.69	13.46
4	15	2583	2.97	14.86
5	20	2714	3.07	15.36
6	40	3123	3.54	17.70
7	60	3469	3.89	19.45
8	80	3884	4.29	21.45
9	100	4524	4.84	24.20

Also in this configuration, the increase of H_2 concentration leads to a bigger CO production. However, when performing the cycles at higher temperature the kinetics result changed: in this case, the CO peaks don't occur at the same instant but shift towards the right when H_2 concentration increases, suggesting a variation of the kinetics. In Table 13, the numerical results in terms of CO yield, maximum CO produced, and CO_2 converted are reported, both for 750°C and 850° stages. The cycle performed at 850°C and the 100% H_2 shows the highest CO yield found until now: 4524 $[\mu mol/g]$. In order to give a better comparison of this test and TEST(IV), in Table 14 are also reported the same quantities but of the oldest test.

***Table 12**: Comparison of CO yield and maximum CO yield of the first stage performed at T=750 °C and second stage at T=850 °C of TEST (VII).*

		$T = 750\,°C$		$T = 850\,°C$	
N° Cycle	**H_2 Content** [%]	**CO yield** $[\mu mol/g]$	**Max CO yield** $[\mu mol/g \cdot s]$	**CO yield** $[\mu mol/g]$	**Max CO yield** $[\mu mol/g \cdot s]$
1	5	1396	8.60	2068	16.55
2	8	1434	8.78	2252	18.76
3	10	1458	8.97	2364	20.03
4	15	1514	9.31	2583	22.11
5	20	1558	9.59	2714	22.86
6	40	1688	10.41	3123	26.33
7	60	1790	11.11	3469	28.95
8	80	1944	12.20	3884	31.93
9	100	2190	13.96	4524	36.01

***Table 13**: Comparison of CO yield and maximum CO yield in of the first stage performed at T=750 °C and second stage at T=850 °C of TEST (IV).*

		$T = 750\,°C$		$T = 850\,°C$	
N° Cycle	**CO_2 Content [%]**	**CO yield [μmol/g]**	**Max CO yield [μmol/g · s]**	**CO yield [μmol/g]**	**Max CO yield [μmol/g · s]**
1	6	1115	4.85	1800	10.11
2	9	1118	5.35	1937	12.42
3	12	1139	5.95	2027	14.24
4	15	1194	7.29	2090	15.45
5	20	1500	9.36	2183	17.49
6	30	1723	11.29	2224	20.04
7	40	1895	12.62	2341	21.78
8	60	2111	14.59	2622	23.70
9	80	2158	16.06	2689	25.16
10	100	2270	17.25	2778	26.08

Firstly, concerning results at 850°C, the first thing we can observe is the difference in terms of global CO yield and maximum CO production: by using a reducing mixture at 100% H_2 and a oxidating one at 20%CO_2/N_2, it is reached 4524 $[\mu mol/g]$ as global CO yield and 36.01 $[\mu mol/g \cdot s]$ as maximum CO production value, while when the hydrogen concentration in 10%/N_2 and the carbon dioxide is at 100% these values become 2278 $[\mu mol/g]$ and 26.08 $[\mu mol/g \cdot s]$ respectively. This difference in production can't be neglected and it means that when the temperature is fixed at 850°C, the increase of the hydrogen content in the reduction step leads to a higher production rate in comparison to the increase of CO_2 concentration in oxidation. However, when the temperature is at 750°C this difference is less marked (values are similar in the two cases). This evaluation confirms the fact that temperature is the predominant parameter for the redox performance of this material and by enhancing reduction phase parameters and reducing the SFNM-04 sample, the highest production rates (until now) can be reached. In conclusion, it can be stated that varying both the oxidation and reduction parameters the final production can be improved, but the first case is limited if compared to the results of the second. Certainly, the optimization process to find the highest CO production is a tradeoff and so the combination of the best reductive and oxidative conditions. In Figure 4.17, the maximum CO produced, and CO_2 converted as function of H_2 concentration are plotted, this time for the second stage at 850°C. In this case a stronger linearity of the curves can be noticed and, differently from the first stage, the lines increase monotonically.

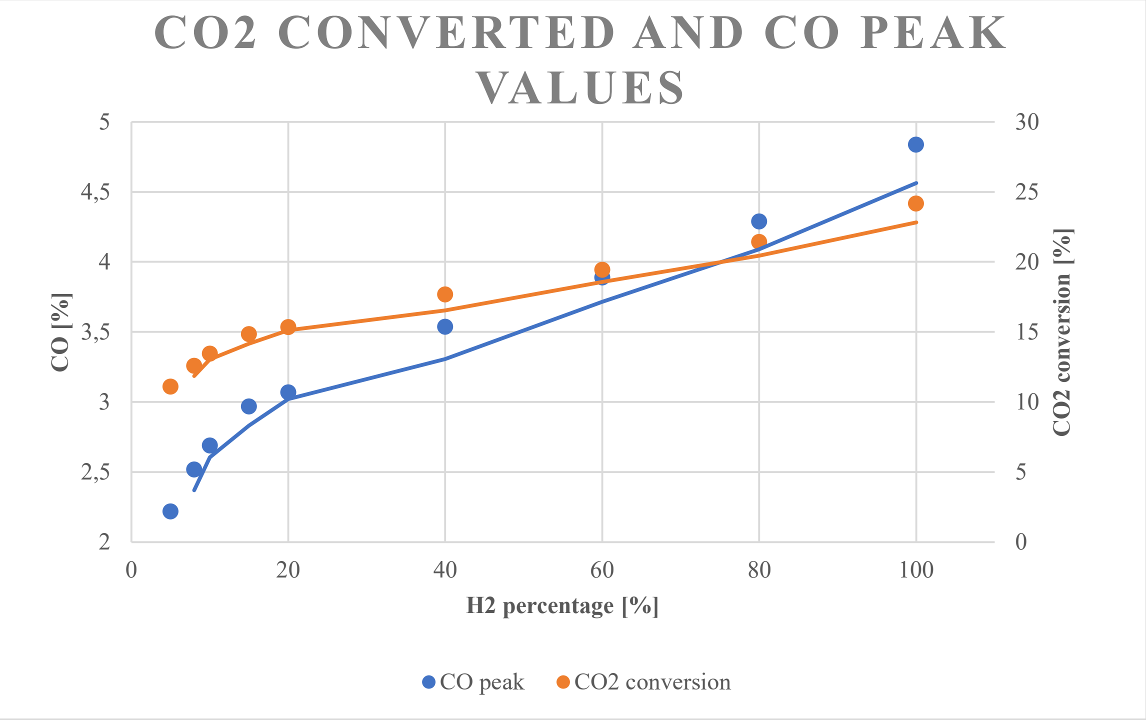

Figure 4.17: *Maximum CO yield (left-y axis) and CO_2 converted (right-y axis) plotted as function of the H_2 concentration for the second stage at 850°C.*

The two curves follow almost the same identical trend, and the maximum resulted conversion of CO_2 is about 24.2 %, more than twice the value of the previous stage. The fact that these curves never reach a plateau means that we never reach (or approach to) the total reduction condition of the sample. Indeed, as it was assessed for the oxidation (TEST(IV)), if the material is fully reduced, the CO global yield should not vary as function of the H_2 concentration. Again, this statement remains a hypothesis since its demonstration is difficult to verify and depends on the reliability of the measured data.

4.8 TEST (VIII): Variation of H_2 content in non - isothermal cycles – 9 cycles

This test is the correspondent of TEST (V), where non-isothermal cycles are performed for each different concentration of hydrogen. In particular, the H_2 content range is varied from 5% to 100%, the temperature of reduction is 850°C and the oxidation temperature is 750°C. As the previous tests, the purging steps are again linked to the temperature program, which use the same ramps (up and down) used until now. The oxidation step last 15 min with 20% CO_2/N_2, while each reduction has a duration of 1 hour. Again, the pretreatment in air is performed at 500°C in order to delete eventual contaminants and to guarantee an oxidized sample before starting the simulation. The graphical and numerical results are reported in the following.

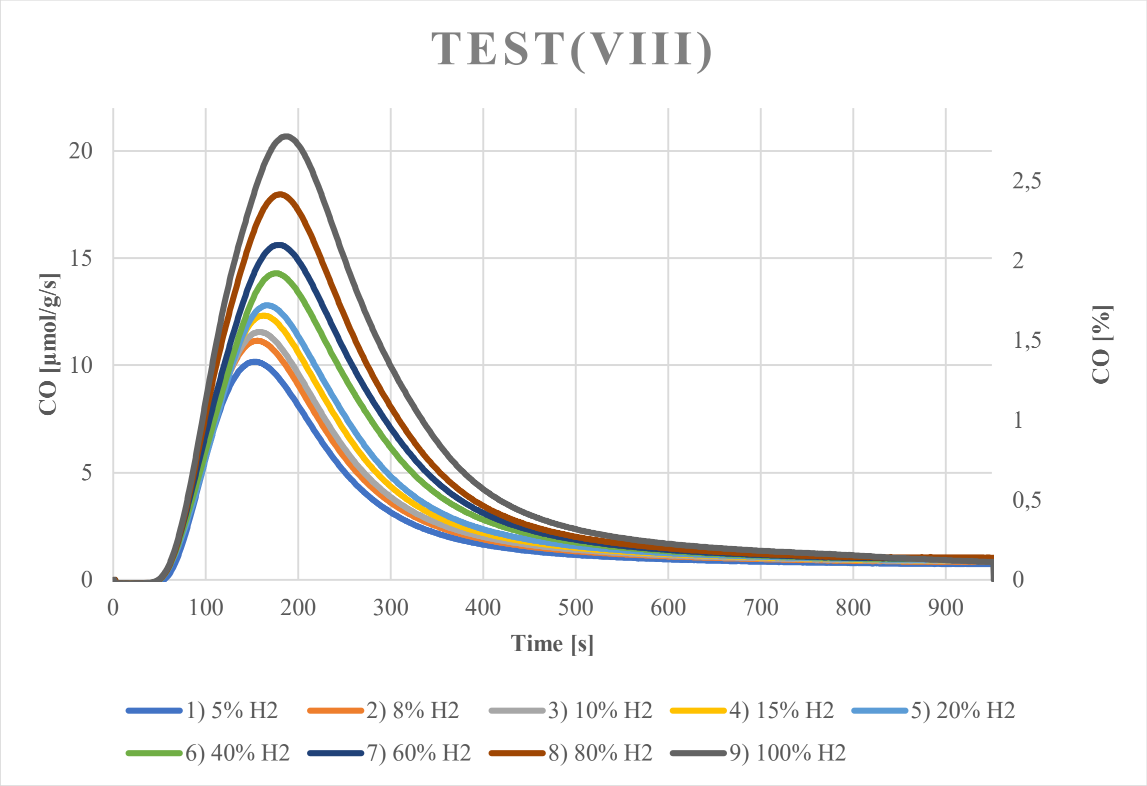

Figure 4.18*: CO Production of TEST (VIII).*

***Table 14**: Results for each redox cycle of TEST (VIII).*

N° Cycle	H_2 **Content [%]**	CO **yield** $[\mu mol/g]$	**Max** CO **[%]**	**Max** CO **yield** $[\mu mol/g \cdot s]$	CO_2 **conversion [%]**
1	5	1739	1.37	10.18	6.84
2	8	1916	1.50	11.16	7.50
3	10	1995	1.55	11.56	7.77
4	15	2157	1.66	12.33	8.29
5	20	2286	1.72	12.80	8.60
6	40	2667	1.92	14.30	9.61
7	60	2982	2.10	15.63	10.50
8	80	3424	2.42	17.98	12.09
9	100	4034	2.78	20.69	13.90

While the H_2 content increases, the CO production rate increases too, as expected. From the comparison of these values with those found in TEST(V), we can see similar CO peaks values but, however, the global yield results higher in this case, slightly when the H_2 concentrations are low, remarkably when the H_2 content is high. The maximum CO production reached in this test is 20.69 $[\mu mol/g \cdot s]$ for 100% H_2 concentration and 20% CO_2/N_2, while it was found 19.47 $[\mu mol/g \cdot s]$for 10 H_2/N_2 and 100%CO_2 conditions; the correspondent values of the global CO yield are 4034$[\mu mol/g]$ and 2413$[\mu mol/g]$. The significant difference between these values, together to a similarity in the maximum CO peaks, indicates that the variation of hydrogen content presents again a predominant role in comparison to the CO_2 one. The kinetics shows similar behaviour to the one found in TEST (V), with a global difference in the CO peak of 10.51 $[\mu mol/g \cdot s]$ (in the previous test the difference was of 13.98 $[\mu mol/g \cdot s]$ passing from 6%CO_2/N_2 to 100%). Another interesting point of view can be found by comparing these results with ones from TEST (VII), whose cycles are isothermal.

- TEST (VIII), non-isothermal conditions with 750°C as oxidation temperature and 850°C for reduction: the global CO yield reached is 1739 $[\mu mol/g]$ and maximum CO production of 10.18 $[\mu mol/g \cdot s]$ (when the reducing environment contain 5%

H_2/N_2), while the global CO yield reached is 4034 $[\mu mol/g]$ and maximum CO production of 20.69 $[\mu mol/g \cdot s]$ for 100% H_2 content;

- TEST (VII), second stage, isothermal conditions at 850°C: 2068 $[\mu mol/g]$ and 16.55 $[\mu mol/g \cdot s]$ are the results for 5% of hydrogen, while 4524 $[\mu mol/g]$ and 36.01 $[\mu mol/g \cdot s]$ when using a 100% concentration.

Therefore, TEST (VIII) establishes again that it is better to operate in isothermal condition with respect to the non-isothermal one. But at the same time, observing the results obtained during the second stage of TEST (IV) performed in isothermal conditions (850 °C) with a CO_2 content of 100 %, it noticed that TEST (VIII) presents significantly higher values even if in this configuration the oxidation temperature is lower (750 °C) and there is a lower CO_2 concentration in the gas oxidizing flow. More precisely, comparing these results listed in *Table 15* and those summarized in *Table 7*:

- During the second stage of TEST (IV) performed in isothermal conditions at 850°C, with a CO_2 content of 100 % of the gas oxidizing flow during the oxidation step, and using a reducing gas flow composed by 10 % H_2/N_2 during the reduction step, it is reached a CO yield of 2778 $[\mu mol/g]$ and a CO_2 conversion rate of 3.57 %.
- Differently, during TEST (VIII) performed in non-isothermal conditions (oxidation at 750°C and reduction at 850°C), with an oxidizing gas mixture composed by 20 % CO_2/N_2 and a reducing gas mixture of 100 % of H_2, it is achieved a global CO yield of 4034 $[\mu mol/g]$ and a CO_2 conversion rate of 13.90 %.

This difference explains that, at low oxidation temperature and low CO_2 concentration, it is possible to increase the CO production significantly by promoting the reduction step, in order to enhance oxygen vacancies creation. Concerning the amount of CO_2 converted, we can observe that the maximum of this value is obtained during the reduction investigation; 24.20% of carbon dioxide conversion is reached while using a 100% H_2 reducing gas flow and 20%CO/N_2 as oxidizing gas, while during oxidation investigation a maximum of 23.43% is obtained in TEST(IV) using 6% CO_2/N_2 as oxidizing mixture and 10% H_2/N_2 as reducing one. The meaning of this result is that, keeping the temperature and duration parameter equal, higher CO_2 conversion rates can be reached enhancing the reduction phase rather than acting on the oxidation parameters.

With TEST (VIII) the SFNM-04 behaviour investigation varying reduction parameters is concluded. H_2 concentration in the reducing gas flow affects more the fuel production if compared to the control of the CO_2 content variation. At the same time, by changing the amount of hydrogen the reaction kinetics doesn't show any difference, since all the CO peaks rise at the same time and have the same duration; this is opposite to what found while investigating the CO_2 content variation, when a change in this parameter brought to a faster CO production, with the peaks moving towards left as the carbon dioxide in the oxidizing flow was growing. So, it is possible to state that the reaction kinetic is surely affected by a variation in the CO_2 concentration and produce an acceleration in the fuel production when its content is increased; on the other side, changing the reduction step doesn't seem to influence the kinetic, since all the peaks grows together. However, in this last case, curves width grows and this is an indication of the effect that reduction has on the material: when performing a cycle using a more reductive environment (hence, more hydrogen content in the reducing flow), the number of created oxygen vacancy increases and then, during reduction, the time needed by the CO_2 molecules to occupy all the free sites will be higher (since there are more of them) and the final fuel production will present an increment too.

After the study of SFNM-04 redox performances at the variation of reduction and oxidizing parameters, an evaluation of possible effect of the step duration on the CO production is performed in the final two tests, namely TEST (IX) and TEST (X). The needing of such evaluation will be better explained in the next paragraphs.

4.9 TEST (IX): Variation of reduction times – 6 cycles

This test is performed in isothermal conditions at 850°C and with the reference concentrations for both reduction and oxidation: 10% H_2/N_2 and 20% CO_2/N_2. The difference with the TEST (I) consists in the variation of the time of the reduction step: while in all the previous simulations the reduction time was set to 60 min, now it is changed within the range 15-120 min. The oxidation step is kept constant at 30 min. The choice of using reference conditions instead the one with the highest performance is because in this case a better evaluation of the role of the reduction time can be performed. The graphical and numerical results are reported in the following.

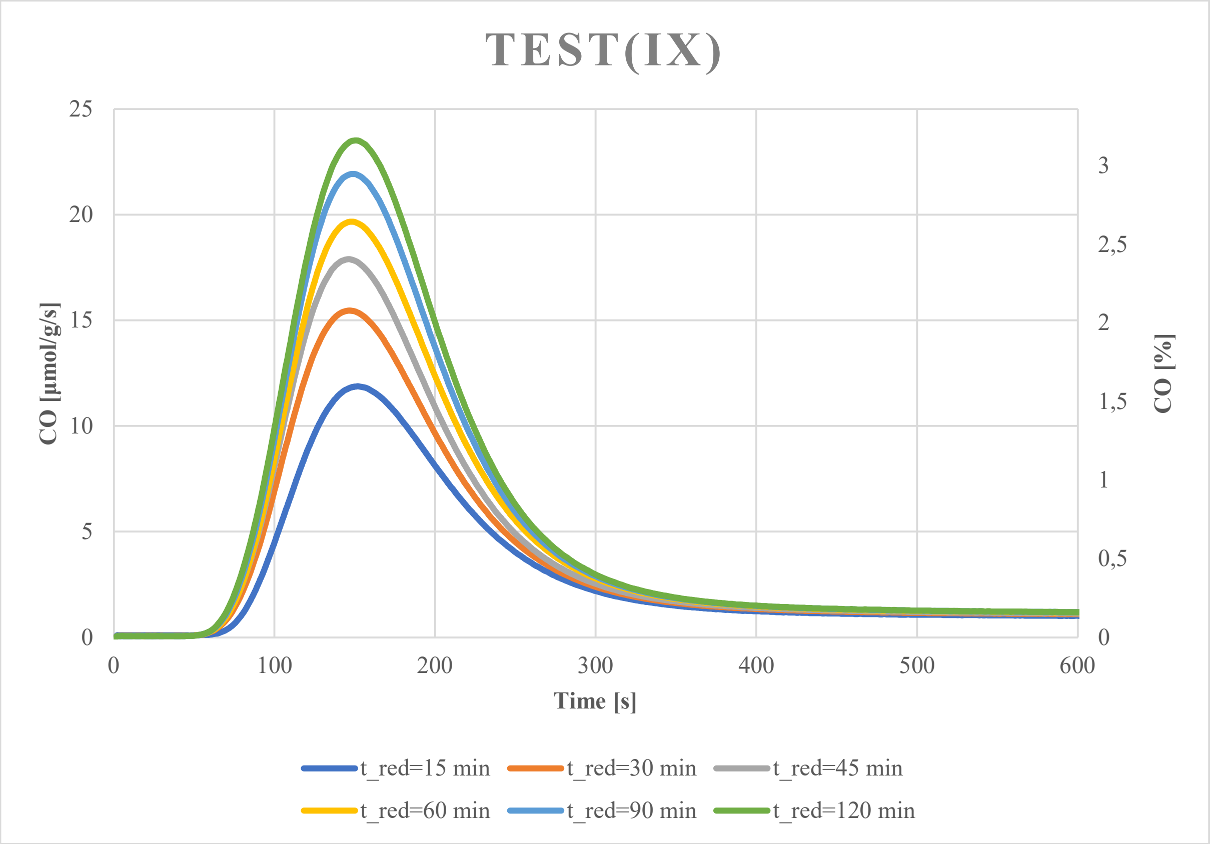

Figure 4.19: *CO Production of TEST (IX).*

Table 15: *Results for each redox cycle of TEST (IX).*

N° Cycle	t_{RED} [min]	CO yield $[\mu mol/g]$	Max CO [%]	CO_2 conversion [%]
1	15	1454	1.60	7.98
2	30	1864	2.08	10.39
3	45	2129	2.41	12.03
4	60	2356	2.64	13.22
5	90	2607	2.95	14.74
6	120	2793	3.16	15.80

Generally, the increase of reduction time brings to an increase of CO production, as expected. Indeed, if we maintain the hydrogen composition while increasing the time in which H_2 "sees" the sample, the molecules have the possibility to reach deeper parts of the lattice, and not just the surface of the material; ideally, with a very long reduction step, the entire perovskite structure could be reduced, because it is allowed the diffusion of the gas mixture in the whole bulk material and more oxygen vacancies are created. What we normally experience, instead, is a reduction that involves only the surface of the sample, where the reaction is promoted by ex-solution phenomena. So, the consequence of a higher reduction time is expected to be a higher fuel production since there is more place where CO_2 molecules can react. The results of this test confirm this concept: the lowest CO production is obtained with 15 min of reduction and correspond to a global CO yield of 1454 $[\mu mol/g]$, almost 60% lower than values found in the reference (60 min); the highest production is reached reducing for 120 min, resulting in 2793 $[\mu mol/g]$ as global CO yield, which represents 19% more than the reference. Analysing the CO peaks values and the rate of CO_2 conversion an equal response is detected (Figure 4.20).

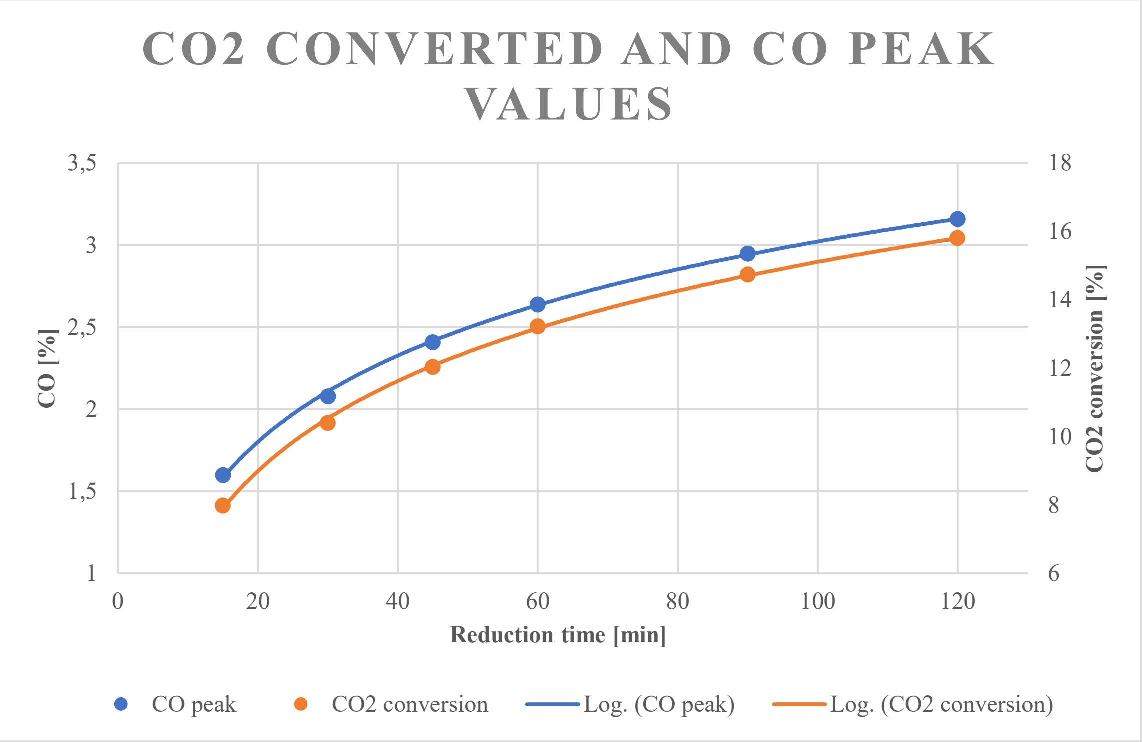

Figure 4.20*: Maximum CO yield (left-y axis) and CO2 converted (right-y axis) plotted as function of the reaction reduction time.*

It can be observed an almost linear behaviour in the first part of the plot (until 60 min), and then a tendency towards a plateau. The main goal of this simulation (with the variation of reduction time) is that in TEST (VII) the results was indicating that a fully reduced condition of the sample wasn't experienced even with 850°C and 100% H_2 in the reducing gas mixture: the third parameter analysable to reach this condition is the time. The resulting plot in Figure 4.10 clearly shows that even doubling the time of reduction, the material is not fully reduced yet. However, the trend is not fully linear but presents a plateau, indication of the fact that this condition is being reached. Further simulation should be carried on in the future to investigate better this topic, as example using the maximum reducing condition (850°C and 100 %H_2/N_2) and increasing the duration until the time variation doesn't affect anymore the CO production and CO_2 conversion. Since these conditions would be too extreme, a further study regarding the reduction time is not performed, but the next test is focused on analysing, starting from this condition, how much the CO production can increase if the sample is left in oxidizing environment for a lot of time.

4.10 TEST (X): 7 hours oxidation cycle – 1 cycle

The last test focuses on the investigation of the influence of the oxidation time in the fuel production of SFNM-04 perovskite. This simulation is composed by only 1 long cycle, where the sample is left in the oxidating environment for 7 hour (420 min), instead of the usual 30 min. The composition of the oxidizing and reducing gas flows are respectively 20% CO_2/N_2 and 100% H_2/N_2 and both steps are performed at constant temperature of 850°C. The reduction step lasts 120 min. Graphical results are reported in the following.

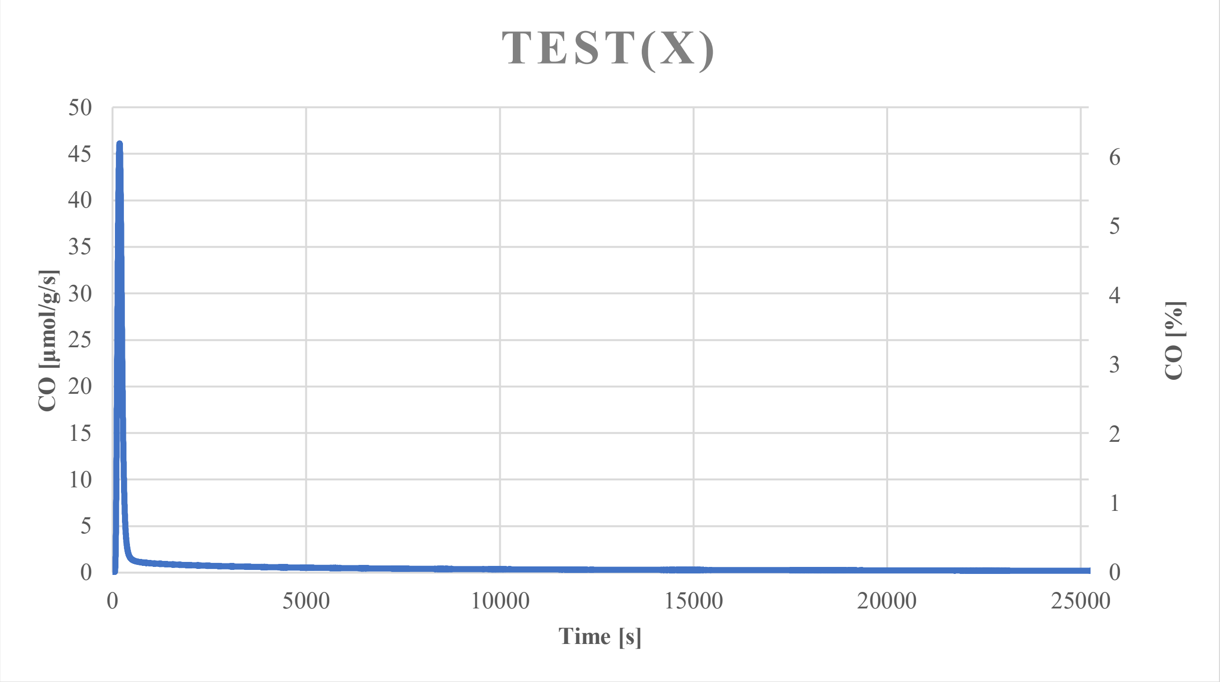

Figure 4.21: *CO Production of TEST (X).*

During this long oxidation step, CO_2 molecules have the possibility to occupy not only the oxygen vacancies in material surface, but also to arrive to the bulk of the perovskite lattice. The consequences of this phenomena are confirmed analyzing the results of this test. The highest CO production rate is obtained, with a peak of 46.13 $[\mu mol/g \cdot s]$ corresponding to a 6.20% of volume and to a CO_2 conversion rate that overcome the 30% (precisely 31%) value, which represent the highest result reached so far. The choice for the parameters of the test is due to the needing of trying to arrive at the maximum oxidation condition of the material, hence the upper limit in fuel production that could be experienced starting from the known condition of TEST(IX). The post processing of the data was challenging in this case, because require an investigation about the CO production values in proximity of the oxidation curve. Indeed, in this test the CO peak is reached after 150 s, but the following tail stabilizes at values which are higher than ones from previous peaks. A possible explanation of this situation could be found in an inaccuracy of the gas analyser or in a wrong reading of the instrument. Of course, these hypotheses can’t be confirmed. For a better analysis of the phenomena, a white test (hence a simulation without the sample inside the microreactor) is performed too, and the comparison between the two curves is reported in Figure 4.22.

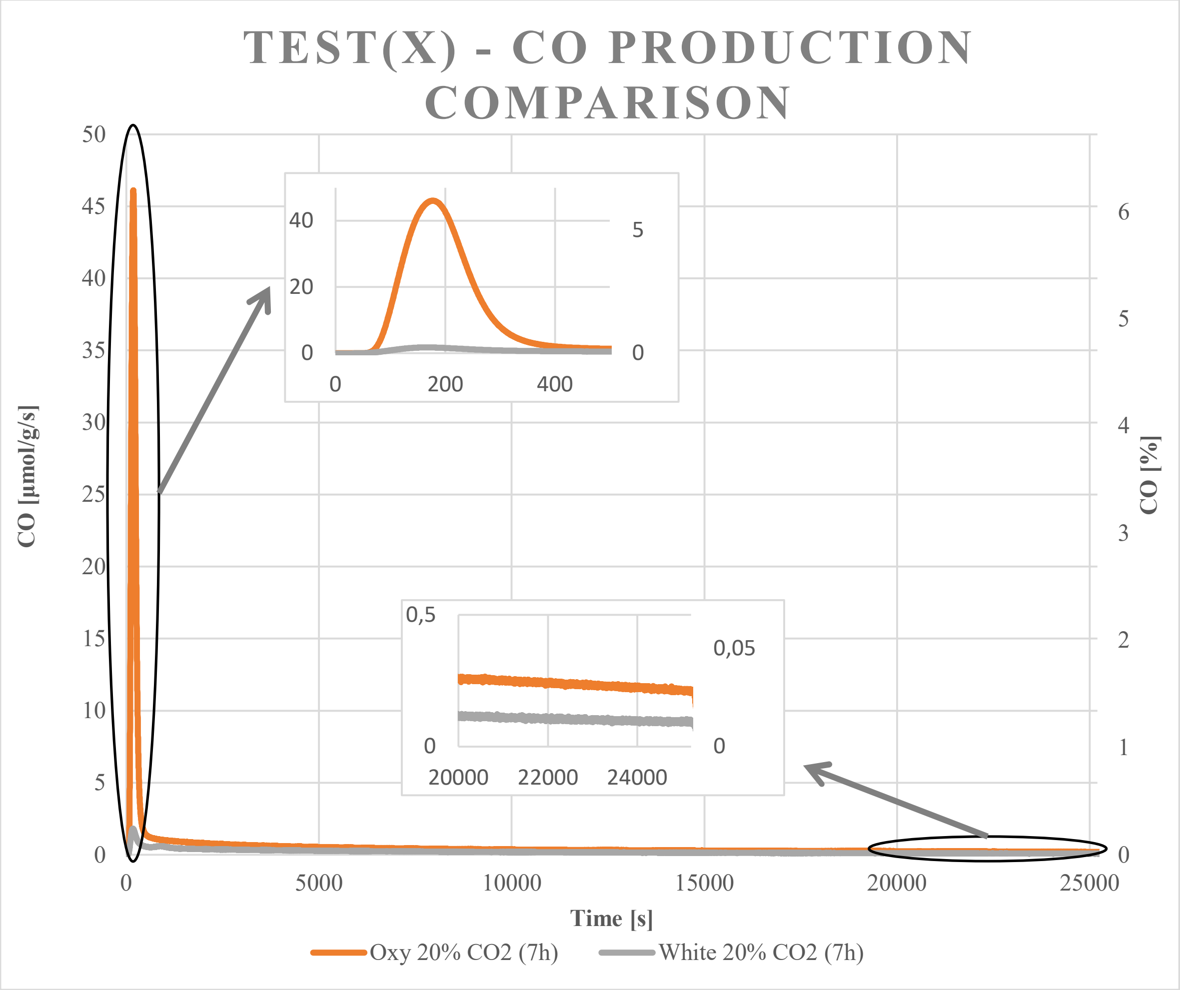

Figure 4.22: *CO Production of TEST (X) (yellow curve) compared with the CO Production of white test (blue curve).*

The grey curve correspond to the white test since there is the lower peak: the presence of this peak while no SFNM-04 sample is inserted in the reactor means that there is always an error due to the gas analyser, which temporarily misread the sent flux of CO_2 with the presence of CO molecules; however, this peak is so small that its presence doesn't influence the final results (upper magnification). Regarding the tails, it can be observed that the grey curve stabilizes around 0.10 $[\mu mol/g \cdot s]$, while for the oxidation curve corresponding to the real simulation this happens around 0.25 $[\mu mol/g \cdot s]$. Since the white test results can be considered as an indication of what the analyser read without any reaction, the grey curve can be considered as the zero of the instrument. The difference between the two curves, even if little (0.15 $[\mu mol/g \cdot s]$) could mean that the oxidation is not finished yet and so there is still a small CO production that continues even after several hours from the peak. Another explanation is that the redox reaction is continuing because an equilibrium condition is reached. To conclude, the CO yield of the simulation is evaluated. In order to that, other two different methods have been implemented, in addition to the integration explained at the beginning of the chapter, because of the long oxidation time. The three methods for the calculation of the area under the curve (and so the CO yield) are:

1. AREA 1: the global CO yield is evaluated in the usual way, considering only the area under the peak, and cutting the tail when the first derivate gets down to the fixed tolerance value.

2. AREA 2: the global CO yield is evaluated considering the area obtained by the net subtraction of the yellow oxidation curve and the blue curve corresponding to the white test.

3. AREA 3: the global CO yield is calculated considering the entire area under the yellow oxidation curve.

The results obtained with the three different methods are reported in Table 17.

Table 16: *Global CO yield of TEST (X) evaluated considering three different numerical integration methods.*

CO yield Area 1 $[\mu mol/g]$	CO yield Area 2 $[\mu mol/g]$	CO yield Area 3 $[\mu mol/g]$
6344	11282	16778

Comparing the three quantities, it is evident the dependency of the global CO yield with the employed method: the way the curve integration is performed strongly affect the results.

With TEST(X) the set of experimental simulation is concluded: a more detailed analysis of the ten tests will be presented in the next chapter.

Chapter 5

5. Discussion of the results

The double perovskite SFNM-04 has shown an optimal stability through the cycles, presenting replicable results for all the ten tests. In particular, the redox ability of the material has been evaluated investigating different conditions:

- Both reduction and oxidation temperature varied between 550°C and 850°C.
- A H_2 content in the reducing gas flow from 5% to 100% in N_2 based gas mixture.
- A CO_2 concentration from 6% to 100% in N_2 based gas mixture for the reducing step.
- Duration of the reduction from 15 min to 120 min.
- Oxidation times of 30 min and 7 hours.

TEST(I) represents the reference, calculated at 850 °C, 10% H_2% (for 60 min) and 20%CO_2 (for 30 min). Then in the first part, from TEST (II) to TEST(V), the experiments focused on the influence of the oxidation parameters on the performance of the perovskite. Increasing the oxidizing temperature an increase in the reaction kinetics and in the CO production is experienced. For 550°C the maximum production rate is 3.4 $[\mu mol/g/s]$ (0.45% of CO in the gas mixture), while for 850°C the value grows up to 18 $[\mu mol/g/s]$ (2.4% of CO). TEST (VI), TEST (VII) and TEST(VIII) explore instead the reduction side of the cycle. Concerning the temperature level, the CO production rate after a reduction at 550°C is about 8 $[\mu mol/g/s]$ and at 850°C is 19 $[\mu mol/g/s]$, respectively 1.1% and 2.5% in the gas mixture. For each curve the trend is the same: a fast initial increase (which corresponds the to the first rapid ion incorporation into the oxygen vacancies) and then a fast decrease, with a long tail which stabilize at a low value. The shape of the curve is affected by the operating temperature because it enhances the oxygen vacancy creation as well as activates some positive phenomena like ex solution, resulting in an accelerated reaction kinetics and so a higher CO production.

Regarding the gas mixture composition, we can note that, generally, an increase of the concentration of both the oxidizing and reducing agent brings to an increase in the CO production. With 6% CO_2/N_2 the CO production rate obtained at 850°C is 10.11 $[\mu mol/g/s]$, with pure CO_2 is 26.08 $[\mu mol/g/s]$ and the kinetics results faster: in this case the time needed for reaching the peak is almost half of the case with the lowest concentration (120 s instead of 200 s). For the reduction step at 5% H_2/N_2 the maximum CO production is 16.55 $[\mu mol/g/s]$, while for the 100% H_2 reaches the value of 36.01 $[\mu mol/g/s]$. Comparing these results, we can assert that the influence of the an higher concentration of the reducing gas is bigger if compared to the one given by the higher content of CO_2 during oxidation. The explanation can be that with more H_2 inside the reducing mixture, not only reduction is enhanced (and more oxygen vacancies are created in the SFNM-04 lattice), but also ex-solution phenomena is positively affected, even if it still dependent mainly from the reduction temperature. However, varying the amount of hydrogen doesn't seem to affect the kinetic of the oxidation reaction, since each curve presents the peak after the same amount of time; instead, changing the CO_2 content, the oxidation curves tend to move toward the left (when CO_2 increase), indicating an acceleration of the kinetic. Probably this phenomenon is due to the fact that a higher CO_2 concentration directly affects the CO formation reaction and, in particular, it can be translated in a higher partial pressure CO_2 gradient between the SFNM-04 sample and the oxidizing flux, facilitating the occupation of the vacancies.

The final tests, namely TEST (IX) and TEST (X), studied the influence of the reaction time in the fuel production process. As expected, a longer time of reduction is translated in a bigger CO production, even if both temperature and gas mixture concentrations were fixed; the reason of that is given to the fact that, leaving the material in a reducing environment for more time, hydrogen has the possibility to reach the bulk lattice, creating more oxygen vacancies where CO_2 molecules can react in the following step. Instead, if the reacting time is low, the redox reaction remains limited to the surface (where it starts thanks to the catalytic properties of SFNM-04 and ex-solution phenomenon). Increasing the oxidation time, it is observed an increase in CO production, but the difference in respect to the reference case is less important than the previous case. From the experience maturated with the performed test, the optimal configuration is finally obtained in TEST (X), where the following parameters are used:

- 100 % H_2/N_2 as reducing gas mixture.
- 20% CO_2/N_2 as oxidizing gas mixture.
- Reaction duration of 120 min for reduction step and 420 min for oxidation step.
- Isothermal cycle at 850°C.

In this condition, the results of the thermochemical cycle performed are:

- 46.13 $[\mu mol/g/s]$ as maximum CO production rate.
- 6344 $[\mu mol/g]$ as global CO yield.
- 6.20 % of CO produced in the final mixture.
- 31 % of CO_2 converted during oxidation.

These values represent the best result obtained in the ten tests performed up to now. Thanks to this study a better understanding of the SFNM-04 double perovskite material has been reached and the results reported and classified. Further studies should be carried on for this material, especially regarding the characterization of phenomenon such as ex-solution or carbonates formation. Indeed, ex-solution is a very interesting phenomenon happening during the reduction phase and can be considered as the reason why the variation of reduction parameters affects harder the cycle performance in comparison to a change in the oxidation ones. Indeed, it is one of the most important properties of the SFNM-04 material and it implies a grow of the structure during the reduction step, when $Fe2+$ and $Ni3+$ cations move from the lattice towards the surface, where they form a $FeNi_3$ alloy: this is translated in two positive effects:

1. the exsolution of $Fe2+$ and $Ni3+$ ions create a lot of vacancies inside the lattice.
2. $FeNi_3$ metal alloy acts like a catalyst for the oxidizing reaction, thus improving the final fuel production.

The structural and surface transformations happening during ex-solution are depicted in Figure 5.1.

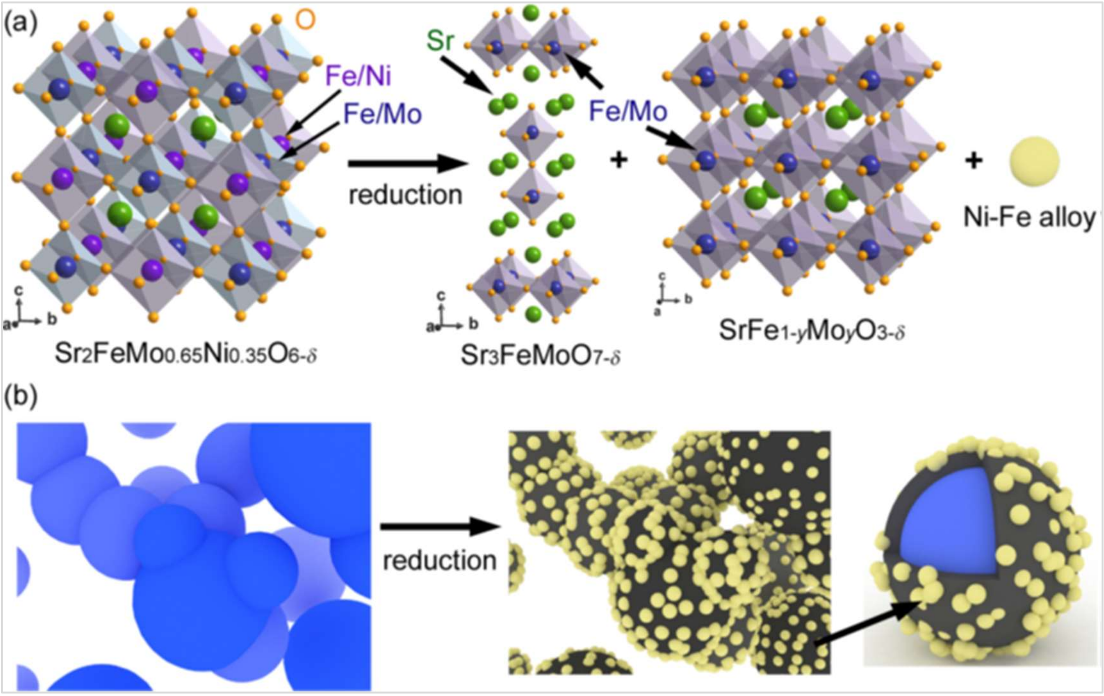

Figure 5.1: *Ex-solution transformation under reducing atmosphere in the crystal structure (a) and in the surface morphology (b)* [155].

Another consequence of the ex-solution phenomenon is the sulphide and coke poisoning resistance of the $FeNi_3$ alloys. However, a high amount of Ni can create some disadvantages, because of the creation of carbonates. Indeed, Hu et al. [157] reported the creation of strontium carbonate ($SrCO_3$) caused by the catalyst action of Ni in the $Sr_2Fe_{1.5-x}Mo_{0.5}Ni_xO$ ($x = 0, 0.005, 0.1, 0.2$) double perovskite. This material is usually employed as cathode for CO_2 electroreduction, and nickel is needed, since the presence of $Fe - Ni$ cations promote the process; however, because of the weak $Ni - O$ bonds created in the material (which favourite the $SrCO_3$ formation than the CO_2 reduction), carbonates are generated, and their deposition blocks the charge transfer and diffusion of molecules on the surface of the cathode. Hu reported that the driving force for the creation of these carbonates is the voltage applied to the SOEC (Solid Oxide Electrolysis Cell). Instead, when performing redox cycles inside chemical looping process, the main problem given by these carbonates is that they block the re- oxidation of the sample, reducing the CO final production; in this case, the driving force is the high temperature heat coming from the concentrating solar panels. With the experiments performed in the microreactor, the correct detection of carbonate creation can’t be made. However, in TGA, if a continuous increase of the mass sample during oxidation is experienced, probably it means that carbonates compounds are generating.

In conclusion, we can assert that ex-solution phenomenon is responsible for the enhanced electronic/ionic conduction and catalytic properties of the SFNM-04 double perovskite; however, an excessive Ni doping can bring to pore blocking as consequence of carbonates creation and thus damaging the stability and repeatability of the cycles: that’s why the nickel doping process for SFM structure is crucial in order to create an optimal perovskite material for chemical looping application.

Chapter 6

6. Conclusions

This work is aimed to evaluate the behavior and the performance of a new double perovskite material in chemical looping applications for the splitting of CO_2. This material, namely $Sr_2FeMo_{0.6}Ni_{0.4}O_{6-\delta}$ (SFNM-04), has been synthesized by University of Udine. The study is inserted in a collaboration project between the Massachusetts Institute of Technology (M.I.T.) of Boston, University of Udine, and Polytechnic of Turin. Tests were performed at the CO_2 *Circle Lab* of the Environment Park, Turin. Chemical looping is a very interesting technology in which redox cycles are carried out in suitable reactors, driven by high temperature energy coming from concentrating solar. During cycles, reduction and oxidation reactions take place between the oxygen carrier and reducing and oxidating fluxes entering the reactor: oxygen carrier materials are firstly reduced and then regenerated during the oxidation in CO_2 at the end of the cycle, producing CO, in this case, but also hydrogen when water is used as oxidating agent. Most of the research is aimed at finding the best suitable material for this type of application. In this dissertation a new double perovskite structure has been investigated. As already known from literature, perovskite structures are very stable during cycles and can contain a big amount of oxygen vacancies, leading to higher productivity in comparison to common materials. Furthermore, double perovskites as SFNM-04 present the ex-solution phenomenon during reduction, which results in a grow of the structure and in the formation, from ex-solution, of Iron-Nickel alloy nanoparticles on the surface of the material; these alloys have catalytic properties, enhance the reactivity of the oxygen carrier and create more vacancies in the lattice. In this work, experimental tests are described in order to study the SFNM-04 properties during all the thermochemical cycles and understand which are the most performative condition for the material. In particular, the parameters considered are temperature, concentration of hydrogen and carbon dioxide inside the reducing and oxidating mixtures, and the time in which the sample is left in these two types of environments. The operated conditions are changed following these ranges:

- Temperature of oxidation and reduction between 550°C and 850°C.

- Reducing and oxidizing mixture composition using from 5% to 100% of H_2/N_2 and from 6% up to pure CO_2 during reduction and oxidation steps, respectively.
- Reduction time from 15 min to 120 minutes.
- Oxidation time of 15, 30 and 420 minutes.

An electric furnace is used to simulate solar energy and the reactor can be considered as continuous flow reactor in which the sample is inserted, inside a boat-shaped alumina crucible. Final performances are evaluated in terms of global CO production rate, CO final yield and CO_2 converted. Results show the suitability of SFNM-04 double perovskite structure for chemical looping applications, because of its stability during cycles (productivity doesn't seem to be affected by the operated number of cycles), the high number of vacancies created, and reactivity with carbon dioxide for fuel production. The best performances are obtained with the following operating characteristics:

- Isothermal cycle at 850°C.
- 100% H_2 gas flow for the reducing ambient for 60 minutes.
- 20% CO_2/N_2 oxidating environment for 420 minutes.

A bigger concentration of hydrogen in the reducing mixture is found to enhance the reduction of the sample, as well as a higher temperature and duration of the step. More H_2 in the environment helps the oxygen vacancies creation mechanism, while temperature activates ex solution phenomenon and extended times of reaction guarantee a reduction up to the bulk lattice. Concerning the oxidation, similar considerations can be done for temperature, CO_2 concentration and oxidation duration. After the ten cycles it can be stated that a completed reduction or oxidation of the material is never experienced. White tests have been performed too, in order to study better the tail that the CO production rate curves show for each test: a difference is found between the tail of the real test (with the SFNM-04 sample inside the reactor) and the white test, meaning that the material continues its oxidation after the peak, even after some hours: indeed, TEST(X) curves shows this behaviour with a duration of oxidation of seven hours. The explanation for this long tail is also found in a possible difficulty of the CO_2 molecules to reach the inner part of the lattice. However, it must be noticed that the behaviour experienced can be due to various mechanism not directly visible using the gas analyser system in the laboratory and thus difficult to identify. One of these phenomena, which certainly needs for more attention, is the carbonate and molybdates creation ($SrCO_3$ and $SrMoO_4$) due to the Ni presence on the surface (after the ex-solution). Indeed, nickel is a powerful catalyst and promotes the carbonate formation, negatively affecting the sample redox performances: $SrCO_3$ hinders carbon dioxide dissociation and stabilize $SrMoO_4$, which represents the insulating phase. For a better comprehension of this SFNM-04 behavior, future tests could be carried out using thermogravimetric analysis (TGA), which measures mass evolution during the cycles. X-ray diffraction XRD post-mortem and SEM (Scanning Electron Microscopy) analysis are also useful instruments.

In conclusion, double perovskite SFNM-04 material resulted as promising oxygen carrier for chemical looping application: the highest attraction is due to its regenerability properties, stability and to the fact that shows good results at lower temperatures in comparison to other materials, such as ceria or metal oxides. The temperature is indeed an important parameter: if the reduction can be performed at lower temperature, the cycle can be driven in isothermal condition, thus simplifying the process, and also leading to an easier integration of the chemical looping technology to different concentrating solar systems. Chemical looping from solar energy is still at the first levels of research (proving the basing concept of the technology). This work is inserted in this phase. Once the technology is validated in laboratory and the best possible material for the process is found, the technology can shift to next level, in particular to a thermodynamic study of the cycle. Syngas produced via solar chemical looping will be a green, clean, solar fuel and it will certainly contribute actively to the energy transition the world is needing.

References

[1] H. Ritchie and M. Roser, “CO_2 and Greenhouse Gas Emissions - Our World in Data,” 2020. https://ourworldindata.org/co2-and-other-greenhouse-gas-emissions#citation (accessed Nov. 10, 2021).

[2] “AR5 Synthesis Report: Climate Change 2014 — IPCC.” https://www.ipcc.ch/report/ar5/syr/ (accessed Nov. 11, 2021).

[3] “No Title.” https://www.co2.earth/.

[4] “December 2020 Climate Action Tracker Paris Agreement turning point.”

[5] “Energy roadmap 2050 Energy,” doi: 10.2833/10759.

[6] “European Technology and Innovation Platform for Zero Emission Plant ZEP Recommendations for the Governance of the Energy Union,” 2017, Accessed: Nov. 11, 2021. [Online]. Available: https://www.thecrownestate.co.uk/media/389780/ei-business-models-for-commercial-co2-transport-and-.

[7] “World coal consumption variation 2019-2020 – Charts – Data & Statistics - IEA.” https://www.iea.org/data-and-statistics/charts/world-coal-consumption-variation-2019-2020 (accessed Nov. 11, 2021).

[8] “Key World Energy Statistics 2020 – Analysis - IEA.” https://www.iea.org/reports/key-world-energy-statistics-2020 (accessed Nov. 11, 2021).

[9] “World Energy Outlook 2016 – Analysis - IEA.” https://www.iea.org/reports/world-energy-outlook-2016 (accessed Nov. 11, 2021).

[10] G. E. Halkos and E.-C. Gkampoura, “Reviewing Usage, Potentials, and Limitations of Renewable Energy Sources,” *Energies*, vol. 13, no. 11, p. 2906, Jun. 2020, doi: 10.3390/en13112906.

[11] E. Rozzi, F. D. Minuto, A. Lanzini, and P. Leone, "Green Synthetic Fuels: Renewable Routes for the Conversion of Non-Fossil Feedstocks into Gaseous Fuels and Their End Uses," *Energies*, vol. 13, no. 2, p. 420, Jan. 2020, doi: 10.3390/en13020420.

[12] E. Millán, N. Mota, R. Guil-López, B. Pawelec, J. L. García Fierro, and R. M. Navarro, "Direct Synthesis of Dimethyl Ether from Syngas on Bifunctional Hybrid Catalysts Based on Supported H3PW12O40 and Cu-ZnO(Al): Effect of Heteropolyacid Loading on Hybrid Structure and Catalytic Activity," *Catalysts*, vol. 10, no. 9, p. 1071, Sep. 2020, doi: 10.3390/catal10091071.

[13] D. . Wilhelm, D. . Simbeck, A. . Karp, and R. . Dickenson, "Syngas production for gas-to-liquids applications: technologies, issues and outlook," *Fuel Process. Technol.*, vol. 71, no. 1–3, pp. 139–148, Jun. 2001, doi: 10.1016/S0378-3820(01)00140-0.

[14] "World Energy Model – Analysis - IEA." https://www.iea.org/reports/world-energy-model (accessed Nov. 11, 2021).

[15] I. Energy Agency, "Technology Perspectives Energy Special Report on Carbon Capture Utilisation and Storage CCUS in clean energy transitions." [Online]. Available: www.iea.org/t&c/.

[16] "No Title," [Online]. Available: https://www.iea.org/fuels-and-technologies/carbon-capture-utilisation-and-storage.

[17] "About CCUS – Analysis - IEA." https://www.iea.org/reports/about-ccus (accessed Nov. 11, 2021).

[18] J. Wilcox, "Carbon capture," *Carbon Capture*, pp. 1–323, Jan. 2012, doi: 10.1007/978-1-4614-2215-0.

[19] International Energy Agency (IEA), "CO2 emisions from fuel combustion," *IEA Publ.*, pp. 1–165, 2019, [Online]. Available: https://iea.blob.core.windows.net/assets/eb3b2e8d-28e0-47fd-a8ba-160f7ed42bc3/CO2_Emissions_from_Fuel_Combustion_2019_Highlights.pdf.

[20] M. Fowler and J. Lewis, "The Role of Carbon Capture and Storage Incentives in

Ammonia Fuel Production ," Accessed: Nov. 11, 2021. [Online]. Available: https://www.catf.us/resource/fuels-without-carbon/.

[21] M. Bert, Ogunlade Davidson, de C. Heleen, L. Manuela, and M. Leo, "Carbon Dioxide Capture and Storage — IPCC 200520," 2005. Accessed: Nov. 11, 2021. [Online]. Available: https://www.ipcc.ch/report/carbon-dioxide-capture-and-storage/.

[22] A. Al-Mamoori, A. Krishnamurthy, A. A. Rownaghi, and F. Rezaei, "Carbon Capture and Utilization Update," *Energy Technol.*, vol. 5, no. 6, pp. 834–849, Jun. 2017, doi: 10.1002/ENTE.201600747.

[23] D. Stolten and V. (Eds. . Scherer, "Efficient Carbon Capture for Coal Power Plants," 2011.

[24] B. Erlach, M. Schmidt, and G. Tsatsaronis, "Comparison of carbon capture IGCC with pre-combustion decarbonisation and with chemical-looping combustion," *Energy*, vol. 36, no. 6, pp. 3804–3815, Jun. 2011, doi: 10.1016/J.ENERGY.2010.08.038.

[25] A. Viscogliosi, C. Bassano, and P. Deiana, "Analisi e modellazione di impianti di produzione elettrica a carbone equipaggiati con sistemi CCS."

[26] E. R. van Selow, P. D. Cobden, R. W. van den Brink, J. R. Hufton, and A. Wright, "Performance of sorption-enhanced water-gas shift as a pre-combustion CO2 capture technology," *Energy Procedia*, vol. 1, no. 1, pp. 689–696, Feb. 2009, doi: 10.1016/J.EGYPRO.2009.01.091.

[27] " OXY COMBUSTION WITH CO 2 CAPTURE GLOBAL CCS INSTITUTE-CO 2 CAPTURE TECHNOLOGIES CO 2 Capture Technologies, Section 4 1 CONTENTS," 2012.

[28] F. M. Baena-Moreno, M. Rodríguez-Galán, F. Vega, B. Alonso-Fariñas, L. F. Vilches Arenas, and B. Navarrete, "Carbon capture and utilization technologies: a literature review and recent advances," *Energy Sources, Part A Recover. Util. Environ. Eff.*, vol. 41, no. 12, pp. 1403–1433, 2019, doi: 10.1080/15567036.2018.1548518.

[29] "Capturing CO2: Gas Compression vs. Liquefaction." https://www.powermag.com/capturing-co2-gas-compression-vs-liquefaction/ (accessed Nov. 11, 2021).

[30] "Global Energy Review 2021 – Analysis - IEA." https://www.iea.org/reports/global-energy-review-2021 (accessed Nov. 11, 2021).

[31] N. Ruffini, "Analisi termodinamica di un impianto di potenza innovativo ad alta efficienza ed emissioni quasi nulle basato sull'idrogassificazione del carbone," 2004.

[32] F. Jin, *Principles of Enhanced Oil Recovery*. 2017.

[33] P. Freund, "Cattura e stoccaggio di CO2 prodotto dai combustibili fossili.," *Enciclopedia degli Idrocarburi, Treccani*. p. VOLUME III: NUOVI SVILUPPI: ENERGIA, TRASPORTI, SO, 2009.

[34] "IEA GHG Weyburn CO 2 Monitoring & Storage Project."

[35] "Tracking Clean Energy Progress 2017 – Analysis - IEA." https://www.iea.org/reports/tracking-clean-energy-progress-2017 (accessed Nov. 11, 2021).

[36] "ANNUAL REPORT 2018 ," 2018.

[37] A. Kätelhön, R. Meys, S. Deutz, S. Suh, and A. Bardow, "Climate change mitigation potential of carbon capture and utilization in the chemical industry," *Proc. Natl. Acad. Sci. U. S. A.*, vol. 166, no. 23, pp. 11187–11194, Jun. 2019, doi: 10.1073/PNAS.1821029116/-/DCSUPPLEMENTAL.

[38] A. Steynberg and M. Dry, "Fischer-Tropsch technology," p. 700, 2004.

[39] C. Agrafiotis, H. Von Storch, M. Roeb, and C. Sattler, "Solar thermal reforming of methane feedstocks for hydrogen and syngas production—A review," *Renew. Sustain. Energy Rev.*, vol. 29, pp. 656–682, Jan. 2014, doi: 10.1016/J.RSER.2013.08.050.

[40] A. Uddin, "Solar fuels via two-step thermochemical redox cycle for power and fuel production," pp. 1–394, Jul. 2019, doi: 10.4/JQUERY-UI.MIN.JS.

[41] Y. Wang, D. He, H. Chen, and D. Wang, “Catalysts in electro-, photo- and photoelectrocatalytic CO2 reduction reactions,” *J. Photochem. Photobiol. C Photochem. Rev.*, vol. 40, pp. 117–149, Sep. 2019, doi: 10.1016/J.JPHOTOCHEMREV.2019.02.002.

[42] C. Agrafiotis, M. Roeb, and C. Sattler, “A review on solar thermal syngas production via redox pair-based water/carbon dioxide splitting thermochemical cycles,” *Renew. Sustain. Energy Rev.*, vol. 42, pp. 254–285, 2015, doi: 10.1016/j.rser.2014.09.039.

[43] C. Graves, S. D. Ebbesen, M. Mogensen, and K. S. Lackner, “Sustainable hydrocarbon fuels by recycling CO2 and H 2O with renewable or nuclear energy,” *Renew. Sustain. Energy Rev.*, vol. 15, no. 1, pp. 1–23, 2011, doi: 10.1016/j.rser.2010.07.014.

[44] S. A. Chernyak *et al.*, “Sintered Fe/CNT framework catalysts for CO2 hydrogenation into hydrocarbons,” *Carbon N. Y.*, vol. 168, pp. 475–484, Oct. 2020, doi: 10.1016/J.CARBON.2020.06.067.

[45] B. C. Sempuga and Y. Yao, “CO2 hydrogenation from a process synthesis perspective: Setting up process targets,” *J. CO2 Util.*, vol. 20, pp. 34–42, Jul. 2017, doi: 10.1016/J.JCOU.2017.05.004.

[46] B. Wei, *A novel solar-driven system for two-step conversion of CO2 with ceria-based catalysts*. Industrial Engineering and Management, KTH Royal Institute of Technology, 2014.

[47] W. Li *et al.*, “A short review of recent advances in CO2 hydrogenation to hydrocarbons over heterogeneous catalysts,” *RSC Adv.*, vol. 8, no. 14, pp. 7651–7669, Feb. 2018, doi: 10.1039/C7RA13546G.

[48] R. van de Krol and B. A. Parkinson, “Perspectives on the photoelectrochemical storage of solar energy,” *MRS Energy Sustain.*, vol. 4, no. 1, Apr. 2017, doi: 10.1557/MRE.2017.15.

[49] C. C. L. McCrory, S. Jung, I. M. Ferrer, S. M. Chatman, J. C. Peters, and T. F. Jaramillo, “Benchmarking Hydrogen Evolving Reaction and Oxygen Evolving

Reaction Electrocatalysts for Solar Water Splitting Devices," *J. Am. Chem. Soc.*, vol. 137, no. 13, pp. 4347–4357, Apr. 2015, doi: 10.1021/JA510442P/SUPPL_FILE/JA510442P_SI_001.PDF.

[50] M. W. Kanan and D. G. Nocera, "In situ formation of an oxygen-evolving catalyst in neutral water containing phosphate and Co2+," *Science*, vol. 321, no. 5892, pp. 1072–1075, Aug. 2008, doi: 10.1126/SCIENCE.1162018.

[51] L. Jiang, J. Li, K. Wang, G. Zhang, Y. Li, and X. Wu, "Low boiling point solvent mediated strategy to synthesize functionalized monolayer carbon nitride for superior photocatalytic hydrogen evolution," *Appl. Catal. B Environ.*, vol. 260, p. 118181, Jan. 2020, doi: 10.1016/J.APCATB.2019.118181.

[52] S. Haussener, S. Hu, C. Xiang, A. Z. Weber, and N. S. Lewis, "Simulations of the irradiation and temperature dependence of the efficiency of tandem photoelectrochemical water-splitting systems," *Energy Environ. Sci.*, vol. 6, no. 12, pp. 3605–3618, Nov. 2013, doi: 10.1039/C3EE41302K.

[53] D. J. Deka, J. Kim, S. Gunduz, M. Ferree, A. C. Co, and U. S. Ozkan, "Temperature-induced changes in the synthesis gas composition in a high-temperature H2O and CO2 co-electrolysis system," *Appl. Catal. A Gen.*, vol. 602, p. 117697, Jul. 2020, doi: 10.1016/J.APCATA.2020.117697.

[54] S. Koumi Ngoh and D. Njomo, "An overview of hydrogen gas production from solar energy," *Renew. Sustain. Energy Rev.*, vol. 16, no. 9, pp. 6782–6792, Dec. 2012, doi: 10.1016/J.RSER.2012.07.027.

[55] M. Romero and A. Steinfeld, "Concentrating solar thermal power and thermochemical fuels," *Energy Environ. Sci.*, vol. 5, no. 11, pp. 9234–9245, Oct. 2012, doi: 10.1039/C2EE21275G.

[56] A. Steinfeld and R. Palumbo, "Solar Thermochemical Process Technology," *Encycl. Phys. Sci. Technol.*, pp. 237–256, 2003, doi: 10.1016/B0-12-227410-5/00698-0.

[57] M. Tou, R. Michalsky, and A. Steinfeld, "Solar-Driven Thermochemical Splitting of CO2 and In Situ Separation of CO and O2 across a Ceria Redox Membrane

Reactor," *Joule*, vol. 1, no. 1, pp. 146–154, Sep. 2017, doi: 10.1016/j.joule.2017.07.015.

[58] L. Zhu, Y. Lu, and S. Shen, "Solar fuel production at high temperatures using ceria as a dense membrane," *Energy*, vol. C, no. 104, pp. 53–63, Jun. 2016, doi: 10.1016/J.ENERGY.2016.03.108.

[59] M. Luo *et al.*, "Review of hydrogen production using chemical-looping technology," *Renew. Sustain. Energy Rev.*, vol. 81, pp. 3186–3214, Jan. 2018, doi: 10.1016/J.RSER.2017.07.007.

[60] B. Moghtaderi, "Review of the recent chemical looping process developments for novel energy and fuel applications," *Energy and Fuels*, vol. 26, no. 1, pp. 15–40, 2012, doi: 10.1021/ef201303d.

[61] E. Jerndal, T. Mattisson, and A. Lyngfelt, "Thermal Analysis of Chemical-Looping Combustion," *Chem. Eng. Res. Des.*, vol. 84, no. 9, pp. 795–806, Sep. 2006, doi: 10.1205/CHERD05020.

[62] A. Lyngfelt, B. Leckner, and T. Mattisson, "A fluidized-bed combustion process with inherent CO2 separation; application of chemical-looping combustion," *Chem. Eng. Sci.*, vol. 56, no. 10, pp. 3101–3113, May 2001, doi: 10.1016/S0009-2509(01)00007-0.

[63] L. Fan, F. Li, and S. Ramkumar, "Utilization of chemical looping strategy in coal gasification processes," *Particuology*, vol. 6, no. 3, pp. 131–142, Jun. 2008, doi: 10.1016/J.PARTIC.2008.03.005.

[64] J. Udomsirichakorn and P. A. Salam, "Review of hydrogen-enriched gas production from steam gasification of biomass: The prospect of CaO-based chemical looping gasification," *Renew. Sustain. Energy Rev.*, vol. 30, pp. 565–579, Feb. 2014, doi: 10.1016/J.RSER.2013.10.013.

[65] C. G. Cortés, E. Tzimas, and S. D. Peteves, "Technologies for Coal based Hydrogen and Electricity Co-production Power Plants with CO 2 Capture," doi: 10.2790/23969.

[66] F. Li *et al.*, "Syngas Chemical Looping Gasification Process: Oxygen Carrier

Particle Selection and Performance," *Energy and Fuels*, vol. 23, no. 8, pp. 4182–4189, Aug. 2009, doi: 10.1021/EF900236X.

[67] Y. Lin *et al.*, "Review of Biomass Chemical Looping Gasification in China," *Energy and Fuels*, vol. 34, no. 7, pp. 7847–7862, Jul. 2020, doi: 10.1021/ACS.ENERGYFUELS.0C01022/SUPPL_FILE/EF0C01022_SI_001.PDF.

[68] X. Zhu, K. Li, L. Neal, and F. Li, "Perovskites as Geo-inspired Oxygen Storage Materials for Chemical Looping and Three-Way Catalysis: A Perspective," *ACS Catal.*, vol. 8, no. 9, pp. 8213–8236, Sep. 2018, doi: 10.1021/acscatal.8b01973.

[69] M. Rydén, A. Lyngfelt, and T. Mattisson, "Chemical-Looping Combustion and Chemical-Looping Reforming in a Circulating Fluidized-Bed Reactor Using Ni-Based Oxygen Carriers," *Energy and Fuels*, vol. 22, no. 4, pp. 2585–2597, Jul. 2008, doi: 10.1021/EF800065M.

[70] M. Rydén, A. Lyngfelt, and T. Mattisson, "Synthesis gas generation by chemical-looping reforming in a continuously operating laboratory reactor," *Fuel*, vol. 85, no. 12–13, pp. 1631–1641, Sep. 2006, doi: 10.1016/J.FUEL.2006.02.004.

[71] J. Adanez, A. Abad, F. Garcia-Labiano, P. Gayan, and L. F. De Diego, "Progress in chemical-looping combustion and reforming technologies," *Prog. Energy Combust. Sci.*, vol. 38, no. 2, pp. 215–282, 2012, doi: 10.1016/j.pecs.2011.09.001.

[72] F. G. Kerry, "Industrial gas handbook: gas separation and purification. 1st ed. Boca Raton, FL: CRC Press; 2007," p. 521, 2007, Accessed: Nov. 12, 2021. [Online]. Available: https://www.crcpress.com/Industrial-Gas-Handbook-Gas-Separation-and-Purification/Kerry/p/book/9780849390050.

[73] B. Moghtaderi, "Application of Chemical Looping Concept for Air Separation at High Temperatures†," *Energy and Fuels*, vol. 24, no. 1, pp. 190–198, Jan. 2009, doi: 10.1021/EF900553J.

[74] Q. Yin, J. Kniep, and Y. S. Lin, "Oxygen sorption and desorption properties of Sr-Co-Fe oxide," *Chem. Eng. Sci.*, vol. 63, no. 8, pp. 2211–2218, Apr. 2008, doi: 10.1016/J.CES.2008.01.016.

[75] K. Shah, B. Moghtaderi, J. Zanganeh, and T. Wall, "Integration options for novel chemical looping air separation (ICLAS) process for oxygen production in oxy-fuel coal fired power plants," *Fuel*, vol. 107, pp. 356–370, 2013, doi: 10.1016/J.FUEL.2013.01.007.

[76] B. McKee, "Net Zero by 2050 – Analysis - IEA." https://www.iea.org/reports/net-zero-by-2050 (accessed Nov. 12, 2021).

[77] K. Wang, Q. B. Yu, Q. Qin, and J. L. Liu, "Experimental Investigation of the Reactivity of the Copper-based Oxygen Carrier Used in Chemical Looping Air Separation," *IOP Conf. Ser. Earth Environ. Sci.*, vol. 86, no. 1, p. 012006, Oct. 2017, doi: 10.1088/1755-1315/86/1/012006.

[78] K. Shah, B. Moghtaderi, and T. Wall, "Selection of Suitable Oxygen Carriers for Chemical Looping Air Separation: A Thermodynamic Approach," *Energy and Fuels*, vol. 26, no. 4, pp. 2038–2045, Apr. 2012, doi: 10.1021/EF300132C.

[79] B. Moghtaderi and E. Doroodchi, "PATENT: Chemical looping removal of ventilation air methane (VAM)."

[80] A. Tong, S. Bayham, M. V. Kathe, L. Zeng, S. Luo, and L. S. Fan, "Iron-based syngas chemical looping process and coal-direct chemical looping process development at Ohio State University," *Appl. Energy*, vol. 113, pp. 1836–1845, Jan. 2014, doi: 10.1016/J.APENERGY.2013.05.024.

[81] B. Wei, R. Fakhrai, B. Saadatfar, G. Mohan, and T. Fransson, "The Design of a Solar-driven Catalytic Reactor for CO2 Conversions," *Energy Procedia*, vol. 57, pp. 2752–2761, Jan. 2014, doi: 10.1016/J.EGYPRO.2014.10.307.

[82] C. N. R. Rao and S. Dey, "Solar thermochemical splitting of water to generate hydrogen," *Proc. Natl. Acad. Sci. U. S. A.*, vol. 114, no. 51, pp. 13385–13393, Dec. 2017, doi: 10.1073/PNAS.1700104114/-/DCSUPPLEMENTAL.

[83] W. C. Chueh *et al.*, "High-flux solar-driven thermochemical dissociation of CO2 and H2O using nonstoichiometric ceria," *Science*, vol. 330, no. 6012, pp. 1797–1801, Dec. 2010, doi: 10.1126/SCIENCE.1197834.

[84] J. Adanez, A. Abad, F. Garcia-Labiano, P. Gayan, and L. F. De Diego, "Progress

in Chemical-Looping Combustion and Reforming technologies," *Prog. Energy Combust. Sci.*, vol. 38, no. 2, pp. 215–282, Apr. 2012, doi: 10.1016/J.PECS.2011.09.001.

[85] X. Zhao *et al.*, "Biomass-based chemical looping technologies: the good, the bad and the future," *Energy Environ. Sci.*, vol. 10, no. 9, pp. 1885–1910, Sep. 2017, doi: 10.1039/C6EE03718F.

[86] R. J. Carrillo and J. R. Scheffe, "Advances and trends in redox materials for solar thermochemical fuel production," *Sol. Energy*, vol. 156, pp. 3–20, 2017, doi: 10.1016/j.solener.2017.05.032.

[87] I. Alxneit, "Assessing the feasibility of separating a stoichiometric mixture of zinc vapor and oxygen by a fast quench – Model calculations," *Sol. Energy*, vol. 82, no. 11, pp. 959–964, Nov. 2008, doi: 10.1016/J.SOLENER.2008.05.009.

[88] I. Vishnevetsky, A. Berman, and M. Epstein, "Features of solar thermochemical redox cycles for hydrogen production from water as a function of reactants' main characteristics," *Int. J. Hydrogen Energy*, vol. 36, no. 4, pp. 2817–2830, Feb. 2011, doi: 10.1016/J.IJHYDENE.2010.11.027.

[89] P. G. Loutzenhiser, A. Meier, and A. Steinfeld, "Review of the Two-Step H2O/CO2-Splitting solar thermochemical cycle based on Zn/ZnO redox reactions," *Materials*, vol. 3, no. 11. pp. 4922–4938, 2010, doi: 10.3390/ma3114922.

[90] P. Haueter, S. Moeller, R. Palumbo, and A. Steinfeld, "The production of zinc by thermal dissociation of zinc oxide—solar chemical reactor design," *Sol. Energy*, vol. 67, no. 1–3, pp. 161–167, Jul. 1999, doi: 10.1016/S0038-092X(00)00037-2.

[91] S. Chuayboon, S. Abanades, and S. Rodat, "Solar chemical looping gasification of biomass with the ZnO/Zn redox system for syngas and zinc production in a continuously-fed solar reactor," *Fuel*, vol. 215, no. March 2017, pp. 66–79, 2018, doi: 10.1016/j.fuel.2017.11.021.

[92] R. Palumbo, M. Keunecke, S. Möller, and A. Steinfeld, "Reflections on the design of solar thermal chemical reactors: Thoughts in transformation," *Energy*, vol. 29,

no. 5–6, pp. 727–744, 2004, doi: 10.1016/S0360-5442(03)00180-4.

[93] K. S. Kang, C. H. Kim, W. C. Cho, K. K. Bae, S. H. Kim, and C. S. Park, “Novel two-step thermochemical cycle for hydrogen production from water using germanium oxide: KIER 4 thermochemical cycle,” *Int. J. Hydrogen Energy*, vol. 34, no. 10, pp. 4283–4290, May 2009, doi: 10.1016/J.IJHYDENE.2009.03.017.

[94] M. Chambon, S. Abanades, and G. Flamant, “Kinetic investigation of hydrogen generation from hydrolysis of SnO and Zn solar nanopowders,” *Int. J. Hydrogen Energy*, vol. 34, no. 13, pp. 5326–5336, Jul. 2009, doi: 10.1016/J.IJHYDENE.2009.04.064.

[95] M. Kromer, K. Roth, R. Takata, and P. Chin, “Support for Cost Analyses on Solar-Driven High Temperature Thermochemical Water-Splitting Cycles Final Report to: Department of Energy Report prepared by TIAX LLC,” 2011.

[96] J. Hu, V. V. Galvita, H. Poelman, and G. B. Marin, “Advanced chemical looping materials for CO2 utilization: A review,” *Materials*, vol. 11, no. 7. MDPI AG, Jul. 10, 2018, doi: 10.3390/ma11071187.

[97] H. A. Alalwan, D. M. Cwiertny, and V. H. Grassian, “Co3O4 nanoparticles as oxygen carriers for chemical looping combustion: A materials characterization approach to understanding oxygen carrier performance,” *Chem. Eng. J.*, vol. 319, pp. 279–287, 2017, doi: 10.1016/J.CEJ.2017.02.134.

[98] H. Jin, T. Okamoto, and M. Ishida, “Development of a Novel Chemical-Looping Combustion: Synthesis of a Looping Material with a Double Metal Oxide of CoO−NiO,” *Energy and Fuels*, vol. 12, no. 6, pp. 1272–1277, 1998, doi: 10.1021/EF980080G.

[99] T. Mattisson, A. Järdnäs, and A. Lyngfelt, “Reactivity of Some Metal Oxides Supported on Alumina with Alternating Methane and OxygenApplication for Chemical-Looping Combustion,” *Energy and Fuels*, vol. 17, no. 3, pp. 643–651, May 2003, doi: 10.1021/EF020151I.

[100] I. Adánez-Rubio, H. Bautista, M. T. Izquierdo, P. Gayán, A. Abad, and J. Adánez, “Development of a magnetic Cu-based oxygen carrier for the chemical looping

with oxygen uncoupling (CLOU) process," *Fuel Process. Technol.*, vol. 218, p. 106836, Jul. 2021, doi: 10.1016/J.FUPROC.2021.106836.

[101] J. Adánez, L. F. De Diego, F. García-Labiano, P. Gayán, A. Abad, and J. M. Palacios, "Selection of Oxygen Carriers for Chemical-Looping Combustion," *Energy and Fuels*, vol. 18, no. 2, pp. 371–377, Mar. 2004, doi: 10.1021/EF0301452.

[102] Q. Zafar, T. Mattisson, and B. Gevert, "Redox Investigation of Some Oxides of Transition-State Metals Ni, Cu, Fe, and Mn Supported on SiO2 and MgAl2O4," *Energy and Fuels*, vol. 20, no. 1, pp. 34–44, Jan. 2005, doi: 10.1021/EF0501389.

[103] J. R. Kelly and I. Denry, "Stabilized zirconia as a structural ceramic: An overview," *Dent. Mater.*, vol. 24, no. 3, pp. 289–298, Mar. 2008, doi: 10.1016/J.DENTAL.2007.05.005.

[104] M. Johansson, T. Mattisson, and A. Lyngfelt, "Investigation of Mn3O4 With Stabilized ZrO2 for Chemical-Looping Combustion," *Chem. Eng. Res. Des.*, vol. 84, no. 9, pp. 807–818, Sep. 2006, doi: 10.1205/CHERD.05206.

[105] S. A. Theofanidis, V. V. Galvita, H. Poelman, and G. B. Marin, "Enhanced Carbon-Resistant Dry Reforming Fe-Ni Catalyst: Role of Fe," *ACS Catal.*, vol. 5, no. 5, pp. 3028–3039, May 2015, doi: 10.1021/ACSCATAL.5B00357.

[106] A. Lyngfelt, "Oxygen Carriers for Chemical Looping Combustion-4 000 h of Operational Experience Chemical Looping-An Alternative Concept for Efficient and Clean Use of Fossil Resources La Boucle Chimique-Un concept alternatif pour un usage propre et efficace des ressources fossiles," *Oil Gas Sci. Technol. IFP Energies Nouv.*, vol. 66, no. 2, pp. 161–172, 2011, doi: 10.2516/ogst/2010038.

[107] J. E. Readman, A. Olafsen, J. B. Smith, and R. Blom, "Chemical Looping Combustion Using NiO/NiAl2O4: Mechanisms and Kinetics of Reduction−Oxidation (Red-Ox) Reactions from In Situ Powder X-ray Diffraction and Thermogravimetry Experiments," *Energy and Fuels*, vol. 20, no. 4, pp. 1382–1387, Jul. 2006, doi: 10.1021/EF0504319.

[108] M. R. Quddus, M. M. Hossain, and H. I. De Lasa, “Ni based oxygen carrier over γ-Al2O3 for chemical looping combustion: Effect of preparation method on metal support interaction,” *Catal. Today*, vol. 210, pp. 124–134, Jul. 2013, doi: 10.1016/J.CATTOD.2013.02.005.

[109] A. Cabello *et al.*, “Relevance of the catalytic activity on the performance of a NiO/CaAl2O4 oxygen carrier in a CLC process,” *Appl. Catal. B Environ.*, vol. 147, pp. 980–987, Apr. 2014, doi: 10.1016/J.APCATB.2013.10.034.

[110] K. E. Sedor, M. M. Hossain, and H. I. de Lasa, “Reactivity and stability of Ni/Al2O3 oxygen carrier for chemical-looping combustion (CLC),” *Chem. Eng. Sci.*, vol. 63, no. 11, pp. 2994–3007, Jun. 2008, doi: 10.1016/J.CES.2008.02.021.

[111] B. M. Corbella, L. F. De Diego, F. García-Labiano, J. Adánez, and J. M. Palacios, “Performance in a fixed-bed reactor of titania-supported nickel oxide as oxygen carriers for the chemical-looping combustion of methane in multicycle tests,” *Ind. Eng. Chem. Res.*, vol. 45, no. 1, pp. 157–165, Jan. 2006, doi: 10.1021/IE050756C.

[112] M. Rydén, M. Johansson, A. Lyngfelt, and T. Mattisson, “NiO supported on Mg–ZrO2 as oxygen carrier for chemical-looping combustion and chemical-looping reforming,” *Energy Environ. Sci.*, vol. 2, no. 9, pp. 970–981, Aug. 2009, doi: 10.1039/B904370E.

[113] L. Silvester, A. Antzara, G. Boskovic, E. Heracleous, A. A. Lemonidou, and D. B. Bukur, “NiO supported on Al2O3 and ZrO2 oxygen carriers for chemical looping steam methane reforming,” *Int. J. Hydrogen Energy*, vol. 40, no. 24, pp. 7490–7501, Jun. 2015, doi: 10.1016/J.IJHYDENE.2014.12.130.

[114] S. Bhavsar and G. Veser, “Reducible supports for Ni-based oxygen carriers in chemical looping combustion,” *Energy and Fuels*, vol. 27, no. 4, pp. 2073–2084, Apr. 2013, doi: 10.1021/EF400184B.

[115] W. C. Chueh and S. M. Haile, “A thermochemical study of ceria: Exploiting an old material for new modes of energy conversion and CO2 mitigation,” *Philos. Trans. R. Soc. A Math. Phys. Eng. Sci.*, vol. 368, no. 1923, pp. 3269–3294, 2010, doi: 10.1098/rsta.2010.0114.

[116] M. Welte, K. Warren, J. R. Scheffe, and A. Steinfeld, “Combined Ceria Reduction and Methane Reforming in a Solar-Driven Particle-Transport Reactor,” *Ind. Eng. Chem. Res.*, vol. 56, no. 37, pp. 10300–10308, 2017, doi: 10.1021/acs.iecr.7b02738.

[117] L. Zeng, Z. Cheng, J. A. Fan, L. S. Fan, and J. Gong, “Metal oxide redox chemistry for chemical looping processes,” *Nat. Rev. Chem.*, vol. 2, no. 11, pp. 349–364, Nov. 2018, doi: 10.1038/S41570-018-0046-2.

[118] C. L. Muhich *et al.*, “Efficient generation of H2 by splitting water with an isothermal redox cycle,” *Science (80-.).*, vol. 341, no. 6145, pp. 540–542, Aug. 2013, doi: 10.1126/SCIENCE.1239454/SUPPL_FILE/MUHICH.SM.PDF.

[119] M. M. Nair and S. Abanades, “Solid-State Redox Kinetics of CeO2 in Two-Step Solar CH4 Partial Oxidation and Thermochemical CO2 Conversion,” *Catal. 2021, Vol. 11, Page 723*, vol. 11, no. 6, p. 723, Jun. 2021, doi: 10.3390/CATAL11060723.

[120] M. Portarapillo, A. Aronne, A. Di Benedetto, C. Imparato, G. Landi, and G. Luciani, “Syngas production through H2O/CO2 thermochemical splitting,” *Chem. Eng. Trans.*, vol. 74, pp. 43–48, 2019, doi: 10.3303/CET1974008.

[121] L. F. De Diego *et al.*, “Performance of Cu- and Fe-based oxygen carriers in a 500 Wth CLC unit for sour gas combustion with high H2S content,” *Int. J. Greenh. Gas Control*, vol. 28, pp. 168–179, Sep. 2014, doi: 10.1016/J.IJGGC.2014.06.026.

[122] V. V. Galvita, H. Poelman, V. Bliznuk, C. Detavernier, and G. B. Marin, “CeO2-Modified Fe2O3 for CO2 Utilization via Chemical Looping,” *Ind. Eng. Chem. Res.*, vol. 52, no. 25, pp. 8416–8426, Jun. 2013, doi: 10.1021/IE4003574.

[123] M. RydÃ©n, E. Cleverstam, M. Johansson, A. Lyngfelt, and T. Mattisson, “ Fe 2 O 3 on Ce-, Ca-, or Mg-stabilized ZrO 2 as oxygen carrier for chemical-looping combustion using NiO as additive ,” *AIChE J.*, p. NA-NA, 2010, doi: 10.1002/AIC.12143.

[124] J. Hu, H. Poelman, G. B. Marin, C. Detavernier, S. Kawi, and V. V. Galvita, “FeO controls the sintering of iron-based oxygen carriers in chemical looping

CO2conversion," *J. CO2 Util.*, vol. 40, Sep. 2020, doi: 10.1016/J.JCOU.2020.101216.

[125] F. He, H. Wang, and Y. Dai, "Application of Fe2O3/Al2O3 Composite Particles as Oxygen Carrier of Chemical Looping Combustion," *J. Nat. Gas Chem.*, vol. 16, no. 2, pp. 155–161, Jun. 2007, doi: 10.1016/S1003-9953(07)60041-3.

[126] W. Qin *et al.*, "Theoretical study of oxidation-reduction reaction of Fe 2 O 3 supported on MgO during chemical looping combustion," *Appl. Surf. Sci.*, vol. 266, pp. 350–354, Feb. 2013, doi: 10.1016/J.APSUSC.2012.12.023.

[127] Y. C. Liu, Y. Ku, Y. H. Tseng, H. Y. Lee, and Y. L. Kuo, "Fabrication of Fe2O3/TiO2 oxygen carriers for chemical looping combustion and hydrogen generation," *Aerosol Air Qual. Res.*, vol. 16, no. 8, pp. 2023–2032, Aug. 2016, doi: 10.4209/AAQR.2015.10.0603.

[128] Q. Zafar, T. Mattisson, and B. Gevert, "Integrated Hydrogen and Power Production with CO2 Capture Using Chemical-Looping ReformingRedox Reactivity of Particles of CuO, Mn2O3, NiO, and Fe2O3 Using SiO2 as a Support," *Ind. Eng. Chem. Res.*, vol. 44, no. 10, pp. 3485–3496, May 2005, doi: 10.1021/IE048978I.

[129] N. V. R. A. Dharanipragada, L. C. Buelens, H. Poelman, E. De Grave, V. V. Galvita, and G. B. Marin, "Mg–Fe–Al–O for advanced CO2 to CO conversion: carbon monoxide yield vs. oxygen storage capacity," *J. Mater. Chem. A*, vol. 3, no. 31, pp. 16251–16262, Jul. 2015, doi: 10.1039/C5TA02289D.

[130] Y. De Vos, M. Jacobs, I. Van Driessche, P. Van Der Voort, F. Snijkers, and A. Verberckmoes, "Processing and characterization of Fe-based oxygen carriers for chemical looping for hydrogen production," *Int. J. Greenh. Gas Control*, vol. 70, pp. 12–21, Mar. 2018, doi: 10.1016/J.IJGGC.2018.01.007.

[131] M. Ismail, W. Liu, and S. A. Scott, "The performance of Fe2O3-CaO Oxygen Carriers and the Interaction of Iron Oxides with CaO during Chemical Looping Combustion and H2 production," *Energy Procedia*, vol. C, no. 63, pp. 87–97, 2014, doi: 10.1016/J.EGYPRO.2014.11.010.

[132] W. Liu, J. S. Dennis, and S. A. Scott, “The effect of addition of ZrO2 to Fe2O3 for hydrogen production by chemical looping,” *Ind. Eng. Chem. Res.*, vol. 51, no. 51, pp. 16597–16609, Dec. 2012, doi: 10.1021/IE302626X/SUPPL_FILE/IE302626X_SI_001.PDF.

[133] X. Zhu, K. Li, Y. Wei, H. Wang, and L. Sun, “Chemical-Looping Steam Methane Reforming over a CeO2–Fe2O3 Oxygen Carrier: Evolution of Its Structure and Reducibility,” *Energy and Fuels*, vol. 28, no. 2, pp. 754–760, Feb. 2014, doi: 10.1021/EF402203A.

[134] M. Machida, T. Kawada, H. Fujii, and S. Hinokuma, “The Role of CeO2 as a Gateway for Oxygen Storage over CeO2-Grafted Fe2O3 Composite Materials,” *J. Phys. Chem. C*, vol. 119, no. 44, pp. 24932–24941, Nov. 2015, doi: 10.1021/ACS.JPCC.5B09876.

[135] S. Sun, M. Zhao, L. Cai, S. Zhang, D. Zeng, and R. Xiao, “Performance of CeO2-Modified Iron-Based Oxygen Carrier in the Chemical Looping Hydrogen Generation Process,” *Energy and Fuels*, vol. 29, no. 11, pp. 7612–7621, Nov. 2015, doi: 10.1021/ACS.ENERGYFUELS.5B01444.

[136] S. Bhavsar, M. Najera, and G. Veser, “Chemical Looping Dry Reforming as Novel, Intensified Process for CO2 Activation,” *Chem. Eng. Technol.*, vol. 35, no. 7, pp. 1281–1290, Jul. 2012, doi: 10.1002/CEAT.201100649.

[137] V. V. Galvita, H. Poelman, E. Fornero, M. Saeys, and G. B. Marin, “Development and Performance of Iron Based Oxygen Carriers for Chemical Looping,” *Nanotechnol. Catal.*, pp. 421–448, Jun. 2017, doi: 10.1002/9783527699827.CH18.

[138] E. Ksepko, “Perovskite Sr(Fe1-xCux)O3-Δ materials for chemical looping combustion applications,” *Int. J. Hydrogen Energy*, vol. 43, no. 20, pp. 9622–9634, May 2018, doi: 10.1016/J.IJHYDENE.2018.04.046.

[139] A. Bayon, A. de la Calle, K. K. Ghose, A. Page, and R. McNaughton, “Experimental, computational and thermodynamic studies in perovskites metal oxides for thermochemical fuel production: A review,” *Int. J. Hydrogen Energy*, vol. 45, no. 23, pp. 12653–12679, 2020, doi: 10.1016/j.ijhydene.2020.02.126.

[140] X. P. Dai, R. J. Li, C. C. Yu, and Z. P. Hao, “Unsteady-State Direct Partial Oxidation of Methane to Synthesis Gas in a Fixed-Bed Reactor Using AFeO3 (A = La, Nd, Eu) Perovskite-Type Oxides as Oxygen Storage,” *J. Phys. Chem. B*, vol. 110, no. 45, pp. 22525–22531, Nov. 2006, doi: 10.1021/JP063490B.

[141] O. Mihai, D. Chen, and A. Holmen, “Catalytic consequence of oxygen of lanthanum ferrite perovskite in chemical looping reforming of methane,” *Ind. Eng. Chem. Res.*, vol. 50, no. 5, pp. 2613–2621, Mar. 2011, doi: 10.1021/IE100651D.

[142] L. Nalbandian, A. Evdou, and V. Zaspalis, “La1−xSrxMyFe1−yO3−δ perovskites as oxygen-carrier materials for chemical-looping reforming,” *Int. J. Hydrogen Energy*, vol. 36, no. 11, pp. 6657–6670, Jun. 2011, doi: 10.1016/J.IJHYDENE.2011.02.146.

[143] F. He, X. Li, K. Zhao, Z. Huang, G. Wei, and H. Li, “The use of La1-xSrxFeO3 perovskite-type oxides as oxygen carriers in chemical-looping reforming of methane,” *Fuel*, vol. 108, pp. 465–473, 2013, doi: 10.1016/J.FUEL.2012.11.035.

[144] A. Haeussler, S. Abanades, A. Julbe, J. Jouannaux, and B. Cartoixa, “Two-step CO2 and H2O splitting using perovskite-coated ceria foam for enhanced green fuel production in a porous volumetric solar reactor,” *J. CO2 Util.*, vol. 41, p. 101257, Oct. 2020, doi: 10.1016/J.JCOU.2020.101257.

[145] J. R. Scheffe, D. Weibel, and A. Steinfeld, “Lanthanum–Strontium–Manganese Perovskites as Redox Materials for Solar Thermochemical Splitting of H2O and CO2,” *Energy and Fuels*, vol. 27, no. 8, pp. 4250–4257, Aug. 2013, doi: 10.1021/EF301923H.

[146] A. H. McDaniel *et al.*, “Sr- and Mn-doped LaAlO3−δ for solar thermochemical H2 and CO production,” *Energy Environ. Sci.*, vol. 6, no. 8, pp. 2424–2428, Jul. 2013, doi: 10.1039/C3EE41372A.

[147] T. Cooper, J. R. Scheffe, M. E. Galvez, R. Jacot, G. Patzke, and A. Steinfeld, “Lanthanum Manganite Perovskites with Ca/Sr A-site and Al B-site Doping as Effective Oxygen Exchange Materials for Solar Thermochemical Fuel Production,” *Energy Technol.*, vol. 3, no. 11, pp. 1130–1142, Nov. 2015, doi: 10.1002/ENTE.201500226.

[148] Q. Jiang, H. Zhang, Y. Cao, H. Hong, and H. Jin, “Solar hydrogen production via perovskite-based chemical-looping steam methane reforming,” *Energy Convers. Manag.*, vol. 187, pp. 523–536, May 2019, doi: 10.1016/J.ENCONMAN.2019.01.112.

[149] R. D. Barcellos, M. D. Sanders, J. Tong, A. H. McDaniel, and R. P. O’Hayre, “BaCe0.25Mn0.75O3−δ—a promising perovskite-type oxide for solar thermochemical hydrogen production,” *Energy Environ. Sci.*, vol. 11, no. 11, pp. 3256–3265, Nov. 2018, doi: 10.1039/C8EE01989D.

[150] S. Dey, B. S. Naidu, and C. N. R. Rao, “Ln0.5A0.5MnO3 (Ln=Lanthanide, A= Ca, Sr) Perovskites Exhibiting Remarkable Performance in the Thermochemical Generation of CO and H2 from CO2 and H2O,” *Chem. – A Eur. J.*, vol. 21, no. 19, pp. 7077–7081, May 2015, doi: 10.1002/CHEM.201500442.

[151] M. H. Imanieh, M. H. Rad, A. Nadarajah, J. González-Platas, F. Rivera-López, and I. R. Martín, “Novel perovskite ceramics for chemical looping combustion application,” *J. CO2 Util.*, vol. C, no. 13, pp. 95–104, Mar. 2016, doi: 10.1016/J.JCOU.2016.01.001.

[152] M. Boaro and A. Felli, “PRIN17 Project Direct Biopower,” 2020.

[153] Q. Liu, X. Dong, G. Xiao, F. Zhao, and F. Chen, “A Novel Electrode Material for Symmetrical SOFCs,” *Adv. Mater.*, vol. 22, no. 48, pp. 5478–5482, Dec. 2010, doi: 10.1002/ADMA.201001044.

[154] Y. Song, Q. Zhong, W. Tan, and C. Pan, “Effect of cobalt-substitution Sr2Fe1.5-xCo xMo0.5O6-δ for intermediate temperature symmetrical solid oxide fuel cells fed with H2-H2S,” *Electrochim. Acta*, vol. 139, pp. 13–20, Sep. 2014, doi: 10.1016/J.ELECTACTA.2014.07.022.

[155] Z. Du *et al.*, “High-Performance Anode Material Sr2FeMo0.65Ni0.35O6 - δ with in Situ Exsolved Nanoparticle Catalyst,” *ACS Nano*, vol. 10, no. 9, pp. 8660–8669, Sep. 2016, doi: 10.1021/ACSNANO.6B03979/SUPPL_FILE/NN6B03979_SI_001.PDF.

[156] A. V. Nikonov, K. A. Kuterbekov, K. Z. Bekmyrza, and N. B. Pavzderin, “A brief

review of conductivity and thermal expansion of perovskite-related oxides for SOFC cathode," *Eurasian J. Phys. Funct. Mater.*, vol. 2, no. 3, pp. 274–292, 2018, doi: 10.29317/EJPFM.2018020309.

[157] S. Hu *et al.*, "Detrimental phase evolution triggered by Ni in perovskite-type cathodes for CO2 electroreduction," *J. Energy Chem.*, vol. 36, pp. 87–94, Sep. 2019, doi: 10.1016/J.JECHEM.2019.06.001.

[158] Carbolite GeroLtd, "Carbolite Gero 3000°C, furnace brochure catalogue."

[159] Invensys Eurotherm, "iTools Help Manual," 2010.

[160] API SRL, "Manuale API- MIoT Poli_To," 2020.

[161] X. Liu, S. Cheng, H. Liu, S. Hu, D. Zhang, and H. Ning, "A Survey on Gas Sensing Technology," *Sensors (Basel).*, vol. 12, no. 7, p. 9635, Jul. 2012, doi: 10.3390/S120709635.

[162] S. B. Twiss, D. M. Teague, J. W. Bozek, and M. V Sink, "Sink (1955) Application of Infrared Spectroscopy to Exhaust Gas Analysis," *J. Air Pollut. Control Assoc.*, vol. 5, no. 2, pp. 75–83, 2012, doi: 10.1080/00966665.1955.10467692.

[163] "Chemical Library," [Online]. Available: https://chem.libretexts.org.

[164] P. L. Spath and D. C. Dayton, "Preliminary Screening -- Technical and Economic Assessment of Synthesis Gas to Fuels and Chemicals with Emphasis on the Potential for Biomass-Derived Syngas," *Natl. Renew. Energy Lab.*, no. December, pp. 1–160, 2003, doi: 10.2172/15006100.